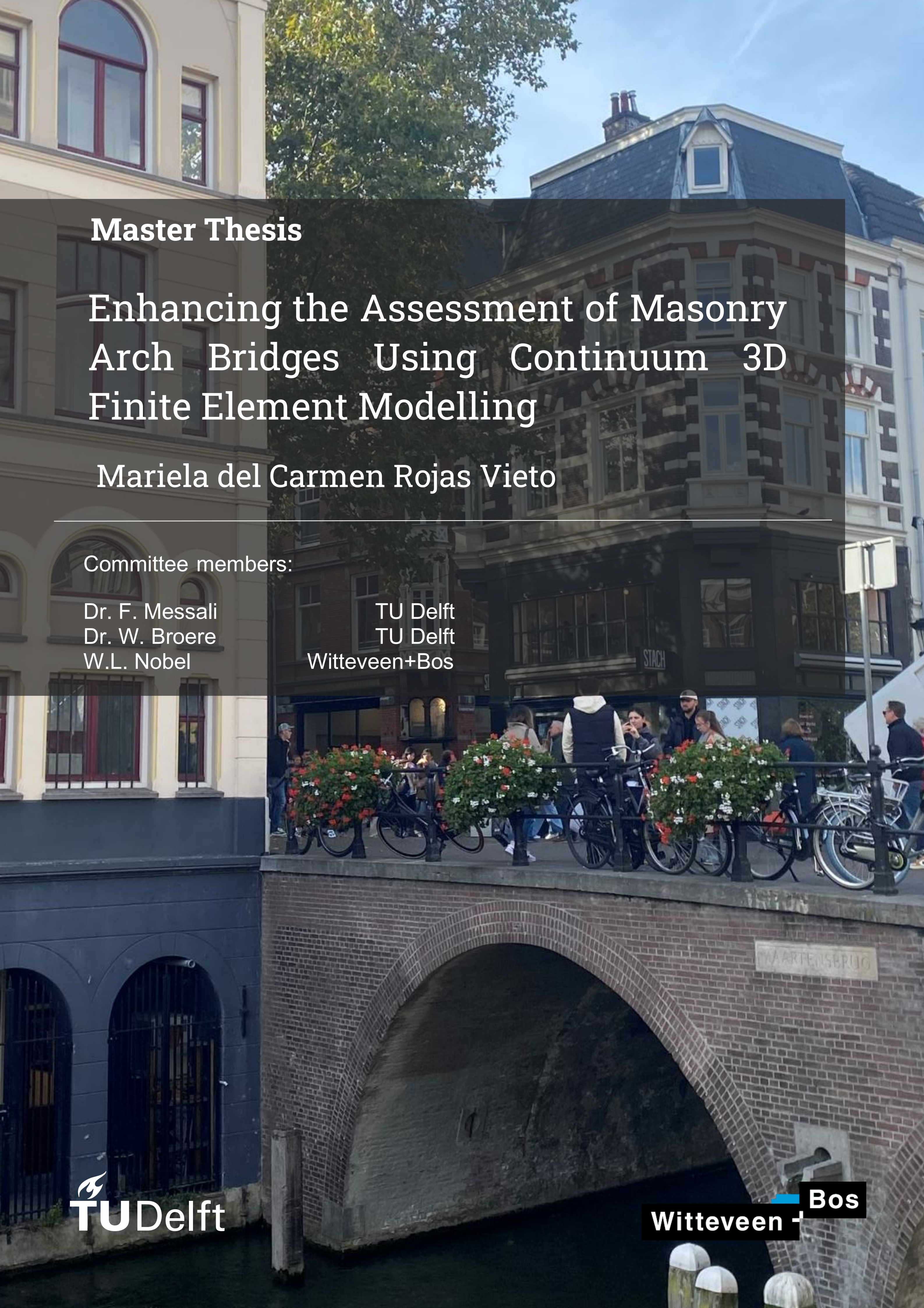

Master Thesis

Enhancing the Assessment of Masonry Arch Bridges Using Continuum 3D Finite Element Modelling

Mariela del Carmen Rojas Vieto

Committee members:

Dr. F. Messali	TU Delft
Dr. W. Broere	TU Delft
W.L. Nobel	Witteveen+Bos

Contents

Figure Index

Table Index

Summary

This thesis focuses on enhancing the assessment of masonry arch bridges through the application of advanced three-dimensional (3D) continuum finite element modelling (FEM). Many historical bridges in the Netherlands were designed for lighter loads than those imposed by current traffic conditions. Consequently, their structural evaluation is crucial to ensure safety, optimize maintenance strategies, and preserve cultural heritage. Existing design standards codes provide limited guidance for masonry bridge assessment, which emphasizes the need for refined numerical modelling techniques capable of capturing the real mechanical behavior of these complex structures.

To address this gap, a series of three- and two-dimensional finite element models were developed in DIANA FEA, based on a full-scale experimental benchmark bridge tested in the United Kingdom. The modelling approach incorporated both linear and nonlinear material behaviors for masonry and backfill using the total strain crack and Mohr-Coulomb constitutive models, respectively. Interface elements were used to represent the contact and frictional interactions between materials, while soil-structure interaction effects were explicitly modelled. The study systematically examined the influence of spandrel walls and backfill confinement on the bridge's global stiffness, load distribution, and ultimate capacity.

Model calibration was carried out using the mechanical properties and geometrical parameters provided by the benchmark test. The 3D nonlinear continuum model was validated against experimental results in terms of radial displacements, cracking, and collapse mechanisms. Comparative analyses between the 3D and 2D models demonstrate that the inclusion of spandrel walls in the 3D framework increases initial global stiffness by 30-36 % and peak-load capacity is increased by 50%. The 3D model accurately reproduced the load spreading through the backfill, the development of cracks, and the redistribution of stresses after cracking, but the 2D plane strain model was unable to capture effectively, which underestimated the capacity by 55%.

Overall, the findings confirm that nonlinear 3D continuum finite element modelling provides a more realistic representation of the structural response of masonry arch bridges. This modelling strategy not only improves predictive accuracy but also offers valuable insights for structural assessments. The outcomes of this research contribute to developing reliable evaluation methodologies and serve as a reference framework for future studies and engineering practice in the assessment of masonry arch structures.

Chapter 1 Introduction

1.1 Research context

The Netherlands has long been shaped by its extensive network of canals, originally developed not only for transportation and irrigation, but also for water management, which is crucial given that much of the country lies below sea level. As a result, bridges have historically been essential for crossing canals and rivers, with some dating back hundreds of years. Even today, bridges continue to serve these purposes, and the total number of such structures is considerable. Many of these older bridges remain in use, despite having been designed for much lower loads than those imposed today. Replacing them would require traffic disruptions and substantial investment. Additionally, the older the structure, the greater its value to Dutch cultural heritage.

1.2 Research Problem

Structural assessment is vital for developing advanced analytical tools that can accurately predict behavior and ensure safety. These tools enable the extension of a structure’s service life through retrofitting, repair, or strengthening, making them particularly important for the preservation of historic urban centers. Masonry arch bridges, as prominent elements of the Netherlands’ architectural legacy, require careful evaluation to maintain both structural integrity and cultural significance.

Higher-level assessments, which go beyond basic hand calculations, often involve linear and nonlinear finite element (FE) modeling. While these methods offer greater accuracy, they demand more computational time and resources. However, advancements in computing have made it possible to manage more complex models with an increasing number of variables, making 3D modeling both feasible and valuable.

Detailed on-site data is necessary to support such modeling efforts. While this level of detail can enhance assessment accuracy, its effectiveness must be validated, particularly for Dutch masonry arch bridges. Their behavior results from complex interactions between masonry units, mortar, and the surrounding soil. For instance, 3D models are essential when analyzing spandrel walls, which significantly influence structural stiffness (mainly in the in-plane direction) of the bridge. Studying the influence that the spandrel walls help identify its contribution to the final capacity of the bridge. In contrast, 2D models can only represent a slice of the bridge due to their simplified transverse geometry and therefore cannot include all the variables (such as the spandrel walls) in one model which might lead to under- or overestimation of the structure’s overall stiffness and strength. To be able to adequately represent the 3D situation adjustments have to be made on the 2D model since the contribution of spandrel walls cannot be represented in this model.

1.3 Research objective

The objective of this research is to support the structural assessment of existing masonry arch bridges by developing and analyzing continuum 3D finite element models. The study aims to determine the representativeness of these 3D models. It studies the load spread action on the backfill, soil structure interaction, the representation of spandrel walls in masonry bridges and the interaction between materials. This will help identify the added value of this 3D model through detecting effects that cannot be captured in a 2D model and quantifying the differences between the models and the benchmark. The research evaluates alternative modeling strategies and identifies which elements of 3D modeling contribute most for an accurate assessment.

1.4 Research questions

Main question:

How much can performing a continuum 3D finite element analysis improve the accuracy in the assessment of masonry arch bridges compared to 2D models?

Sub-questions:

1. How to select material properties that should be used to make the model comparable to the benchmark?
2. How does the choice of effective width in a 2D plane strain model influence its performance relative to a 3D model without spandrel walls?
3. What are the differences in stiffness, peak load capacity, cracking patterns and ductility between the 3D model and the benchmark experiment?
4. What are effects on stiffness, peak load capacity, cracking patterns and ductility due to the spandrel walls?

Chapter 2 Literature review

This chapter presents an overview of the existing knowledge relevant to masonry arch bridge assessment. It first explores the historical development and typology of masonry bridges, with emphasis on their materials, structural behavior, and the factors influencing their performance. The chapter reviews the behavior of backfill materials and their interaction with masonry components, followed by a discussion of the principal modelling techniques used to represent masonry structures. The chapter also summarizes the main assessment frameworks and experimental investigations available in literature.

2.1 Historic masonry bridges

Masonry structures have been constructed for centuries, starting with Egyptians and followed by the Greeks, and later the Romans. These civilizations constructed many structures that are still standing, such as the aqueducts and churches. They often used stone rather than bricks. Later, with the industrial revolution, Portland cement was widely used even in masonry structures, improving durability and strength. And now, however, due to technological innovation, masonry is no longer used in the construction of new bridges. (Pipinato, 2016)

In the Netherlands, bridges date back to at least 1275 with the Saint Servatius bridge in Maastricht being one of the earliest examples. Since then, the number of bridges has been increasing ever since. During this period, medieval bridges were typically made using stones and lime mortar. Although this mortar tended to degrade over time, stones are accommodated in a way that it would remain stable with mortar or without mortar. As a result, many of these structures still stand, although modern vibrations from traffic can cause bricks or stones to fall from the arches. (Orduna, 2003)

As bridges age, several forms of deterioration can occur. These include corrosion of brick surfaces due to weathering, surface wear, falling bricks, and cracks caused by freeze-thaw cycles or incompatible cladding materials. Some bridges built in the late 1800s, such as those in Latvia studied by Paeglītis et al. (2013), used porous clay bricks and dolomite stones bonded with dolomite lime mortar. This combination, along with properly sized aggregates, allowed moisture to migrate naturally through the structure, making the materials highly compatible and the bridges durable.

Later assessments using 3D finite element modeling confirmed that such bridges were still capable of handling ordinary traffic loads. This suggests that many older bridges, especially those built with these material combinations, remain structurally safe today. In fact, some have proven to be more durable than those in the early 20th century, even those repaired with reinforced concrete. Still, each case must be individually evaluated to ensure safety and longevity.

While bridges primarily serve for transportation and connectivity, the abundance of them in the Netherlands is large due to the country's extensive canal system. These canals were originally developed for water management and defense, and later adapted for transport, drainage, and eventually tourism. Today, many of these historic bridges are part of the Netherlands' cultural heritage and maintaining them is crucial to preserving that legacy.

Masonry is composed of specifically shaped stones, bricks, or a combination of both, bonded together with mortar. The construction of masonry structures relies primarily on gravity, with compression being the dominant stress state. Due to the nature of their construction, these structures offer limited resistance in tension. As a result, the individual elements must be capable of withstanding significant compressive forces before crushing occurs.

While stone or brick can exhibit considerable strength in both compression and tension, the mortar between them is relatively weak. According to Heyman (1969), it is safe to assume that masonry can be considered to have infinite compressive strength and no tensile strength. Although sliding failure is theoretically possible, it is considered unlikely. Heyman disregarded this failure mode in his calculations, assuming that sliding failure does not occur. A usual assumption he made was that failure takes place under small displacements. While these assumptions simplify the analysis, it does not imply that crushing cannot happen, and in some cases, this assumption may lead to unsafe results. Therefore, it is essential to introduce realistic limits to material strength in modern analyses.

Masonry bridges are made up of various components, as illustrated in Figure 1. However, not all elements are present in single-span masonry bridges. For the purposes of this research, the focus will be on the key components: spandrel walls, stone or brick units, abutments, and fill material.

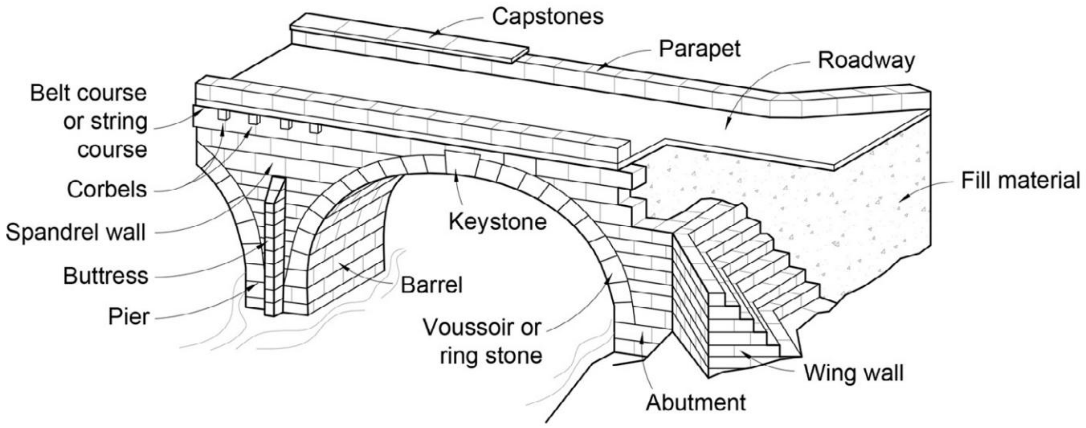

Figure 1. Elements of masonry arch bridges (Pipinato, 2016).

2.1.1 Available information of codes

For masonry bridges, the NPR998:2020 only specifies characteristics for clay bricks, calcium-silicate bricks and concrete bricks. It also provides information for the mortar depending on whether the masonry is unreinforced, confined or reinforced.

According to Eurocode 6, a guideline for designing with masonry is addressed, but bridges are not covered in the scope of this code. Even though this code doesn’t cover bridges, properties of materials such as clay bricks and stone can be useful for modelling or for design, when properties are unknown.

Due to the lack of codes for assessing or redesigning this type of masonry structure, the knowledge must be sought for in existing literature. Therefore, it’s essential to understand the materials, the composite action and the overall structural behavior of these bridges to correctly estimate the response using computational methods,

2.1.2 Arch structure

The arch is an essential element in masonry arch bridges; there are several ways this can be formed. This is element of the bridge is key to understanding the behavior of the collapse mechanism. The parts of the arch are shown in Figure 2.

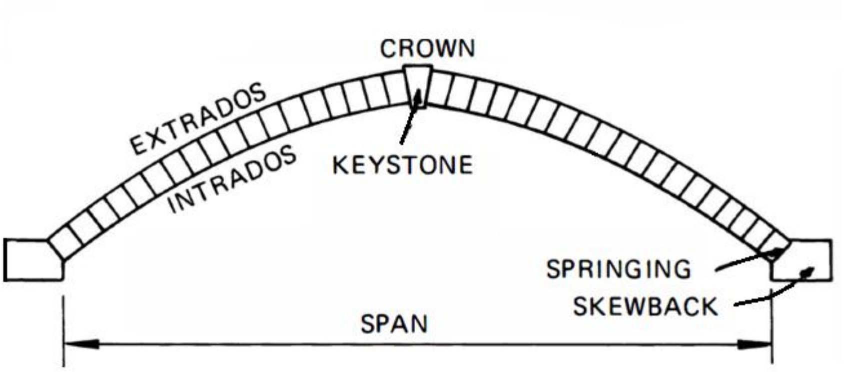

Figure 2. Parts of the arch (Heyman, 1982).

According to Heyman (1982), the thickness and the shape of the arch can make an arch safer or not because of the way that the loads travel. It also depends on the location of the load application, since the hinges will form where the travelling of the load as a straight line from the load to the supports meet the intrados of the arch creating an opening in the extrados. This explains the higher load capacity that these types of bridges have when loaded at the crown, and as the load moves away from the crown through the arch, then a lower capacity is found. The behavior can be seen in Figure 3, this load is creating a 4-hinge mechanism, or as Heyman calls it a "four-bar chain" mechanism. Depending on how the load is transferred to the supports, the location of the load and the shape of the arch, then the hinges might defer.

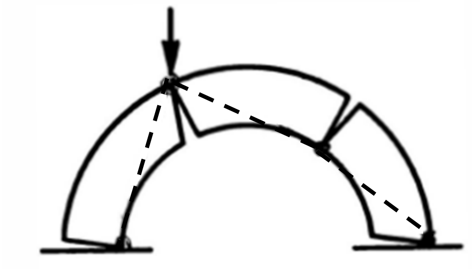

Figure 3. Failure mechanism (Heyman, 1982)

2.1.3 Masonry behavior

Masonry in bridges can be made of several materials, as mentioned previously. As the structure is made by two main materials, the bricks and the mortar, they each behave differently.

The masonry units vary in properties since they can be made from different materials. Variation between the bricks used to be higher than now because of the control conditions that they have. The units themselves have their own compressive and tensile behavior, although the results in test vary depending on the material and the conditions in which the element was tested. This element tends to have high compressibility and a lower tension.

On the other hand, the mortar also has its own properties. The mortar since it's a combination of materials, and the proportions and materials used are directly related to its performance. In the same way as the bricks, they have higher compressibility than tension.

Since masonry is composed of these two elements, composite action is often also analyzed. Specifically, the interface between the mortar and the bricks, this interface is the bond and often the weakest link particularly when the masonry is subject to tension. The behavior generally follows a brittle behavior as shown in Figure 4. This is unusually obtained using a tensile test which contributes to determining the mode I fracture energy (G^{I}_{f}). The value is, as described in Ghiassi, et al. (2019) "the amount of energy needed to create a unit area of a crack along the brick-mortar interface" which is the same as the area below the curve. As for mode II fracture energy (G^{II}_{f}) it's associated to shear, and it depends on the normal stresses. Shear most of the time can be described as a Mohr-Coulomb relationship. (Ghiassi, et al., 2019) Where σ is stress, u_n is the normal displacement and f_t is the maximum tensile stress.

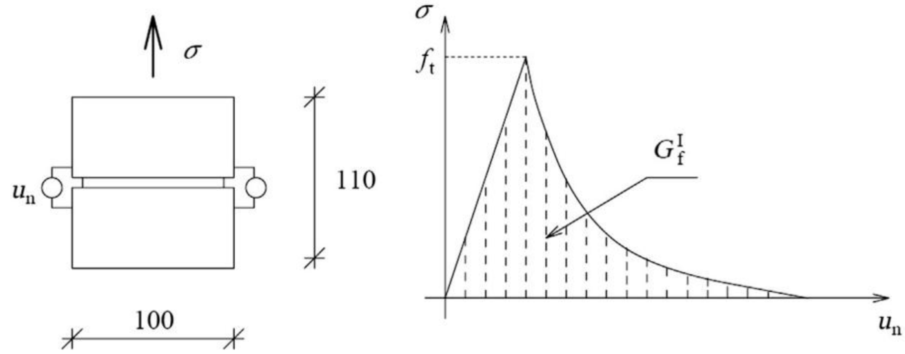

Figure 4. Tensile behavior of the brick mortar interface (Lourenco, 1994)

Masonry as a composite material also has a certain behavior, although much more variable than when analyzed separately. A parabolic curve is usually adopted since it's the typical behavior of the masonry, although it's always better to have a test and use a constitutive model that better adapts to the real behavior as shown in Figure 5. (Ghiassi, et al., 2019)

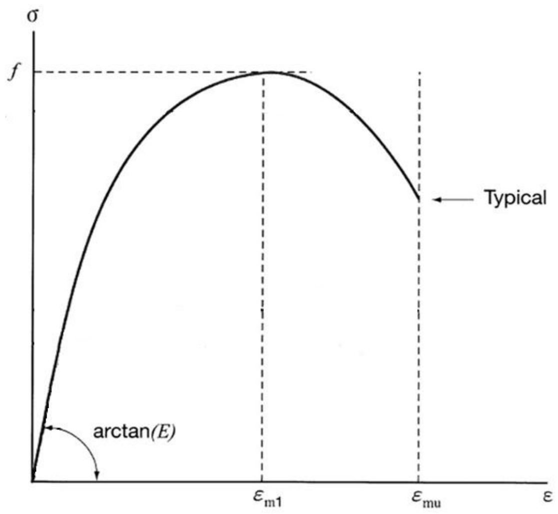

Figure 5. Compressive behavior of masonry as a composite (Ghiassi et al., 2019)

When testing the composite action of masonry in tension, three main failures can occur: cracking in the masonry units or in the mortar, separation of the interface between the mortar and the bricks, or a crack in the horizontal or vertical direction crossing the brick and the mortar. (Ghiassi, et al., 2019)

2.2 Backfill behavior as a soil material

The backfill in masonry arch bridges plays an important role in their structural behavior, as it positively influences the overall response of the bridge. For this reason, it is important to accurately represent backfill material in structural models to ensure that simulated behavior closely reflects real-world performance.

The physical behavior of soil is complex; however, when used as backfill in a masonry bridge, it can often be treated as relatively uniform, since its placement and compaction are controlled and, therefore, achieves more consistent properties. Soil behavior is commonly described using the Mohr-Coulomb failure criterion, where failure occurs once the shear strength envelope is exceeded. Another important aspect is consolidation, which is directly linked to settlements. During this process, water is drained from the soil's pores under sustained loading, leading to gradual volume reduction (a phenomenon characteristic of soils). Permeability governs the rate of drainage, and it influences the consolidation process.

The soil as a backfill material in the masonry bridge provides support and contributes to the load distribution. Tests suggest that the backfill has a positive effect on the load capacity of the bridge. Some of them suggest that the load spread allows the bridge to have a higher capacity, which is reasonable as the stresses due to the load at the arch are lower than the ones received by the soil. (Sarhosis et al., 2016)

According to Papa et al. (2021), one of the primary causes of cracking in bridges and other structures is differential settlement, though other factors can also contribute. When modeling, it is essential to properly consider the interaction between the soil and masonry by incorporating soil-structure interface elements.

2.2.1 Interfaces between materials

It’s important to understand that the interface between soil and other materials can have a behavior different from the material properties themselves. Depending on the type of soil and the material it rests, these properties will vary. The shape and surface texture of the material in contact with the soil are also key factors that need to be considered to determine surface friction. The smoother the material, the less friction there will be at the interface. This interaction influences the behavior of the entire bridge; the more friction there is at the interfaces, the higher the capacity of the bridge.

Including interfaces allow the model to behave closer to the real scenario. When interfaces are included, cracking and sliding can be developed in these locations. These allow redistribution of stresses, and therefore, when opening, sliding or crushing occurs, there is a relief of the concentrations of stress because it is redirected so the model finds a new equilibrium path. When including an interface, the properties tend to be weaker and more deformable than the adjacent materials. The properties of these elements should be properly estimated so that stability is not being wrongly estimated.

2.3 Modelling techniques

There are many modeling techniques to simulate the structural response of structures. These include finite element modelling (FEM), limit analysis, discrete element method and data driven models.

FEM is a widely used numerical technique for structural analysis. It works by dividing a structure into smaller, manageable components called finite elements, which are connected at points known as nodes. FEM can be performed using two main approaches: linear and non-linear analysis. Linear analysis is a simplified method where stress is directly proportional to strain, assuming elastic behavior of materials. This approach is often preferred when computational efficiency is needed or when material properties are not available.

Non-linear analysis, on the other hand, considers real-world behavior. These include material nonlinearity (e.g., yielding, cracking, crushing), geometric nonlinearity (changes in stiffness due to large deformations), and contact nonlinearity (such as slipping or separation at interfaces). Though this method demands greater computational resources, it gives results that more accurately reflect actual structural behavior.

One commonly used modeling technique for masonry arches is limit analysis, which has proven to be both efficient and reliable. This method is grounded in three core theorems (Ferreira, 2007):

- The lower bound theorem, which ensures safety by analyzing force equilibrium and stress distribution within yield limits.
- The upper bound theorem, which focuses on plastic mechanisms and equates internal and external work.
- The uniqueness theorem, which asserts that if both bounds converge, the solution is definitive.

Using limit analysis, the failure mechanism and load-carrying capacity of an arch can be determined relatively quickly. In many cases, models include hinges within the arch to estimate load capacity; however, the positions of these hinges are not known beforehand and must be determined as part of the analysis. Heyman (1969) expanded on this approach by incorporating thrust line analysis for arches without backfill.

The plastic method provides a safety factor by allowing the structure to form plastic hinges or joints between blocks or bricks as it approaches failure. This method enables the redistribution of internal forces, enhancing the structure's ability to carry loads beyond the elastic limit.

Another modeling method, discrete element modeling (DEM), involves rigid block discretization. The numerical technique uses individual elements connected by interfaces. It is made to study collapse, sliding and large displacements. It can also be hybrid by combining FEM with DEM. This hybrid technique is particularly useful for 2D models, where simplifications allow for more manageable computations (Milani & Lourenço, 2012).

As we move into the realm of artificial intelligence, parts of the modeling process can be complemented by data-driven models.

2.3.1 FEM modelling strategies

For FEM modelling, the strategies can be categorized into two main scales: microscale (or mesoscale) and macroscale (continuum) approaches. The microscale method, sometimes referred to as mesoscale in literature, models individual bricks, mortar, and their interfaces in detail (see Figure 6(b)). A simplified version of this approach involves modeling only the bricks and defining the interfaces between them, omitting the mortar entirely (see Figure 6 (c)). In contrast, the macroscale approach treats masonry as a homogeneous material, using larger elements that conform to the overall geometry of the structure (Figure 6(d)). This method significantly reduces modeling time and computational load.

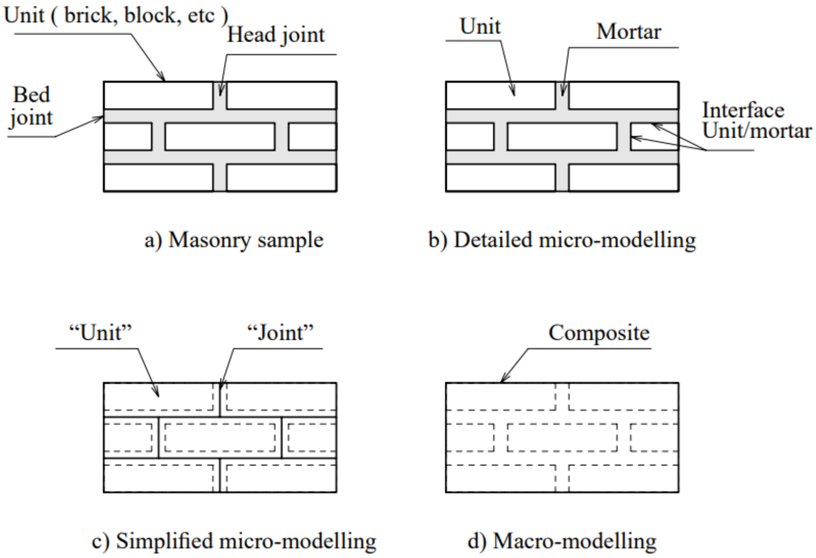

a) Masonry sample b) Detailed micro-modelling

c) Simplified micro-modelling d) Macro-modelling

Figure 6. Scale of masonry modelling (Lourenco, 1994)

At the structural level, the bridge can be discretized into parallelepiped rigid elements and quadrilateral elasto-plastic elements with softening interfaces, where all deformations are concentrated (Milani & Lourenço, 2012). These interfaces can be interconnected using elements that accommodate three nonlinear displacements and supports, allowing for a realistic simulation of complex interactions within the masonry system.

In modeling, the choice between a macro- or micro-modeling approach depends on the specific context and dimensions of the bridge. This decision is typically guided by a balance between computational cost, modeling time, and the desired level of accuracy. Macro modeling (also referenced in this document as continuum model) is typically faster and less computationally intensive, though it may come at the expense of some detail and precision compared to micro modeling. Both approaches, however, are commonly used in the structural assessment of masonry arch bridges.

A clear example of macro-scale modeling is presented by Milani and Lourenço (2012) in their study titled *"3D Non-linear Behavior of Masonry Arch Bridges."* In this work, a macro 3D model is developed, with the arch represented using a mesh of parallelepiped elements. Although the main objective was to analyze the bridge's 3D behavior, a 2D model was also created to study the interaction between the backfill and the arch. The research showed that while the 3D model provided more representative results, the 2D model still offered a simplified perspective of the same behavior, though with limitations in capturing the full complexity.

For 3D modeling, a macro-scale approach is commonly preferred due to the substantial computational resources required. In this example method, the spandrel wall was modeled as an orthotropic and homogeneous material, while the backfill was represented using a Mohr-Coulomb isotropic material model, incorporating tension cutoff and softening behavior (an approach demonstrated in the work of Milani & Lourenço (2012)).

2.3.2 Elements

The elements are determined based on the type of model required. They can be plane stress or plane strain when modeling a 2D model. As for 3D models, structural solid elements (as DIANA FEA has as an element class) are used.

Stresses are defined as a force distributed over an area. These are divided into two: normal stresses (σ) which act perpendicular to the surface and shear stresses (τ) which act parallel to the surface. Stress is described as:

$$\sigma = \frac{Force}{Area}$$

Strain is defined as a change in length relative to the original length of an element. These, as stresses, also have two types, normal strain (ϵ) which is perpendicular to the surface and shear strain (γ) which is parallel to the surface.

$$\varepsilon = \frac{\Delta length}{Length_{original}}$$

In solids, these can be related using a constitutive law which describes the material behavior. The conservation laws of mass and momentum help understand the mechanics of the solid. The mass conservation law assumes materials are continuous and is based on the principle that mass is neither created nor destroyed. And the momentum conservation law states that the momentum of the system remains constant unless an external force acts on it. This law provides the base to the equilibrium equations used for solving models.

When modeling a solid in 2D, the plane stress elements can be used. This condition is used when there are no forces or very small forces which are close to zero in one of the directions. This would mean that the stresses in this direction with zero force would be zero (normal and shear stresses). In DIANA FEA, when using a 2D model, the forces in z-direction are none (out-of-plane direction), meaning that.

$$\sigma_{zz} = 0$$

$$\sigma_{zy} = \sigma_{yz} = 0$$

$$\sigma_{zx} = \sigma_{xz} = 0$$

Whereas for plane strain would be an ideal approach when the element that is being analyzed has no strain in one of the directions because of an invariance of the loading and the structure in the same direction, in DIANA FEA software, the 2D model would assume the z-direction (out-of-plane direction), which translates to. (Van Dalen & Vardon, 2023).

$$\varepsilon_{zz} = 0$$

$$\varepsilon_{zy} = \varepsilon_{yz} = 0$$

$$\varepsilon_{zx} = \varepsilon_{xz} = 0$$

Because of Hooke's law, which relates stresses and strains, DIANA FEA software calculates values for each relationship. However, the results might not always be fully useful, depending on the specific conditions and assumptions made during the analysis.

The element geometries are several. These include nodes, lines and plane faces. The plane faces can be modelled in different geometries, triangular (figure a and figure b) or quadrilateral (figure c and figure d). When having a 3D model these geometries combine to obtain a pyramid (4 triangles connected to each other), wedge (2 triangles and 3 quadrilaterals interconnected) or brick (6 quadrilaterals connected to each other).

These can be divided into first (linear), second order (quadratic) or third order (cubic) and so on, and the interpolation can be linear, quadratic, cubic, etc, but the software DIANA FEA has an on-shape interpolation instead of a quadratic and cubic interpolation. Some of the geometries are shown in Figure 7 in which the first two figures on the left side (figures a and b) are linear and the two figures on the right side (figures c and d) are quadratic.

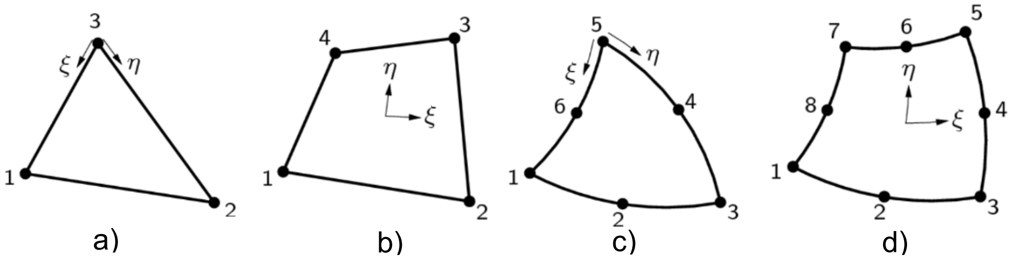

Figure 7. General geometry types (DIANA FEA, 2025)

The selection of the element geometry, with the different combinations mentioned above, is related to the type of element, the size of the mesh, and how detailed the analysis is intended to be.

For the connection between elements is continuous, unless specified differently. The type of connection can be defined in DIANA FEA, and therefore if an interface has a particular property, a connection can be made. The connection can be interfaces, springs, hinges, slides or even disconnection. Table 1 shows a summary of the elements per material.

Table 1. Elements for 2D and 3D models for the different materials

Material	2D	3D
Reinforced concrete	Plane stress elements Quadrilateral/Triangular Quadratic/Linear	3D solid elements Brick/Wedge/Pyramid Linear/Quadratic
Masonry	Plane stress elements Quadrilateral/Triangular Quadratic/Linear	3D solid elements Brick/Wedge/Pyramid Linear/Quadratic
Soil	Plane stress elements Quadrilateral/Triangular Quadratic/Linear	3D solid elements Brick/Wedge/Pyramid Linear/Quadratic
Soil structure interaction	2D interface elements	3D interface elements

2.3.3 Iterative procedures

Iterative procedures are used to progressively reach a solution through repeated approximation. One common method is the incremental-iterative procedure, in which the load is applied in increments. For each increment, the model balances external and internal forces until either the convergence criterion is met, or the maximum number of iterations is reached.

A commonly used technique within this framework is the full Newton-Raphson method (also referred to as Regular Newton-Raphson in DIANA FEA). In this approach, the stiffness matrix is updated at every iteration, which allows the method to converge in fewer steps, as shown in Figure 8 (a). However, its effectiveness depends heavily on the accuracy of the initial stiffness estimate. If the initial guess is far from the actual solution, the method may fail to converge.

To address this limitation, a modified Newton-Raphson method is often used. It is also an alternative in DIANA FEA. This variation updates the stiffness matrix only once per load increment and continues iterating using the same matrix until convergence is reached (see Figure 8 (b)). While this method may require more iterations to converge, it significantly reduces the computational cost of recalculating the stiffness matrix at every step.

Another variation is the Quasi-Newton method, referred to as the secant method in DIANA FEA. Like the regular Newton-Raphson method, it updates the stiffness matrix at each iteration. However, instead of recalculating it entirely, the Quasi-Newton method approximates stiffness using information from previous iterations (Figure 8(c)), making it a more efficient alternative in some scenarios (DIANA FEA, 2025).

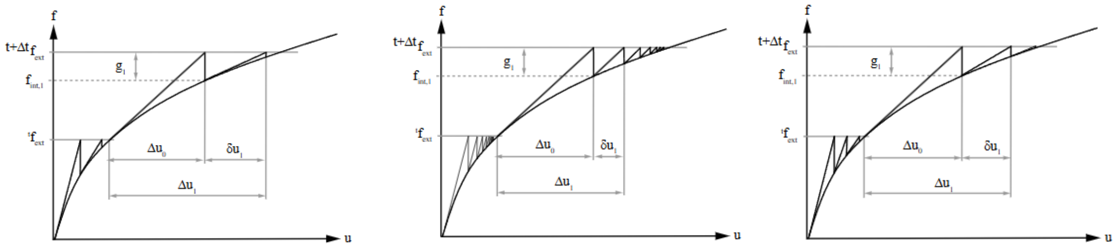

a) b) c)

Figure 8. Newton-Raphson Iteration methods (DIANA FEA, 2025)

Another approach is the linear stiffness method, which uses the stiffness matrix calculated during the first load increment and retains it for all subsequent increments. This method maintains the matrix as symmetrical and does not update stiffness throughout the analysis. As a result, while each iteration is computationally faster than in methods that update stiffness at every step, convergence tends to be slower, often requiring a larger number of iterations per increment (DIANA FEA, 2025). This method is illustrated in Figure 9.

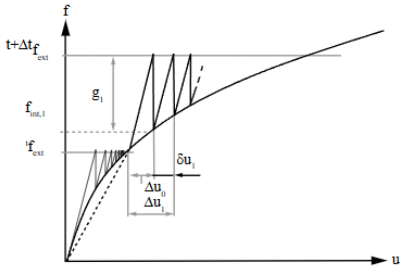

Figure 9. Linear stiffness method (DIANA, 2025)

Another alternative available in DIANA FEA is the constant stiffness method. In this approach, the stiffness matrix from the previous load increment is reused in the current increment. After the first interpolation step, it functions similarly to the linear stiffness method. While this method is one of several possible alternatives, DIANA FEA does not implement all the existing methods within the software (DIANA FEA, 2025).

Once an iterative solution method is selected, it is equally important to define appropriate convergence criteria. The most fundamental criterion is to stop the iteration once convergence has been achieved. Additional stopping conditions include reaching a maximum number of iterations or detecting divergence in the solution.

Several types of convergence norms can be used to evaluate whether convergence has been reached:

- Force norm: This compares the externally applied forces to the internal forces calculated during the iteration. The difference between them must fall below a predefined tolerance.
- Displacement norm: This compares the displacement from the current iteration to the displacement from the initial guess. The iteration is considered converged when this difference is within the assigned tolerance.
- Energy norm: This norm evaluates the convergence by balancing internal energy, considering both the internal forces and displacements. It ensures that the energy residuals are within acceptable limits.

Each norm offers different ways to solve the model, and the choice of norm often depends on the nature of the problem and the desired level of accuracy (DIANA FEA, 2025).

2.3.4 Load application

Loads can be applied in various ways, depending on the type of target (such as a vertex, edge, surface, or face). They may take the form of forces, moments, prescribed deformations, or other load types, depending on the requirements of the analysis. These loads can be applied either as point loads or distributed loads across the selected target. The appropriate method depends on the objective and nature of the simulation.

Structural tests and numerical models often use either load control or displacement control methods. In linear analysis, where the response is proportional to the applied load, the choice between these two is less critical. Since the system stiffness is constant and known, either the displacement or the force can be calculated from the other with equal validity.

In practice, force control is typically used when the applied load is known in advance and the structure is expected to remain in the elastic range, that is, when no sudden failure or instability is anticipated. The corresponding displacement is then calculated as a response to the applied force.

For nonlinear models, displacement control is often preferred. This is because the structural behavior may be unpredictable, and a known displacement provides a more stable input. In these cases, the model applies to a predefined displacement, and the resulting force is computed. This method is particularly useful when the failure load is unknown or when sudden collapse needs to be avoided during simulation.

2.3.5 Load spread

The backfill material used in masonry bridges should be considered not only as an external load but also as a structural component that contributes to the overall behavior of the bridge. It is typically modeled as a homogeneous and isotropic material. There are several ways to represent backfill in numerical models. One common approach is to apply it as an equivalent load on the masonry structure. Another method involves modeling the backfill as a solid volume with interface elements placed between it and the masonry blocks to simulate their interaction. Alternatively, the backfill can be represented as a system of rigid blocks, which helps simulate internal energy dissipation and sliding behavior, similar to natural failure planes within the soil (Papa et al., 2021).

In DIANA FEA, load distribution through the backfill is considered, but for 2D models, adjustments are needed to account for the model's assumptions and limitations. These adjustments ensure that the output remains realistic. Accurately understanding how the load spreads through the backfill helps in calculating an equivalent load that closely reflects real-world conditions. The load is typically assumed to be distributed over a wider area, calculated based on the width of the footing (B). The redistributed width (B') is given by the equation:

$$B' = B + 2 * D * \tan\beta$$

Where:

- D is the height of the layer of soil
- β is the spread angle
- B is the width of the footing

Because soil primarily transmits compressive forces and not tension, the contact behavior between the backfill and the masonry must be carefully defined. Interface elements are used to capture this interaction. These interfaces can be modeled with nonlinear properties (allowing compression, zero tension, and some shear capacity due to friction). This ensures that soil does not introduce unintended tensile forces onto the arch, spandrel walls (in 3D models), or reinforced walls (in both 2D and 3D models). Accurately defining these interface behaviors leads to a model that better reflects the actual structural response of masonry arch bridges under backfill pressure.

In reality the load spread has a bell shape distribution of the load over a surface, in every direction in which the load spread is looked at, producing a circular bell shape distribution of the load instead of a squared shaped as the approximation above suggests. Boussinesq, in 1885, studied the stress distribution of a point load through an elastic and isotropic material. He developed a more realistic approach for calculating how the load spreads through the material.

2.3.6 Materials constitutive models

Depending on the context, constitutive models can vary to represent different material behaviors. The linear elastic model is commonly used when analyzing the elastic range of material. At the initial stage, most constitutive models are assumed to behave in a linear elastic manner, meaning stress is directly proportional to strain. This relationship is defined by Hooke’s law and reflects a material’s elasticity, or its ability to return to its original shape once the applied force is removed. In this model, stiffness (represented by the slope of the stress-strain curve, Eo) remains constant during both loading and unloading. As shown in Figure 10, the material follows the same linear path up to the yielding point.

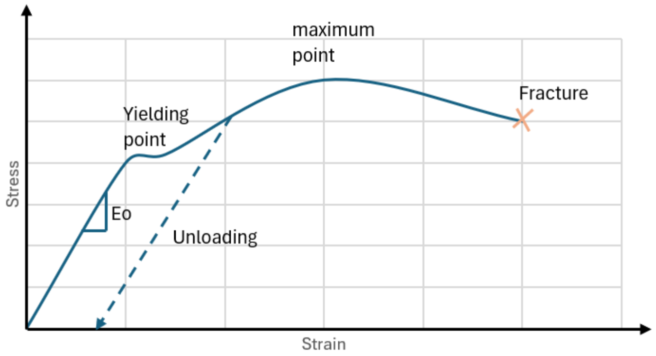

Figure 10. Steel ideal stress-strain curve

Linear elastic models can be either isotropic or orthotropic. In isotropic materials, properties are the same in all directions, making their behavior uniform regardless of orientation. Orthotropic materials, while still behaving linearly and elastically, have stiffness properties that vary depending on the direction, which is common in composite or layered materials.

Figure 10 shows a typical response of plastic material, but this doesn’t apply to all. When a material goes beyond the elastic range and reaches the yielding point, it enters the plastic region. In this phase, the stress-strain curve becomes nonlinear (as illustrated in Figure 10), and the material gets permanent deformation. When unloading, the material typically follows a linear path with the same initial stiffness, but it does not return to its original shape. Plastic behavior can appear as ductility or hardening. Ductility describes the ability of a material to deform plastically before failure, often with little increase in stress. Hardening, on the other hand, occurs when the material requires more stress to continue deforming after yielding, indicating an increase in resistance.

Cracking in materials can be modeled in two ways: smeared or discrete. Smeared cracking is used when cracks are distributed over an area, typically in regions experiencing high tensile stress without a clearly defined cracking path. Discrete cracking is used to simulate localized fractures at specific points where crack initiation and propagation are expected. In both cases, understanding the nature of cracking is essential for accurate structural analysis.

To simulate the interaction between different materials or components, interface elements are introduced. These elements define the behavior at contact surfaces or edges by assigning normal and shear stiffness values. They can model a variety of physical responses, including sliding, separation, or bonding, depending on the mechanical conditions at the interface.

2.3.6.1 Reinforced concrete modelling

When looking for options to model reinforced concrete, typically, it is modeled as two distinct materials when the location and properties of the reinforcement are known. Each material is represented according to its nonlinear behavior, and the software accounts for their composite action. Steel usually follows a stress-strain curve like the one shown in Figure 10, characterized by a clear yield point and strain hardening, while concrete follows a smoother, more gradual curve with a brittle behavior.

When concrete and steel are modeled separately, DIANA offers various material models for concrete based on different design codes, including European, American, and Japanese standards. In these cases, the required input values depend on the concrete classification and include key properties like Young’s modulus and characteristic stresses for both materials. If the relevant code isn’t available in the software, there are alternatives, such as the "crack and plasticity" model in DIANA, which allow users to define custom cracking and plasticity behavior as needed.

In situations where detailed information about the reinforcement is missing, reinforced concrete may need to be modeled as a single, composite material. In that case, the constitutive model must be adjusted to represent an equivalent material that captures both crushing behavior and a degree of ductility.

Depending on the analysis objectives, a simple linear elastic model may be sufficient. This can involve using separate Young’s modulus values for concrete and steel or a single equivalent modulus for the composite material. If a more advanced analysis is required but the composite material approach must still be used, the "crack and plasticity" model can also be applied. However, it’s important that the material properties used reflect the combined behavior of both concrete and reinforcement.

2.3.6.2 Masonry modelling

Masonry is a composite material made up of two main components: bricks or stones and mortar. It primarily resists load through compression and is considered anisotropic, meaning its properties vary depending on the direction. Because masonry is composed of different materials, modeling it as a homogeneous material can be challenging.

Masonry has been tested in compression and in tension, and the results are not always representative when testing composite behavior. In compression it has been found that compression test made (with 5 bricks: one on top of the other one) tend to overestimate the Young's modulus when comparing them to large walls. In tension, the composite behavior has an exponential softening curve, and mode I fracture energy has a typical range between 0,005 and 0,02 N/mm. For shear, results on testing say that it has an exponential softening curve with a Mode II (fracture energy) between 0,01 and 0,25 N/mm. (Lourenco, 1994)

Although experimental results tend to have some inaccuracies, there is a trend. Based on experimental tests, the typical behavior of masonry matches the curves shown in section 2.1.3, the ratio σ_t / σ_c ranges between 0,1 and 0,01. From the behavior of masonry, the curves that best represent the behavior of the compressive composite action is a parabolic curve. Whereas tension, an exponential curve fits accordingly.

Several options can be considered when making a continuum model, some models represent the material without considering the composite behavior of the masonry.

When creating a micro-model, each material component should be modeled separately, and interface elements are necessary. Interface elements can be used instead of explicitly modeling mortar between bricks, or they can represent the interfaces between mortar and bricks if the mortar is modeled.

In contrast, for macro-modeling or continuum modeling, where masonry is modeled as a combined material (bricks and mortar), masonry is best represented using a total strain-based cracking model when the structure is not a wall. This approach is ideal when performing a continuum model because the initial locations of cracking are typically unknown during analysis, and the model effectively captures both tensile and compressive behaviors by providing a variety of curve options for each. Since composite materials like masonry exhibit distinct properties under tension and compression, the total strain-based cracking model is well suited to represent their complex behavior.

This model is based on the Modified Compression Field Theory (MCFT), which was initially developed to represent smeared cracking in reinforced concrete modeled as an orthotropic material. Similarly, the total strain-based cracking model uses a smeared approach to represent fracture energy. However, unlike the original MCFT, this model has been adapted for use in three dimensions.

In this model, strain is used to define the stress response. Due to the way it has been implemented in DIANA FEA software, the model offers several options for representing compressive and tensile behavior. There are two main approaches for defining crack orientation. The first is the rotating crack model, in which cracks form perpendicular to the direction of the principal strain and continuously rotate as the principal strain direction changes. The second is the fixed crack model, where cracks also initially form perpendicular to the principal strain direction, but the orientation is locked once a crack appears. The software also contains a combination of both. As for the fixed crack, a value for the shear retention between 1 and 0 is needed, meaning 1 is full shear and 0 is no shear once the crack opens. This shear retention value is assumed to be 1 for the rotating crack, and therefore no value is required in the software. This decides whether the crack rotates or is kept fixed. (DIANA FEA, 2025) A fixed crack is preferred when wanting to clearly analyze the hinge formation in the masonry, this is useful when analyzing the collapse mechanism.

For this model, values such as Mode-I tensile facture energy (G_{ft}) and compressive fracture energy (G_{fc}) are required. When these values are not available, correlations can be used. For the tensile fracture energy, where f_t is the tensile strength of the masonry, as suggested by Rots, Hendriks, & Esposito (2024) according to Van der Pluijm in 1999.

$$G_{ft} = 0{,}16 * f_t$$

As for the compressive fracture energy, the suggested equation in DIANA FEA software where f_c refers to the compressive strength of the masonry.

$$G_{fc} = 15 + 0{,}43 * f_c - 0{,}0036 f_c^2$$

For modeling masonry in the software DIANA FEA, as another constitutive model that there is a specific material model called the “Engineering Masonry Model,” which is based on the concept of smeared cracking. This model is designed for use with masonry elements assigned as regular plane stress or curved shell elements. It is typically recommended for static nonlinear cyclic analyses or transient dynamic nonlinear analyses of structures. The model accounts for two distinct stiffnesses in the x and y directions: the x-direction aligns with the bed of the brick, while the y-direction is perpendicular to the head joint. It also simulates several failure mechanisms. (DIANA FEA, 2025) Analysis of head joint failure using this model has shown mixed results: in some cases, the step cracking pattern is realistic, while in others it tends to overestimate damage. It’s important to note that this model was originally developed based on wall analyses.

2.3.6.3 Backfill material modelling

The backfill material can be any type of soil. There are many ways the soil can be modelled in a non-linear elastic way. These include Von Mises and Tresca plasticity, Mohr-Coulomb and Drucker Prager, and extended hardening soil model.

The Mohr-Coulomb constitutive model is the most commonly used to represent soil. This theory combines normal and shear stresses to determine the failure of the material. Failure is defined by an envelope, so any point falling on the failure envelope represents shear failure, while any point above the envelope cannot exist since the failure condition has already been reached. Often the values to create this envelope are determined in the laboratory using the principal stresses. The equation is described in Figure 11.

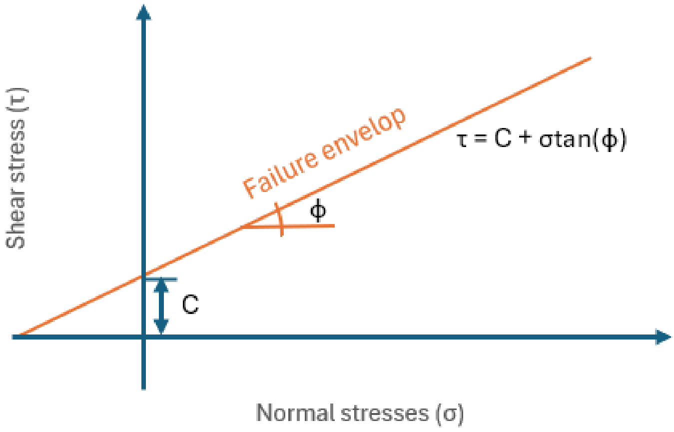

Figure 11. Mohr-Coulomb model

2.3.6.4 Interface modelling

For the interfaces, a Coulomb friction model was chosen. Interfaces between two materials generally develop friction, which can be represented by this model. The Coulomb friction model is similar to the Mohr-Coulomb model presented previously, but it is applied specifically to interfaces. It governs both sliding and opening/closing behavior. The shear resistance follows the same Coulomb criterion, when the shear stress reaches the failure limit, in this case, sliding occurs. In addition, the model includes a normal law that controls opening and closing of the interface, which is governed by the normal stiffness assigned to the contact surface. (DIANA FEA, 2025)

The normal and shear stiffnesses that can be used for this model, according to DIANA FEA (2025) the initial normal stiffness (K_n) and shear stiffness (K_t) can be calculated as:

$$K_n = 100{\sim}1000 \frac{E_{adj}}{l_{el}}$$

$$K_t = \frac{K_n}{10{\sim}100}$$

Where E_{adj} is the Young’s modulus of the adjacent material with the lowest modulus and l_{el} is the length of the element.

As for the calculation for the cohesion and friction angle, these can be obtained by using as a suggestion made by PLAXIS (2018):

$$C_i = R_{inter} * C_{soil}$$

$$\tan(\varphi_i) = R_{inter} * \tan(\varphi_{soil})$$

Where C is cohesion, R_{inter} is the reduction factor for the interface which varies depending on the interface properties and φ is the friction angle.

2.4 Assessment of existing structures

The assessment of masonry structures is typically carried out from a macro perspective by modelling the masonry structure as a continuum material, as evaluating each individual brick or stone in detail would be highly time-consuming and impractical. To make the process more efficient, though potentially less precise, the structure is usually analyzed with analytical calculations or is calculated using limit analysis. To guide this process, a system of assessment levels has been developed, allowing for a level approach that balances accuracy with practicality.

There are four defined levels of structural assessment:

- Level I involves basic hand calculations and the use of standard tables from design codes.
- Level II includes linear modeling techniques to analyze structural behavior.
- Level III applies nonlinear modeling, which captures more complex behaviors of materials and interactions.
- Level IV consists of proof load testing, where actual loads are applied to the structure to assess performance directly.

The first level is the simplest and quickest to perform, with a large safety margin built in. Failing to meet Level I requirements by a low margin doesn’t necessarily mean the structure is unsafe, it just indicates that a more detailed analysis (higher level) is needed to confirm the structure’s capacity. As the levels increase, so do the level of detail, computational effort, and cost. This process is often illustrated visually, as in Figure 12.

For this reason, it's generally recommended to begin at Level I and proceed upward only as needed, collecting more specific information at each step to determine whether the structure is safe. As for Level IV, the proof load test does not determine the exact failure load of the bridge. Instead, a controlled load is applied within a predefined margin to avoid collapse while still providing a high level of confidence in the structure’s ability to carry the required loads. However, it only makes sense to move through the assessment levels if initial results suggest the structure’s performance is close to the required capacity. (Lantsoght, Yang, & van der Veen, 2022)

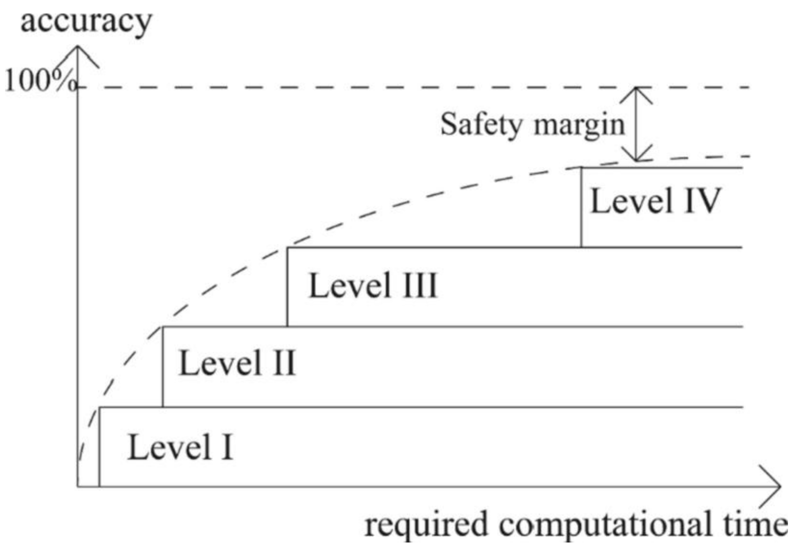

Figure 12. Levels of assessment of a structure (Lantsoght, Yang, & van der Veen, 2022)

To perform an assessment, enough information should be collected from the structure. From the location and the date to construction plans and material testing. Visual inspection is part of a preliminary assessment and having other information as from monitoring devices is often useful. Even though monitoring a structure can also be done with visual inspection, the devices can be used for a direct measurement to check the state of the structure. The devices include measurements of cracks, deflections, vibrations or even settlements. The data can be more precise, can have periodic monitoring and can contribute to an early detection of problems, and help engineers with decision making. The information gathered from the monitoring devices can be used for any level of assessment, but the more information the higher the level of assessment can be performed.

Existing bridges often show signs of deterioration, with cracking being one of the most common indicators. When assessing a bridge, it’s important to identify any cracks and investigate the underlying causes. Cracks may form due to various reasons, such as excessive loading or, more commonly, differential settlements. Proper modeling of the bridge can provide valuable insights and help determine the most likely cause of the cracking, supporting a more accurate and informed assessment.

2.5 Tests of masonry arch bridges

Over the years, numerous tests have been conducted to better understand the behavior of masonry arch bridges. Some of these tests focused specifically on the arch itself, while others aimed to analyze the behavior of the backfill soil. Records of laboratory-scale tests in controlled conditions date back as early as 1717. Field tests, particularly those carried out between the 1980s and 1990s, explored various structural aspects including arch failure mechanisms, soil-structure interaction, the role of backfill and spandrel walls as contributing structural elements, and the effects of ring separation (Sarhosis et al., 2016).

As reviewed by Sarhosis et al. (2016), a wide range of experimental studies has explored soil-structure interaction. These include tests by Darvey (1953); Harvey, Vardy, Craig, and Smith (1989); Melbourne and Walker (1990); Melbourne (1991); Fairfield and Ponniah (1994); Harvey, Smith, and Wang (1994); Melbourne and Gilbert (1997); Hughes, Davies, and Taunton (1998); and Gilbert et al. (2006). These studies investigated how loads are distributed through the backfill to the arch, the response of the soil, and the mutual interaction between soil and structure. A key finding from this body of research is that a greater amount of backfill generally increases the collapse load. Moreover, the type of backfill plays a crucial role: denser materials with higher internal friction angles provide better support, as demonstrated by Gilbert (1993) and later confirmed by Gilbert et al. (2006).

Spandrel walls have also been shown to significantly contribute to the structural performance of masonry arch bridges. Tests by Darvey (1953) and Royles and Hendry (1990) indicated that well-connected spandrel walls can enhance the arch's load-bearing capacity by distributing loads more effectively. The presence of cracks within the structure does not necessarily indicate a reduction in capacity, as the location and severity of the damage play a more significant role.

Other findings revealed that the position of the applied load influences both the failure mechanism and the magnitude of the collapse load. Ring separation, a phenomenon where individual rings of multi-ring arches begin to behave independently, was also studied. Hendry, Davies, and Royles (1985), and later Melbourne, Gilbert, and Wagstaff (1997), found that ring separation could reduce a bridge's load-bearing capacity by 33% to 71%, depending on its size and construction.

These various experiments, each with its specific objectives, collectively help deepen the understanding of the composite action in masonry arch bridges. When test results show consistent behavior across different scenarios, the probability increases that similar effects can occur in real-world structures. This consistency also helps identifying the causes of observed damage, such as cracking, deformation, or failure, and in refining models to predict structural behavior with greater accuracy.

One of the latest tests was performed in United Kingdom as a collaboration between University of Sheffield and the University of Leeds in 2024. They made a large-scale masonry bridge and tested its capacity. They also measured displacements under the arch and on the side of the spandrel walls. This test is described in more detail section 3.1 and is used as a benchmark for this research.

Chapter 3 Numerical modelling of a masonry arch bridge

This chapter describes the development and implementation of the numerical models used to simulate the behavior of a masonry arch bridge. The modelling process is based on a benchmark full-scale experimental bridge tested in the United Kingdom, which provides the geometric configuration, material properties, and loading conditions used for calibration and validation. Both 2D and 3D models were made using DIANA FEA, incorporating constitutive models and interfaces to represent the interaction between masonry and soil. The chapter outlines the modelling strategy, boundary conditions, material properties, mesh configuration, and analysis parameters; establishing the framework used to evaluate the structural response and to compare different modelling approaches.

3.1 Case scenario or benchmark

The modeling of the masonry arch bridge in this study is based on real experimental data obtained from a full-scale 3D bridge tested under controlled laboratory conditions. These tests were conducted by the University of Sheffield and the University of Leeds. The bridge was subjected to three loading scenarios (low, medium, and high loads) and the resulting data include material properties, geometric specifications, load locations, and detailed response behavior. Important results recorded during the tests include crack propagation, stiffness changes under load, radial displacements of the arch, and out-of-plane deformations.

This information is essential for validating the numerical model. The material properties and geometric parameters used in the simulation are directly taken from the experimental setup, as documented in the published research. By comparing the model’s results against the laboratory data, the reliability and accuracy of the simulation can be confirmed. This process not only enhances understanding of the structural behavior of masonry arch bridges under different loading conditions but also provides a foundation for applying similar modeling techniques to other bridges with varying geometries or material properties.

Regarding loading methods, two approaches were used during the physical testing: load control and displacement control. Load control was used during the low and medium load phases of the test, allowing displacement measurements to be directly compared with numerical results. Displacement control was used in the high-load phase, which aimed to push the bridge toward failure (Ultimate Limit State). This method is preferred in such cases to avoid sudden collapse by incrementally increasing displacement and monitoring the resulting forces. It enables the test to be stopped at the moment when the force response begins to diverge, signaling structural failure.

The test bridge was constructed using clay bricks bonded with mortar. Each brick measured 215 mm × 102,5 mm × 63 mm. Limestone was used as the backfill material, and no asphalt or other surfacing layers were applied. The construction process followed common procedures used in similar past laboratory experiments in the UK. First, a reinforced concrete wall (exact reinforcement details not specified) was built to retain the backfill. Polystyrene slabs were then installed to replicate the behavior of real-world spandrel walls. Following this, the abutments were constructed, and a framework was set up to form the masonry arch and spandrel walls. Backfill was added in compacted layers, although the compaction percentage was not specified. A diagram illustrating the full test setup and geometry is provided in Figure 13.

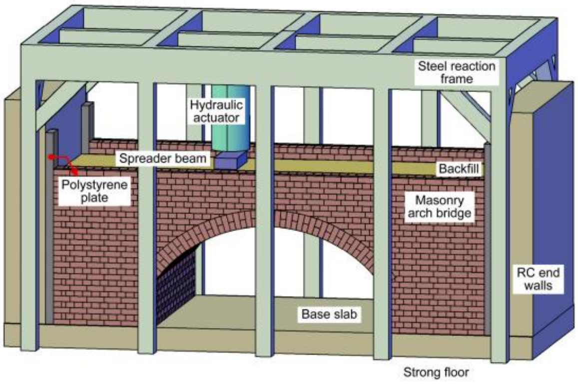

Figure 13. Test set-up (Liu et al., 2024)

To apply the load during testing, a steel frame was assembled to support the hydraulic actuator, as observed in Figure 13. Steel plates, two types were used to transfer the load onto the backfill surface. These plates ensured even load distribution and consistency throughout the test.

A smaller, similar steel structure was built to support the linear variable differential transformers (LVDT), which measured radial displacements at 15 evenly distributed points beneath the arch. Potentiometers and accelerometers were mounted on a separate steel frame to monitor deformations in the abutments and spandrels, also evenly spaced throughout the masonry structure (see Figure 14, Figure 15, Figure 16 and Figure 17). Additional steel frames were installed to hold monochrome cameras used for digital image correlation (DIC).

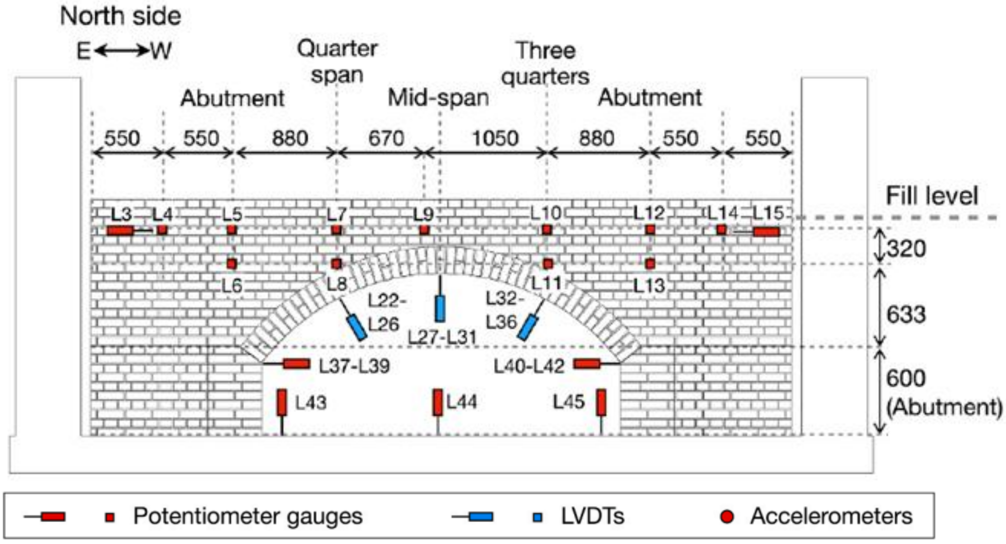

Figure 14. Measurement devices for the north side (dimensions are in mm) (Sarhosis et al., 2024)

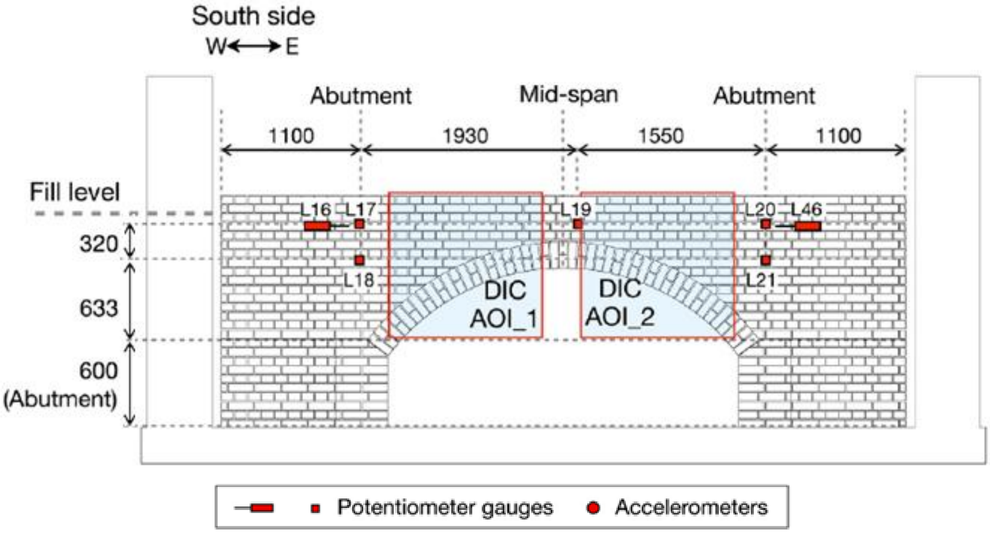

Figure 15. Measurement devices for the south side (dimensions are in mm) (Sarhosis et al., 2024)

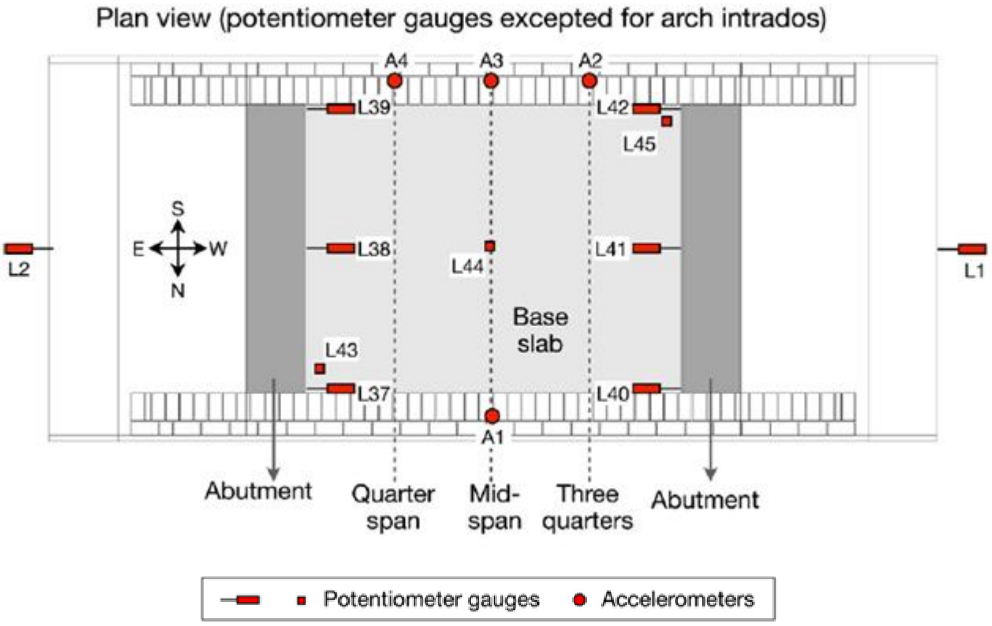

Figure 16. Potentiometer locations for the plan view (Sarhosis et al., 2024)

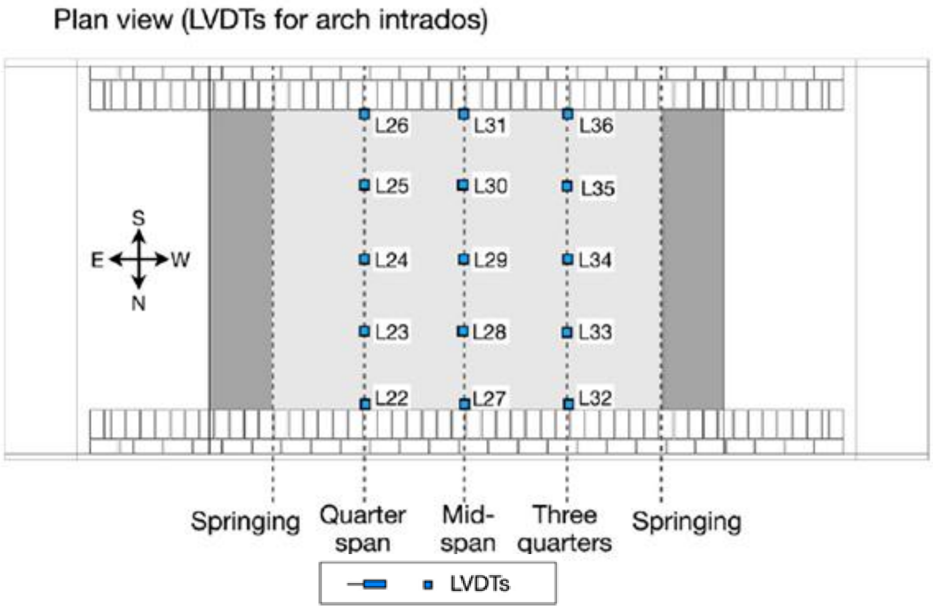

Figure 17. LVDT locations for the plan view (Sarhosis et al., 2024)

This section provides a physical description of the test setup to support understanding of the benchmark.

The bridge was constructed in a laboratory under controlled conditions. The tested structure was a 5,68 meter masonry arch bridge subjected to three types of loading: low load (150 kN), mid load (250 kN), and high load (560 kN or until failure). The dimensions are shown in Figure 18, Figure 19, Figure 20 and Figure 21.

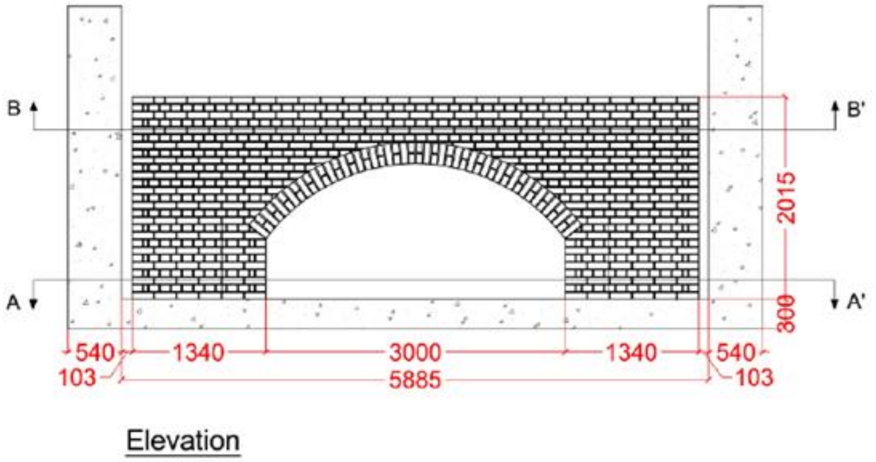

Figure 18. Dimensions of the test bridge front view (mm) (Sarhosis et al., 2024)

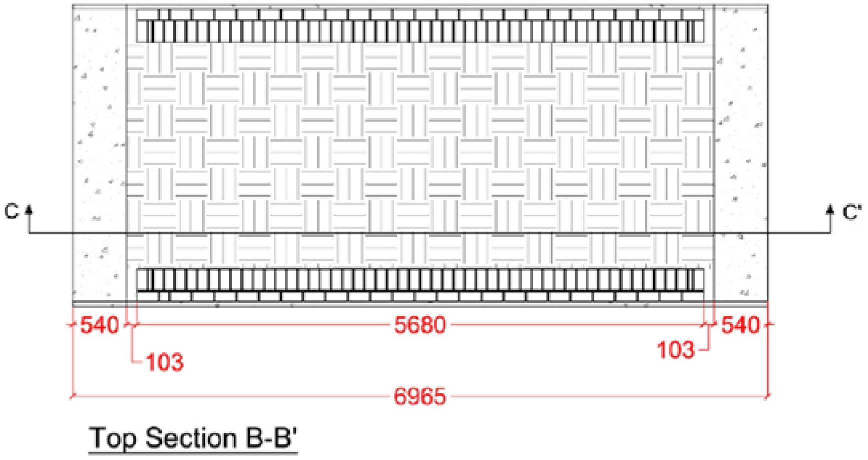

Figure 19. Dimensions of the test bridge section B-B' (mm) (Sarhosis et al., 2024)

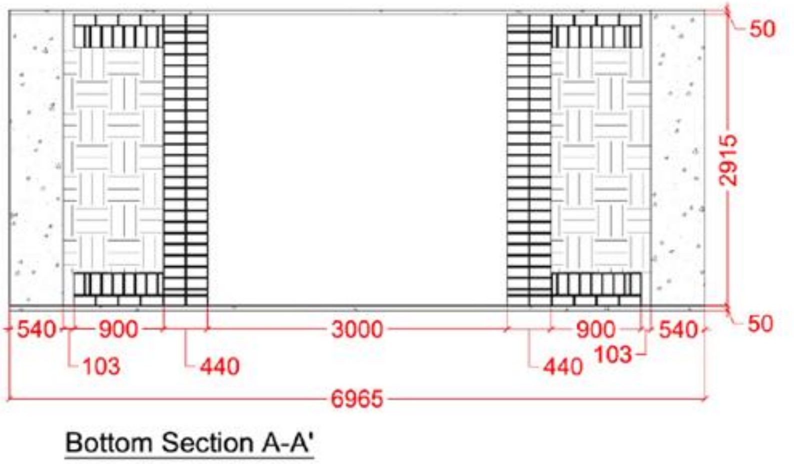

Figure 20. Dimensions of the test bridge section A-A’ (mm) (Sarhosis et al., 2024)

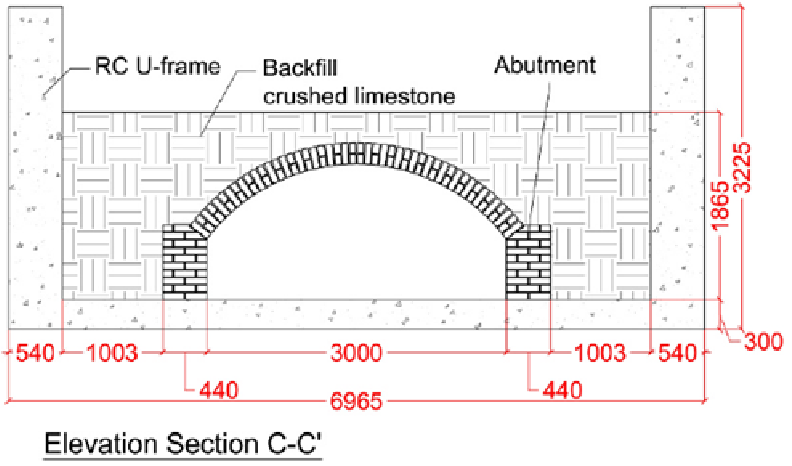

Figure 21. Dimensions of the test bridge section C-C’ (mm) (Sarhosis et al., 2024)

While most dimensions of the bridge were provided in the test documentation, the exact geometry of the arch was not explicitly specified. For modeling purposes, the arch was recreated using the measured arch height and a constant radius of curvature, aligned as closely as possible with the 36-degree inclination of the abutments.

The material characteristics that were determined in the laboratory that are of interest for this research are listed in the Table 2.

Table 2. Laboratory properties

Property	Symbol	Value	Units
Young's modulus of masonry	E_m	10128	MPa
Mortar density	ρ_j	1680	kg/m^3
Brick density	ρ_u	2470	kg/m^3
Limestone density	ρ_b	2150	kg/m^3
Compressive strength of masonry	$f_{c,m}$	30,84	MPa
Cohesion at brick-to-mortar interface	C	0,4	MPa
Friction angle at brick-to-mortar	φ	44,9	Degree
Friction angle of limestone	φ_b	47,8	Degree

The loading was applied using nine 300×300 mm steel plates for the low and mid-load cases, and two 300×750 mm plates for the high-load case. These plates were placed on top of the backfill to distribute the load uniformly.

In total, 25 tests were carried out: each of the nine plates was loaded once for both the low and mid-load tests, while the high-load tests involved one load applied on one side and two loads applied on the other side of the bridge. The arrangement of these plates is shown in Figure 22 and Figure 23.

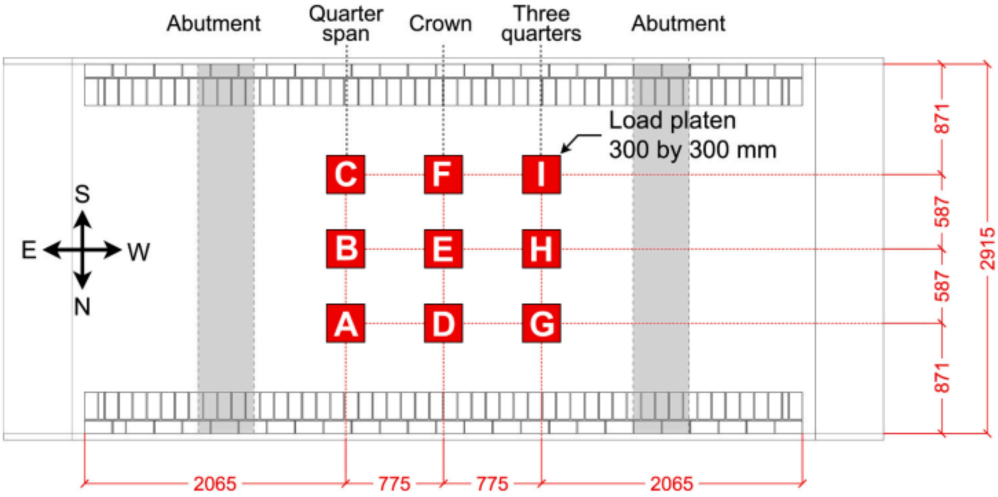

Figure 22. Location of plates for low and mid loads from top view (all units are in mm) (Sarhosis et al., 2024)

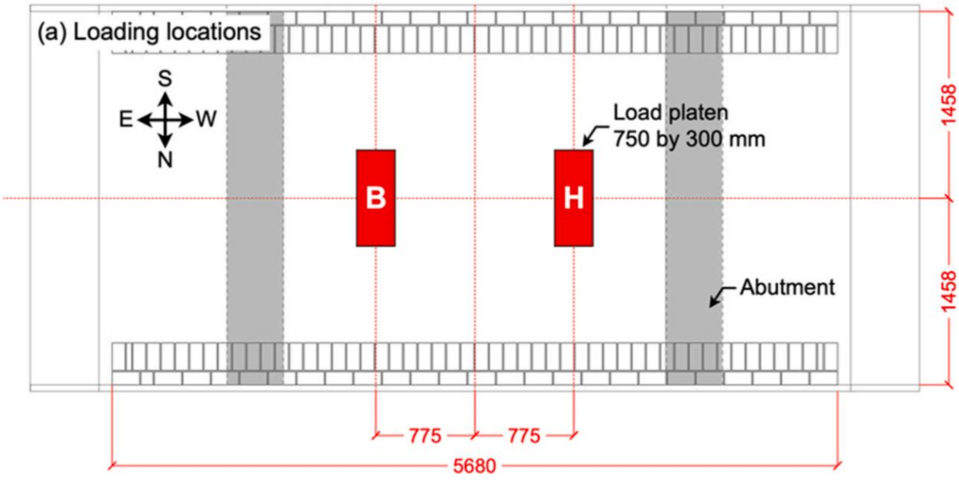

Figure 23. Location of plates for high loads from top view (all units are in mm) (Liu et al., 2024)

The tests performed were 25 tests but the information available is for 23 tests. The ones relevant for this research are described in Table 3. For the information for the rest of the test it can be found in the appendix in Table A 1.

Table 3. Relevant tests performed in the benchmark

Test No.	Plate locations	Type of load	Level	Loading area [mm]
T5	E	Static and cyclic	Low-load (150kN)	300x300
T8	B	Static and cyclic	Low-load (150kN)	300x300
T18	E	Static and cyclic	Mid-load (250 kN)	300x300
T20	B	Static and cyclic	Mid-load (250 kN)	300x300
T22	B	Static	Failure-load	750x300

3.1.1 Relevant results from the laboratory test

From the test, data were collected on elements such as radial displacements beneath the arch, cracking patterns, and out-of-plane deformations of the spandrel walls. Measurements were recorded at all tested points; however, only the most relevant results are presented in Table 4 and Table 5.

Table 4. Radial displacements in mm from load application on plate B and E (Sarhosis et al.,2024)

Load location	**B plate**			**E plate**		
LVDTs	L22-L26	L27-L31	L32-L36	L22-L26	L27-L31	L32-L36
Low load (150kN)	-0,109	-0,018	0,036	-0,01	-0,147	0,004
	-0,207	-0,059	0,056	-0,045	-0,344	-0,064
	-0,309	-0,072	0,067	-0,07	-0,652	-0,103
	-0,189	-0,037	0,061	-0,069	-0,356	-0,069
	-0,093	-0,007	0,033	-0,041	-0,188	-0,031
Mid load (250kN)	-0,385	0,022	0,258	0,040	-0,365	0,002
	-0,645	-0,047	0,371	0,044	-0,628	0,001
	-0,909	-0,08	0,416	0,010	-1,288	-0,024
	-0,616	-0,024	0,366	-0,016	-0,649	0,001
	-0,346	-0,007	0,222	-0,027	-0,358	-0,005

Table 5. Radial displacements in mm from load application on plate B (Liu et al., 2024)

Load location	**B plate**		
LVDTs	**L22-L26**	**L27-L31**	**L32-L36**
High load (560kN)	-1,678	1,592	2,252
	-2,819	1,287	2,466
	-3,824	0,887	2,412
	-2,877	1,172	2,240
	-1,615	1,379	1,926

The initial stiffnesses were calculated from the measured results, specifically using the values between 0 and approximately 10 kN. This approach differs from the method used to calculate stiffnesses in the referenced research. The decision was based on the observed behavior of the actual load-displacement curve and the expected response after incorporating nonlinear properties into the model. The calculated initial stiffness values are presented in Table 6.

Table 6. Stiffnesses for the laboratory tests

Location	**Initial Stiffness [kN/mm]**	**Average Stiffness [kN/mm]**
Side low load (From Test T8)	734	619
Side mid load (From Test T20)	504	
Center low load (From Test T5)	317	342
Center mid load (From Test T18)	367	

3.2 Modelling strategy

Several models were considered, with their parameters varying depending on the intended purpose. To solve the questions of this research, the models were developed as described in this section.

Initially, a 3D linear elastic model was made (see Figure 24) to compare it to the test results in the linear elastic range, specifically the initial stiffness. Due to the comparison material calibration was carried out to ensure that the properties that were used were comparable. This involved adjusting material characteristics to match the real behavior in the 3D model. As for the nonlinear model, an adjustment of the soil material properties was made by analyzing the material alone.

After, a load spread analysis was made comparing a 2D and a 3D model in the same way as previously (linear elastically), to be able to determine if a 2D model can be representative. For these two models to be comparable, the 3D model had the spandrel walls removed (as seen in Figure 25). Since the structure is symmetrical, the loads that were considered are the loads on plates B and E. This is made to understand the load spread in the third dimension and based on this determine an equivalent width for the 2D model (Figure 26).

A 3D model (including spandrel walls, Figure 24) was created with nonlinear properties, so that stiffnesses, peak load capacity, cracking patterns and ductility could be directly compared with the benchmark. With this determine if the model can closely represent the real case scenario.

With a comparison between the 2D and the 3D model without spandrel walls and a nonlinear analysis, the equivalent width can be determined and compared to the one obtained when running a linear analysis comparison.

A spandrel wall effect is determined by comparing the 3D models, the one including the spandrel walls and the one without them. The comparison includes elements like stiffness, peak load capacity, cracking patterns and ductility, determining how much of an effect the spandrels can introduce in the system.

The 2D and 3D models were created using the updated parameters. All 2D models share the same geometry; the differences lie in the applied loads and material properties. The 3D models, with and without spandrel walls, are shown as they were developed in the modeling software (see Figure 24 and Figure 25), it does contain a variation in the location of the load to match the location corresponding the tests. And the 3D model with spandrel walls in the nonlinear analysis, had a variation regarding the foam, where the foam was substituted with a disconnection.

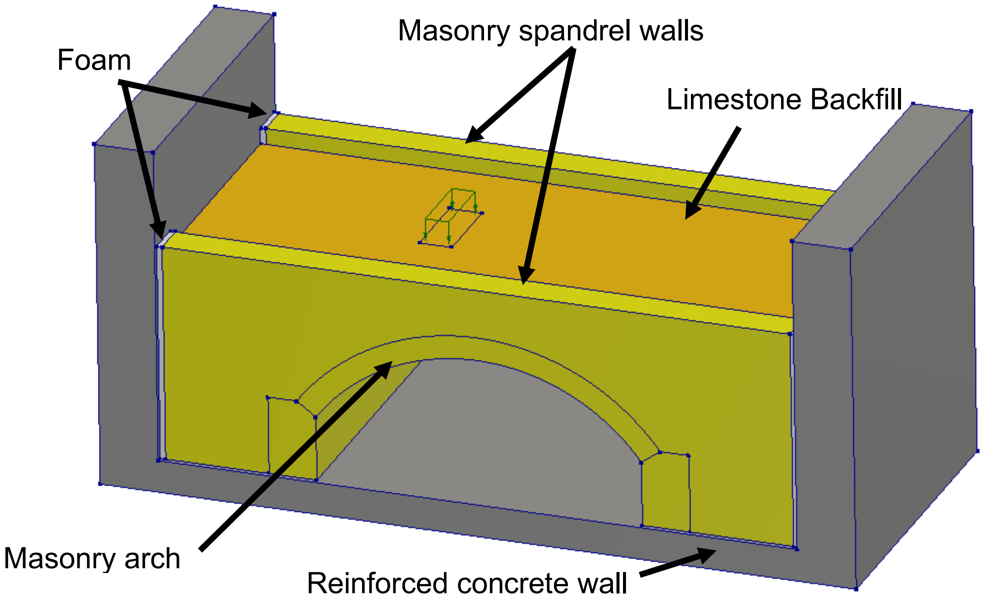

Figure 24. 3D model with spandrel walls

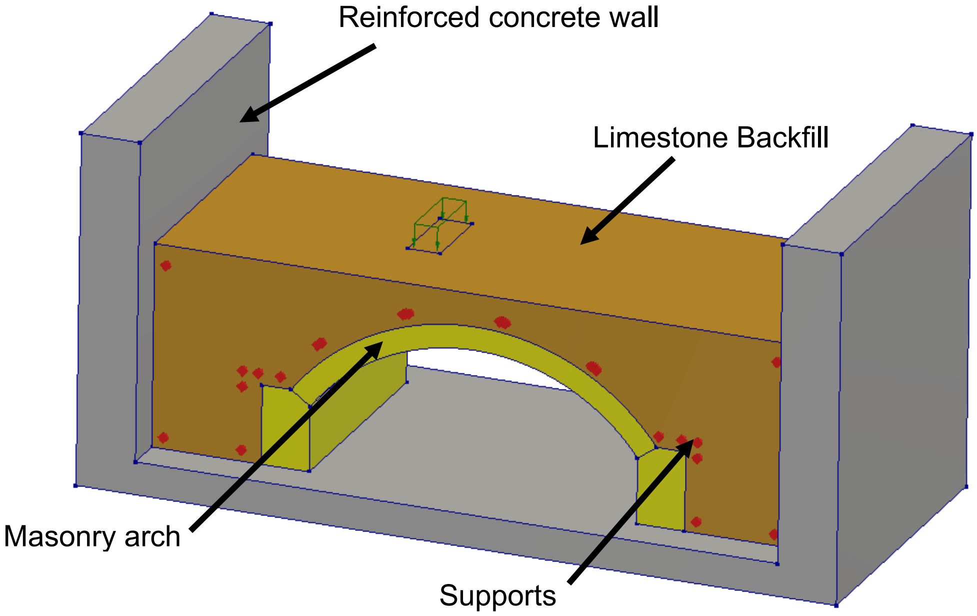

Figure 25. 3D model without spandrel walls

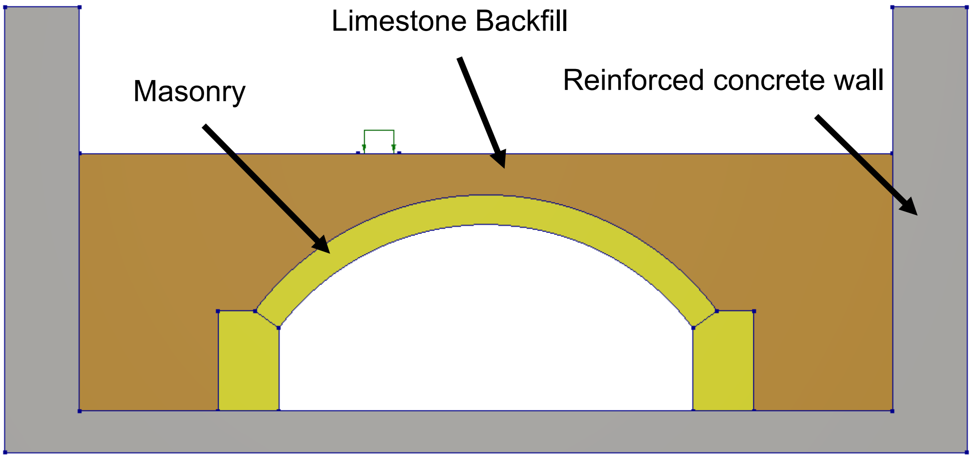

Figure 26. 2D model with load cases and boundary conditions

The models described above all have a reinforced wall to make the model as similar as possible to the benchmark. Although, this could be done differently, replacing the concrete walls with supports instead, but in this case the concrete wall acts as a support to the soil. The concrete wall does need to be held, because there is an upward reaction caused by the floor. This element has 6 degrees of freedom as for the 3D model, but because the bottom surface was supported, then 3 degrees of freedom were limited (translational in x, y and z). As a consequence of this being limited, rotations are also limited. As for the 2D model, similar scenario, with restricting translational degrees of freedom (x and y directions) along the bottom edge of the concrete wall.

In the case of the 3D model without the spandrel walls, the soil would be free to move, sliding off the bridge. Spandrel walls are mainly restricting this movement, and therefore, the horizontal direction (y direction) is restricted in the surface by adding supports as shown in Figure 25. Even though the walls don't fully restrict the movement in the out-of-plane direction, the supports help making this model a comparable one to the one with walls.

3.3 Boundary conditions

The boundary conditions of the model are relatively simple due to the presence of a reinforced concrete wall, which retains the soil and supports the spandrel walls. However, to ensure stability, all models include supports at the bottom of the reinforced concrete slab. These supports prevent horizontal and vertical movement.

In the sensitivity analysis, where the spandrel walls are removed, an additional boundary condition is applied to the soil. This adjustment compensates for the absence of the walls by ensuring the soil remains adequately supported, without adding extra stiffness to the system. This can be observed in Figure 25 where supports are located to restrain the lateral movement of the soil as a way to substitute the spandrel walls. This approach helps isolate and identify the structural contribution of the spandrel walls. Additionally, it allows the 2D model to be comparable to the 3D model, since spandrel walls cannot be explicitly included in the 2D representation.

3.4 Material properties

3.4.1 Linear elastic material properties

Some material properties were not reported in the test documentation; as a result, certain values necessary for the modeling process were missing. To address this, typical values from literature were used for some materials, while others were estimated through empirical correlations

Initially, for the 3D analysis, all materials were modeled as linear elastic. The material properties used in the model are presented in Table 7, as the initial values that were used.

Table 7. Material properties for the linear elastic model (initial values)

Material	Property	Value	Units
RC wall	Young's modulus [1]	25091	MPa
	Poisson's ratio [2] (ACI, 2019)	0,15	-
	Mass density [2] (ACI, 2019)	2400	kg/m^3
Steel plates	Young's modulus [2] (ACI, 2019)	200000	MPa
	Poisson's ratio [2] (ACI, 2019)	0,3	-
	Mass density [3]	0	kg/m^3
Backfill	Young's modulus [2] (Karlinasari & Rachmadan, 2020)	70	MPa
	Poisson's ratio [2] (Lei et al., 2014)	0,27	-
	Mass density specification	Dry density and porosity	
	Density [4]	2150	kg/m^3
	Porosity [2] (Domenico & Schwartz,1990)	0,37	-
	Initial stress	Isotropic	-
	K0 [2] (Duncan & Wright, 2005)	0,5	-
	Shear/ pressure	Mohr-Coulomb	-
	Friction angle [4]	47,8	degrees
	Cohesion [2]	0,001	MPa
Masonry	Young's modulus [4]	10128	MPa
	Poisson's ratio [2] (Ghiassi, et al., 2019)	0,2	-
	Mass density [1]	2340	kg/m^3

Material	Property	Value	Units
Polystyrene	Young's modulus ^{2} (Tang et al., 2019)	1,24	MPa
	Poisson's ratio ^{3}	0	-
	Mass density ^{3}	0	kg/m^3

[1] Determined with mechanical/analytical formulas

[2] Taken from literature/typical values

[3] Value of steel and polystyrene plate was not used for the model because it doesn't affect the performance

[4] Test values (see Table 2)

For the linear 2D model, the same material properties were used as in the 3D model, with the exclusion of properties for the foam, which was only used for the linear model, and with the adjustment in the masonry Young's modulus.

Several material properties for the materials used were missing. Therefore, the values used are either determined from mechanical or analytical formulas, a typical value generally taken from literature, or values taken from the test that were performed for the materials of the bridge.

When wanting to apply the total strain model, the missing values for masonry were estimated. To estimate the density, a composite value was calculated based on the densities of the bricks and mortar, according to their respective proportions in the masonry. The tensile and compressive stress-strain curves were defined based on the theoretical behavior of masonry, although the specific values used in the model vary.

Due to missing values and high values for masonry, a calibration of the model was made. The 3D model was developed using the geometric dimensions provided by Sarhosis et al. (2024). The 3D model includes the spandrel walls as well as the polystyrene slabs positioned between the reinforced concrete wall and the spandrels. This model setup is relatively straightforward geometry wise, and the materials used are the ones already mentioned.

The first linear 3D model had results for initial stiffness, these were compared with the test results. The stiffnesses were calculated using the following equation, where the radial displacement is located along the bottom of the arch in a point underneath the load.

$$Stiffness = \frac{Load}{Radial\ displacement}$$

Due to high stiffnesses in the linear 3D model, a sensibility analysis was made for the calibration of the materials. When comparing the stiffness of the 3D model to the experimental results, it was found that the model consistently overestimated the structural response. To address this difference, a sensitivity analysis was carried out to calibrate the material properties. The following key parameters were individually varied during the analysis:

- Young's modulus of the masonry
- Young's modulus of the backfill
- Young's modulus of the reinforced concrete wall

To facilitate the comparison, the data was normalized for both the side load (load applied on B plate) and the center load (load applied on E plate). As described in the equations below for the center load and the side load, where the average stiffness center is 342 kN/mm and the average stiffness side is 619 kN/mm, and the model stiffness is the one determined from the model in each position when the material property was changed.

$$Normalized\ stiffness\ center = \frac{Model\ stiffness\ center}{Average\ test\ stiffness\ center}$$

$$Normalized\ stiffness\ side = \frac{Model\ stiffness\ side}{Average\ test\ stiffness\ side}$$

For the model results, it is important to note that the radial displacements were derived by combining the displacements in both the vertical and horizontal directions and transforming them into a radial component. This calculation assumed that the LVDTs were oriented perpendicular to the tangent at their respective positions on the arch, and that the arch itself maintained a constant curvature (consistent with the assumptions used in the design).

When comparing the normalized stiffness of the model (Figure 27) with the young's modulus of the masonry, it becomes evident that the Young's modulus can be adjusted to match each individual test. This reduction in stiffness is reasonable since the value calculated from tests are usually overestimating this value because of the gap that exists between the tests and the real behavior of the materials as pointed out by Lourenco, 1994. For both load cases, the normalized stiffness of the bridge's reference values is calculated using the averages of the low and mid loads in Table 6. However, since the goal is to define a single representative value, an intermediate value was selected to provide a balanced calibration between both load application locations.

The analysis indicates that the most influential parameter was the Young's modulus of the masonry. The variation of the parameters showed a linear relationship with the overall initial stiffness of the model, highlighting the importance of accurately calibrating this parameter to match the experimental behavior

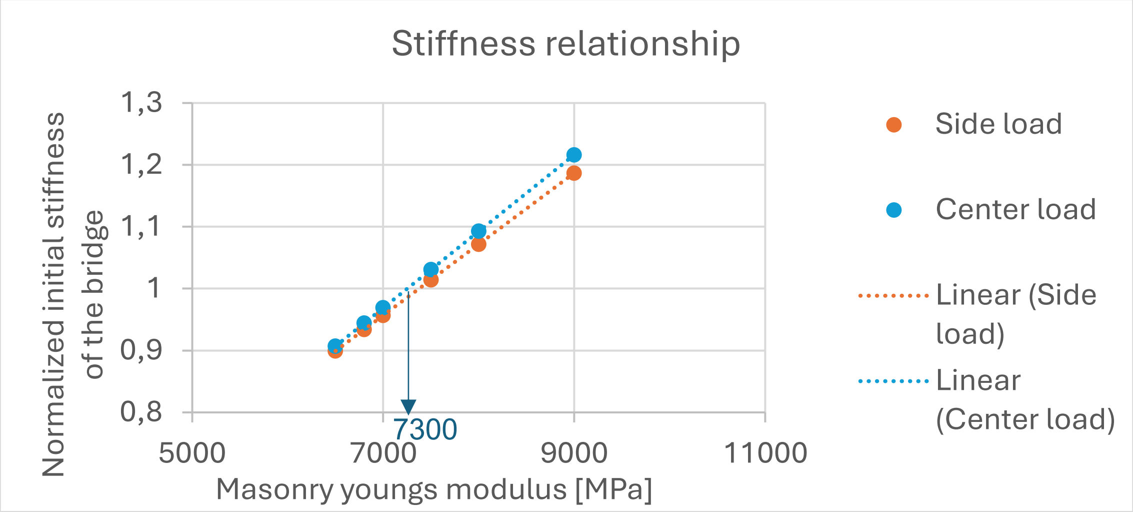

Figure 27. Stiffnesses relationship for material calibration.

As observed in Table 6 (and as was also the case for the linear 3D models) the stiffness is higher when the load is applied on the side of the arch compared to when it is applied at the center. This same behavior is observed in the current model when normalizing the stiffnesses. This is because a load placed closer to the support results in a shorter lever arm, which generates a smaller bending moment.

As demonstrated above in Figure 27, the calibrated value that has been modified (which was modified in the following models) is 7300 MPa for the masonry's Young's modulus This value is considered a reasonable estimate, as the laboratory-determined modulus by the researchers is on the higher end of the typical range for masonry. The Young's modulus for masonry that is used for the continuum model is 73% of the Young's modulus determined by the laboratory test. The results due to the change in stiffness from altering backfill and concrete Young's modulus can be observed in Table A 2.

As seen in the stiffness relationship, the comparison between the numerical results and the experimental results show a great consistency. The percentage difference remains under 1% when comparing the normalized stiffnesses. Meaning that the model in a linear elastic analysis is representative for the stiffnesses in both locations when the masonry Young's modulus is as indicated above.

3.4.2 Nonlinear material properties

In the nonlinear analysis, each material was assigned a more specific constitutive model, with the corresponding properties listed in Table 8, Table 9 and Table 10. For the reinforced concrete material model, an isotropic linear elastic model is used, for both the linear and the nonlinear analysis. Since the concrete material was not directly tested, its properties are introduced based on standard equations and assumptions. It is assumed that the reinforced concrete wall and slab were constructed to withstand the backfill without significant deformation. Because the exact dimensions and material properties of the walls and slab are not specified, their characteristics must be estimated from the available information. The primary role of these walls is to retain the backfill and prevent differential displacements in the bridge structure. Modeling these elements as linear elastic is appropriate, especially since the research and testing conducted on the bridge report no damage related to their performance. These exceptions were made also for the steel plates, and polystyrene slabs, which were modeled as linear elastic materials, as no signs of deterioration were reported. This approach ensures they fulfill their purpose in the bridge without introducing unnecessary complexity. Therefore, the properties used for these materials can be seen in Table 7.

As for the masonry, the young's modulus was adapted from the material calibration, the tensile strength was estimated using the cohesion and friction angle of the material, while the mode-I tensile fracture energy and compressive fracture energy were derived using empirical correlation equations shown in section 2.3.6.2. The complete set of material properties used in the model is provided in Table 8.

Table 8. Masonry nonlinear properties

Model	Masonry total strain	
Young's modulus [1]	7300	MPa
Poisson's ratio [2](Ghiassi, et al., 2019)	0,20	-
Mass density [1]	2340	kg/m^3
Crack orientation	Fixed	
Tensile curve	Exponential	
Tensile strength [1]	0,4	MPa
Mode-I tensile fracture energy [1]	0,064	N/mm
Crack bandwidth specification	Rots	
Reduction model	No reduction	
Compressive curve	Parabolic	
Compressive strength [3]	30,48	MPa
Compressive fracture energy [1]	24,8	N/mm
Residual compressive strength	-	MPa
Reduction model	No reduction	
Confinement model	No increase	
Shear retention function	Constant	
Shear retention (β)[4]	0,01	-

[1] Determined with mechanical/analytical formulas

[2] Taken from literature/typical values

[3] Test values (see Table 2)

[4] A discussion on the shear retention value and results of the models with a $\beta=0$ are in Appendix 7.1

Regarding the backfill properties, most values were not provided or directly tested. Consequently, typical values from the literature were used. The Young's modulus was set at the lower bound of the typical range for sand or gravel, considering the material composition is limestone. Poisson’s ratio was selected as an average value for this type of material. A small, non-zero cohesion value (a "dummy" value) was introduced to prevent numerical instability, as assigning zero cohesion caused the model to diverge.

The friction angle was obtained from laboratory test results (47,8°), and the dilatancy angle was approximated based on the friction angle, consistent with expected values for well-graded gravel. The remaining parameters were treated as initial estimates. All values used in the model are summarized in Table 9.

Table 9. Backfill nonlinear properties for the model (initial values)

Model	Mohr-Coulomb plasticity model	
Young's modulus [1] (Karlinasari & Rachmadan, 2020)	70	MPa
Poisson's ratio [1] (Lei et al., 2014)	0,27	-
Mass density specification	Dry density and porosity	
Density [2]	2150	kg/m^3
Porosity [1] (Domenico & Schwartz,1990)	0,37	-
Cohesion [1]	0,001	MPa
Fiction angle [2]	47,8	Degrees
Dilatancy angle [1,3] (Stacho et al. 2023)	17	Degrees
Friction hardening	Constant friction angle	
Tension cut-off (Based on principal stresses) [2]	0,2	MPa
Initial stress		
Type	effective stresses-isotropic	
K0[1] (Duncan & Wright, 2005)	0,5	-

[1] Taken from literature/typical values

[2] Test values (see Table 2)

[3] The value of 17 degrees was modified to 10 degrees for stability of the model

To be able to make a 3D nonlinear analysis, the parameters used for the soil needed to be adjusted, since the values from 17° to 11° of the values tend to have convergence issues when iterations are a maximum of 300. For this a block was modelled with containing the constitutive model of Mohr-Coulomb, supporting all the sides except for the top part like in Figure 28. This model had the same area for load application and the same mesh size as the 3D models of the bridge.

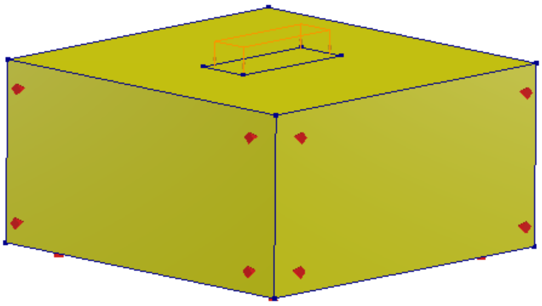

Figure 28. Soil block model for adjustment of parameters

The material model was according to the values presented in Table 9 with a small load application to avoid convergence issues. Because of the model having problems with convergence, all the parameters were varied one by one. This variation determined that the dilatancy angle was high. Therefore, the value that was tested to be in the high side but still managed to converge was 10 degrees. The rest of the values for each property remained the same.

The effect of the change in dilatancy angle can be observed in the Figure 29. As the dilatancy angle increases more iterations are needed to reach convergence, but the graph indicates a stiffer material when the dilatancy angle increases, therefore, a stiffer material would be expected if the dilatancy angle reaches 17 degrees.

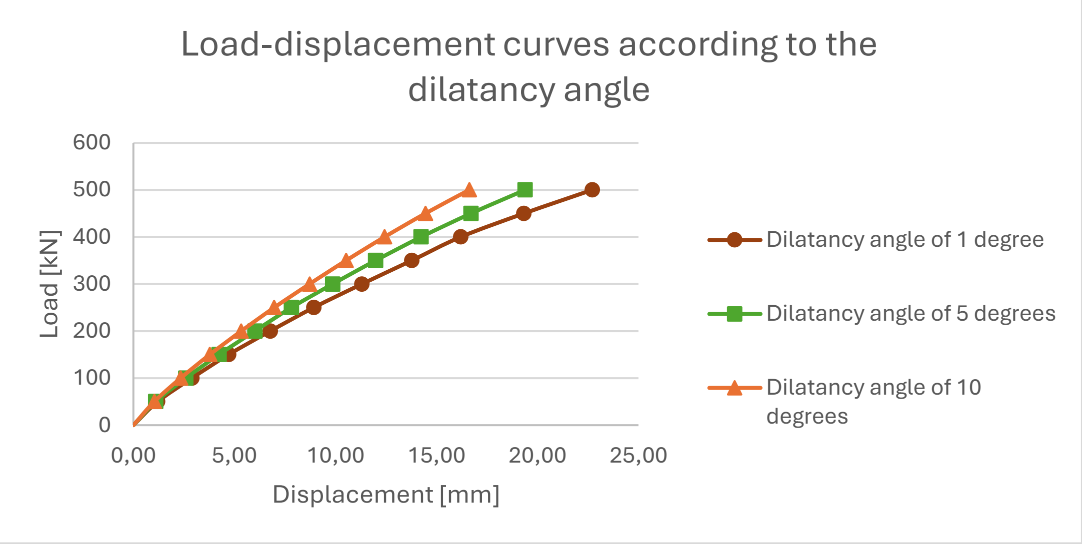

Figure 29. Effect of dilatancy angle in soil

The interface properties used in the 2D and 3D models are presented in Table 10. The interfaces vary depending on the type of contact. There are 4 types of contact:

- Soil to masonry: Coulomb friction model
- Soil to reinforced concrete: Coulomb friction model
- Masonry to concrete (side of spandrel): Disconnect or foam
- Masonry to masonry (arch to spandrel walls): Coulomb friction model

The friction angle and dilatancy angle were assigned based on standard values commonly used for interfaces between these two materials. The stiffnesses were calculated as described in section 2.3.6.4, using the adjacent material's properties.

Table 10. Interface nonlinear properties for the 3D model

Type of connection	Property	Value	Unit
Interface masonry spandrels to masonry arch (Coulomb friction)	Normal Stiffness modulus-z [1]	1000	N/mm^3
	Shear Stiffness modulus-x [1]	10	N/mm^3
	Shear Stiffness modulus-y [1]	10	N/mm^3
	Cohesion [3]	0,4	MPa
	Fiction angle [3]	45	Degrees
	Dilatancy angle [2]	0	Degrees
	Interface opening	Tension cut-off	
	Tensile strength [1]	0,27	MPa
Interface soil to masonry (Coulomb friction)	Normal Stiffness modulus-z [1]	700	N/mm^3
	Shear Stiffness modulus-x [1]	7	N/mm^3
	Shear Stiffness modulus-y [1]	7	N/mm^3
	Cohesion [3]	0,001	MPa
	Fiction angle [3]	47,8	Degrees
	Dilatancy angle [2]	0	Degrees
	Interface opening	Tension cut-off	
	Tensile strength [2]	0	MPa
Interface soil to concrete (Coulomb friction)	Normal Stiffness modulus-z [1]	700	N/mm^3
	Shear Stiffness modulus-x [1]	7	N/mm^3
	Shear Stiffness modulus-y [1]	7	N/mm^3
	Cohesion [1]	0,001	MPa
	Fiction angle [1]	41,4	Degrees
	Dilatancy angle [2]	0	Degrees
	Interface opening	Tension cut-off	
	Tensile strength [2]	0	MPa

[1] Determined with mechanical/analytical formulas

[2] Taken from literature/typical values

[3] Test values (see Table 2)

As for the 2D model and the 3D model without walls there are 4 types of interfaces, the connection between the soil and the reinforced concrete, the connection between soil and masonry, between masonry and concrete and between masonry and masonry for the connection between the arch and the spandrel walls. The one difference between the 2D and the 3D model in material properties relays in the extra dimension, still making use of the same values for the shared interfaces.

The interfaces can be seen in Figure 30 and Figure 31 with the color scheme that depends on the type of interface that was assigned.

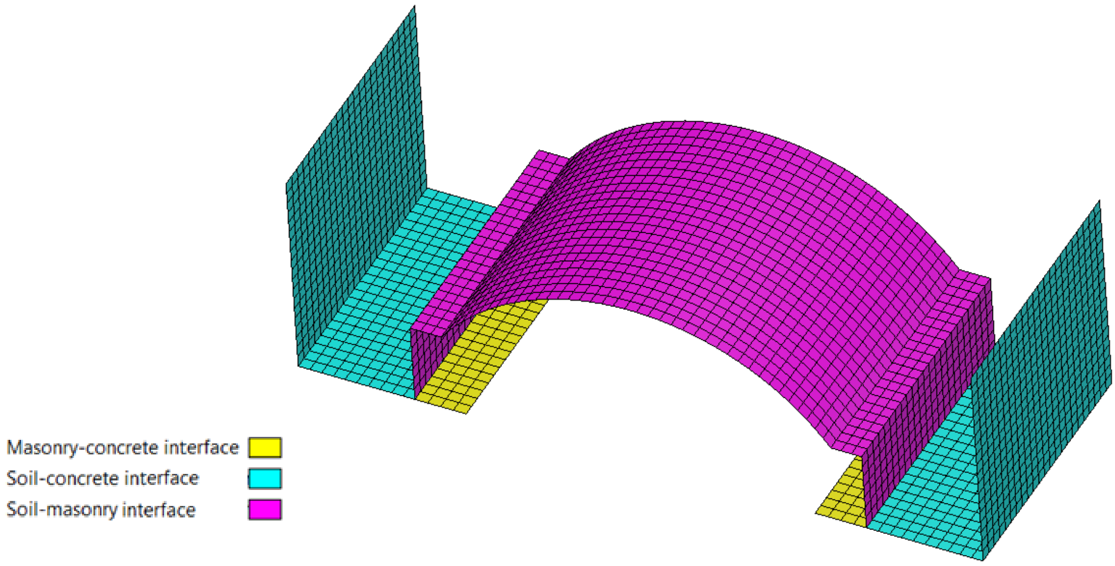

Figure 30. Interfaces for the model without spandrel walls

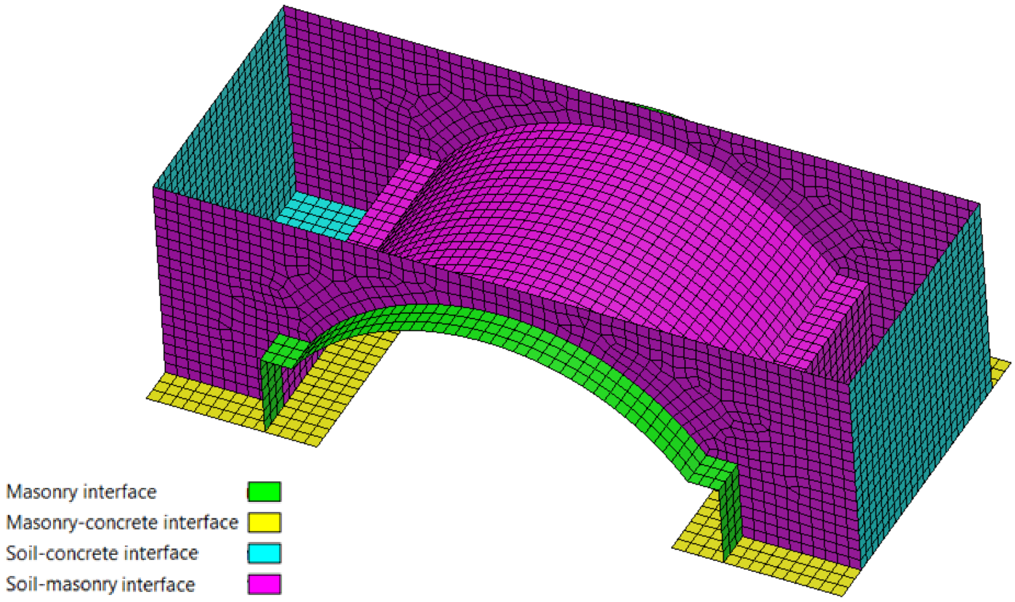

Figure 31. Interfaces for the model with spandrel walls

3.5 Meshing and analysis parameters

The meshing was performed using quadratic elements with quadratic mesh order where the integration scheme is a Gaussian 3x3. This approach allows for a relatively coarse mesh while still providing intermediate accuracy in the results. For the backfill and the reinforced concrete wall, a mesh size of approximately 150 mm was used, as these components are not critical and limited information is available for them. In contrast, the masonry elements were meshed with a finer resolution of approximately 100 mm. This meshing strategy was applied consistently to both the 2D and 3D models in both linear and non-linear models. The meshed model can be observed in Figure 32.

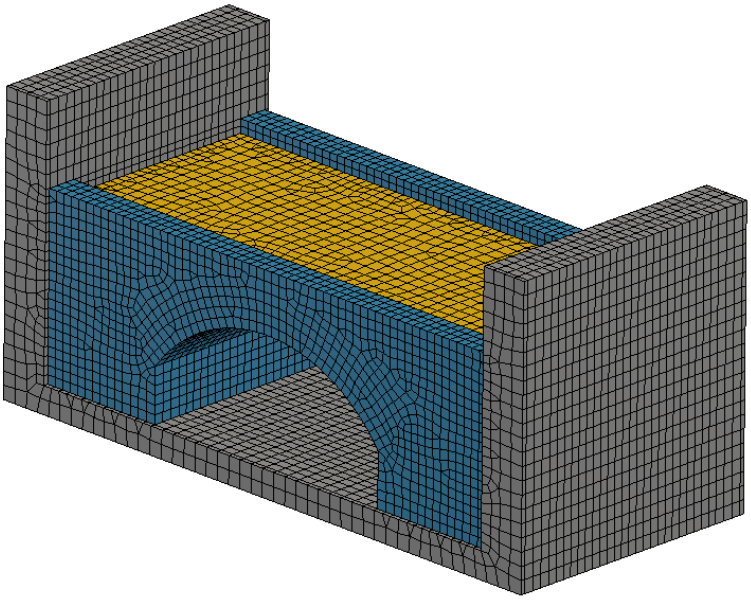

Figure 32. Meshed model

For the non-linear model analyses, the chosen iterative method was the secant (quasi-Newton) method since it's the most stable model, with a maximum of 300 iterations. Convergence was defined by satisfying both displacement and force norms, where force convergence tolerance is 0,01 and the displacement convergence tolerance is 0,02.

The analysis consisted of 3 phases:

- 1st: Only masonry with self-weight
- 2nd: Addition of backfill with initialization of stresses
- 3rd: Application of load (displacement control)

Chapter 4 Analysis of the outcome and discussion

The results obtained from the numerical analyses and their implications for the structural assessment of masonry arch bridges are presented in this chapter. The effect of the spandrel walls, backfill behavior, and soil-structure interaction on the global stiffness and peak load capacity are evaluated through comparisons between 2D and 3D models. The cracking patterns and load-displacement relationships are analyzed. The findings are interpreted and compared to the experimental data from the benchmark bridge to assess the accuracy and representativeness of the numerical models.

4.1 Spandrel wall effect on the bridge stiffness

As seen in the material calibration section, only the Young's moduli were changed for the original linear elastic properties. After the calibration of the material in a 3D model, the results were obtained to be able to determine the spandrel wall effect. The linear 3D models with and without spandrel walls were compared.

The stiffnesses were determined in the same way as it was done for the material calibration. Due to the calibration value, the stiffness obtained from the 3D model is very close to the one from the test and therefore the comparison is only made between the two models. To avoid confusion, the test results were not displayed in this section, but the results demonstrate also the effect that the spandrels most likely have in the real case.

This was done for both load application locations (center and side). Due to the model's symmetry and linear behavior, the analysis focused on locations in plates B for the side load, and E for the center load, in the low load (150 kN). Since it's a linear analysis, the values can later be extrapolated, if needed.

To understand the impact of the spandrels, the effect was analyzed at the side and the center of the structure. The results can be seen in Figure 33.

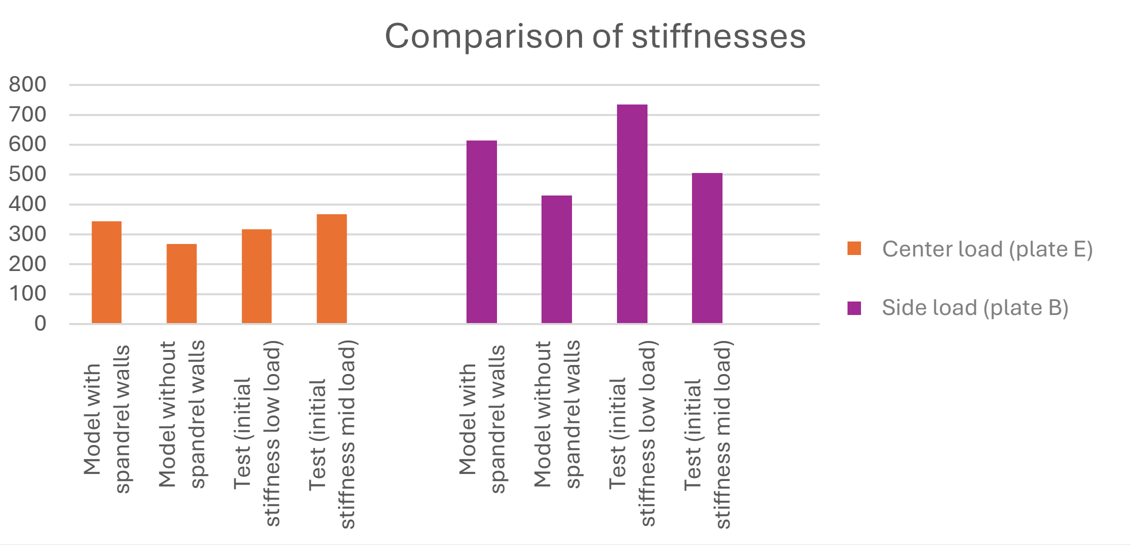

Figure 33. Center load and side load stiffness comparison

The results from the overall initial stiffness of the bridge indicate that replacing the walls with only lateral supports (to retain the backfill) leads to a decrease in stiffness of the bridge. This decrease in stiffness is approximately 43% to 29% depending on the location of the load. These findings are summarized in Table 11, as these are the critical points.

Table 11. Comparison of stiffnesses to evaluate effect of spandrel walls

Location of the load	Initial stiffnesses model **with** spandrel walls [kN/mm]	Initial stiffnesses model **without** spandrel walls [kN/mm]	Spandrel wall effect on the overall stiffness of the bridge
Side (plate B)	613,7	429,6	43%
Center (plate E)	344,3	267,4	29%

4.2 Effective width in 2D plane strain models

A 3D linear model excluding the spandrel walls was created to be able to make a fair comparison with a 2D model for the effective width determination. For this model, the walls were removed and were replaced with supports (see Figure 25) same as used for 4.1.The model was compared with the linear 2D model, varying the effective width to identify the load spread along the arch. The terms used are illustrated in Figure 34 and Figure 35.

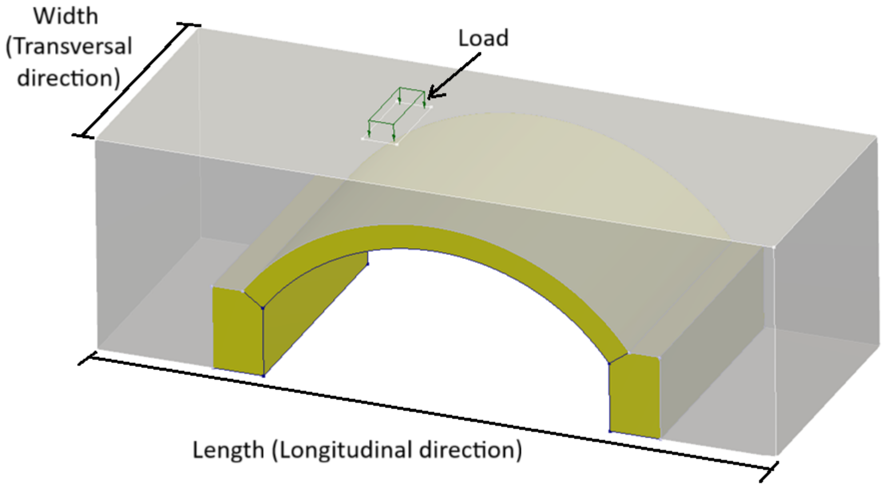

Figure 34. Notation for dimensions

For the 2D model the width was set to 1 m for simplicity. As a result, the applied load had to be adjusted to reflect an effective width, as illustrated in Figure 35. Since the model assumes uniform characteristics in the in-plane (transverse) direction, it does not account for the natural load distribution that occurs in reality. The effective width represents the extent to which the load spreads laterally before reaching the arch and serves to compensate for the absence of this three-dimensional load dispersion and the spandrel walls in the 2D model. This value is used to introduce a load that contains this effective width, which accounts for the load spread.

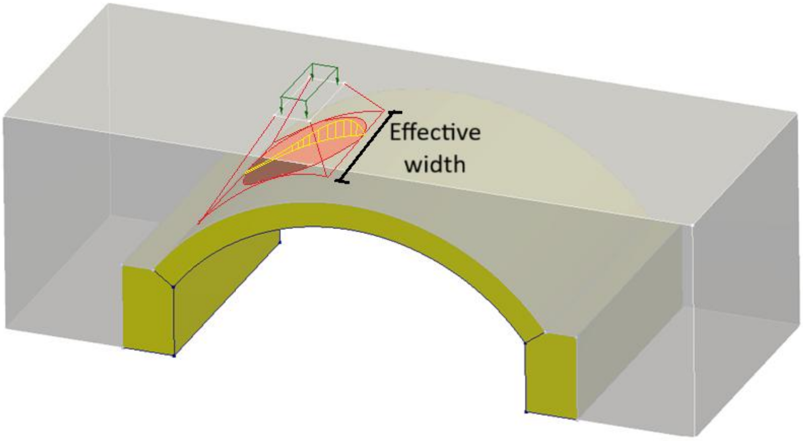

Figure 35. Definition of effective width and load spread in the third dimension

The first approximation used the equation provided in Section 2.3.5, based on the load applied at plate E. A value of β = 0,5 rad was used, as recommended for this type of backfill, and the depth (D) was taken as 515 mm as for the center load location and 680 mm for the side load. The depths used can be seen in Figure 36 and Figure 37.

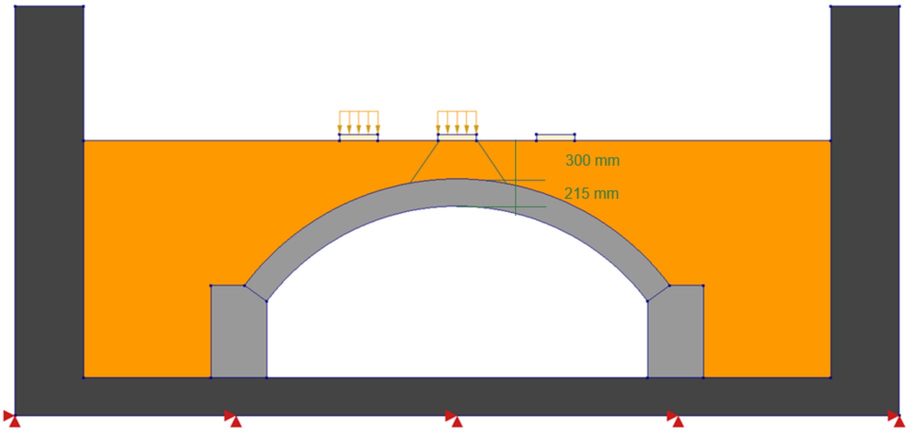

Figure 36. Initial approximation for load spread dimension used for center load

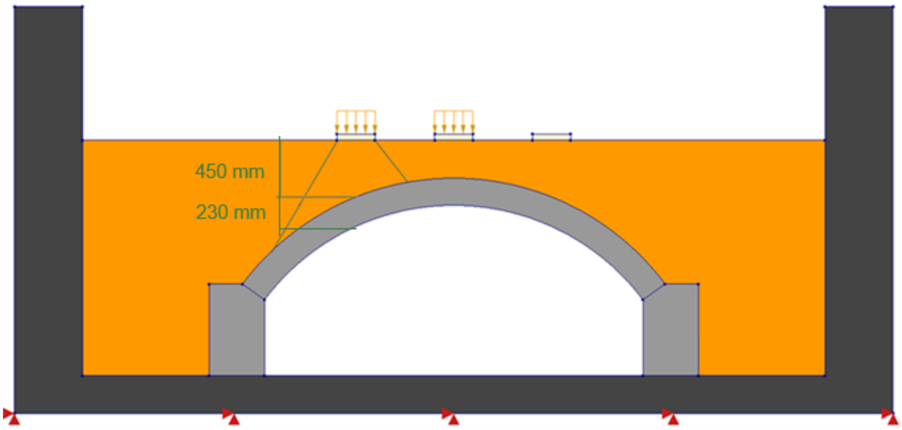

Figure 37. Initial approximation for load spread dimension used for side load

The comparison, as in section 4.1, the stiffnesses along the longitudinal centerline of the 3D model under the load were compared to those obtained in the 2D model. In the same way, a load of 150 kN was used to calculate the stiffnesses, and the analyzed points were at the crown (center) and the quarter-span, corresponding to plates E and B respectively (see Figure 22). The results showed that the effective width determined using the theory was not enough to represent the 3D model. (see Figure 38)

A sensitivity analysis was conducted by adjusting the applied load in the 2D model based on different assumed effective widths. The load was iteratively modified until the radial displacement from the 2D model closely matched that of the 3D model. The analysis determined a linear relationship when making the comparison between the equivalent width and the initial stiffness per point, which is expected since the model is linear. This comparison plays a key role in calibrating the effective width used in the 2D model.

For the comparison a normalization of the values was made for easier understanding.

$$Normalized\ value_{Center} = \frac{Stiffness_{2Dmodel,center}}{Stiffness_{3D\ model,center}}$$

$$Normalized\ value_{side} = \frac{Stiffness_{2D\ model,side}}{Stiffness_{3D\ model,side}}$$

Where the stiffness in the center is calculated using the radial displacement in the crown and the load in plate E and the stiffness in the side is calculated using the radial displacement at one quarter of the span and the load in plate B. These were implemented in Figure 38.

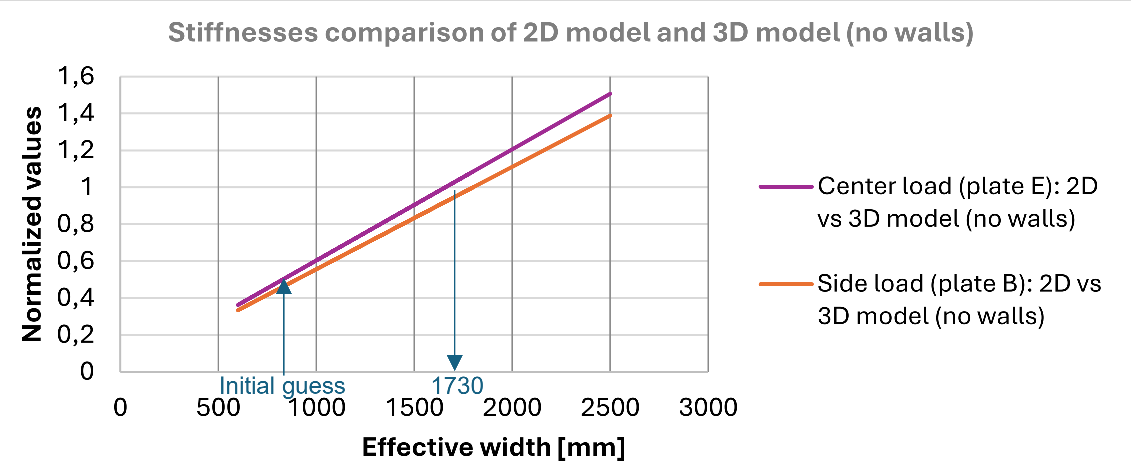

Figure 38. Effective width comparison vs 3D model and test results

When making this comparison a back calculation of the angle was made using the depths shown in Figure 36 and Figure 37. Table 12 shows the results obtained where the average between 1600 and 1800 is 1730 mm as indicated in Figure 38.

Table 12. Angles used and corresponding effective widths

Property	Initial guess	For normalized value of 1
Angle for center load (D=515 mm)	25,9	52,9
Effective width center load [mm]	800	1660
Angle for side load (D=680mm)	25,5	47,8
Effective width side load [mm]	950	1800

Because this is not the only way to identify the load spread, the 3D model was analyzed longitudinally and transversally to cross check the values obtained when analyzing the stiffnesses. For this, values were obtained from the interface between the arch and the soil.

The longitudinal and transversal direction were analyzed along the arch in the center line and transversal line below the location as shown in Figure 39. The results from the model can be seen in Figure 40, Figure 41, Figure 42 and Figure 43. And from these figures it can be observed that the behavior of the load spread is in the shape of a bell.

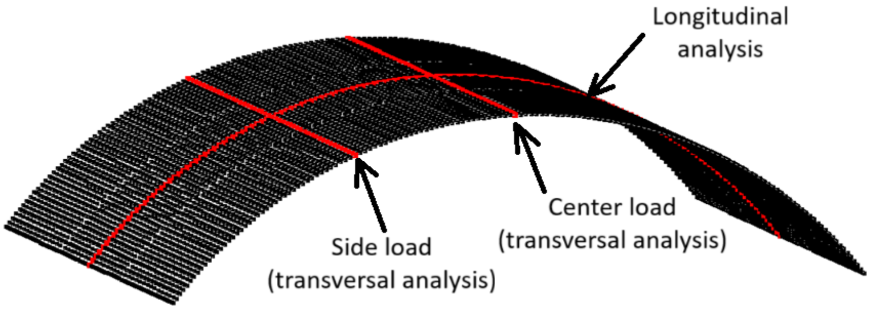

Figure 39. Location of nodes analyzed in the interface for the load spread

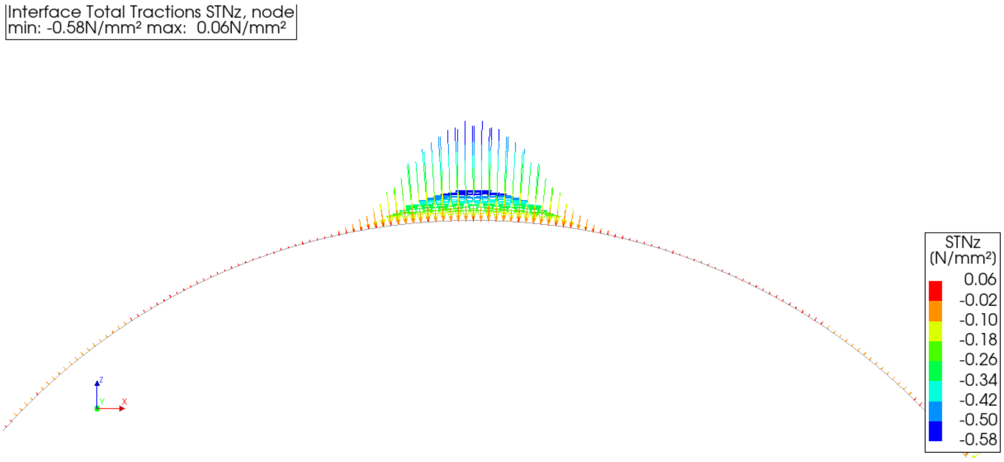

Figure 40. Interface tractions for the center load (longitudinal view)

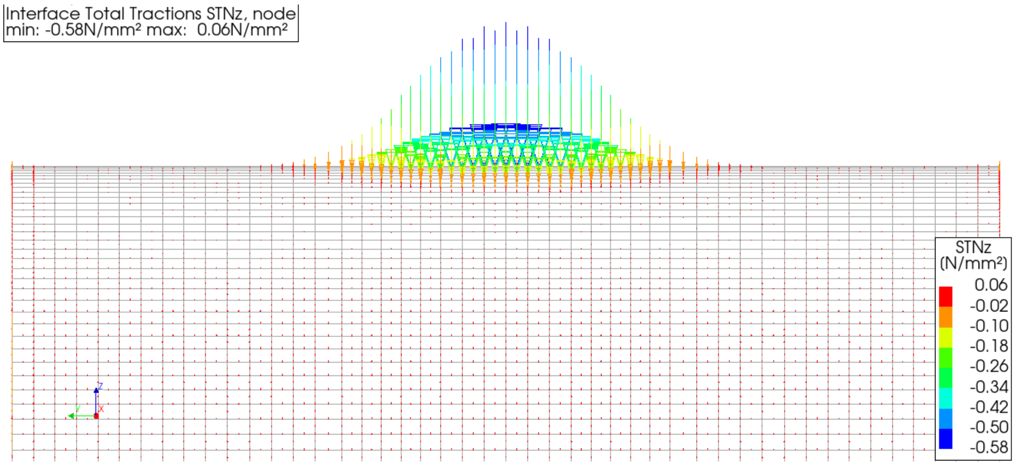

Figure 41. Interface tractions for the center load (transversal view)

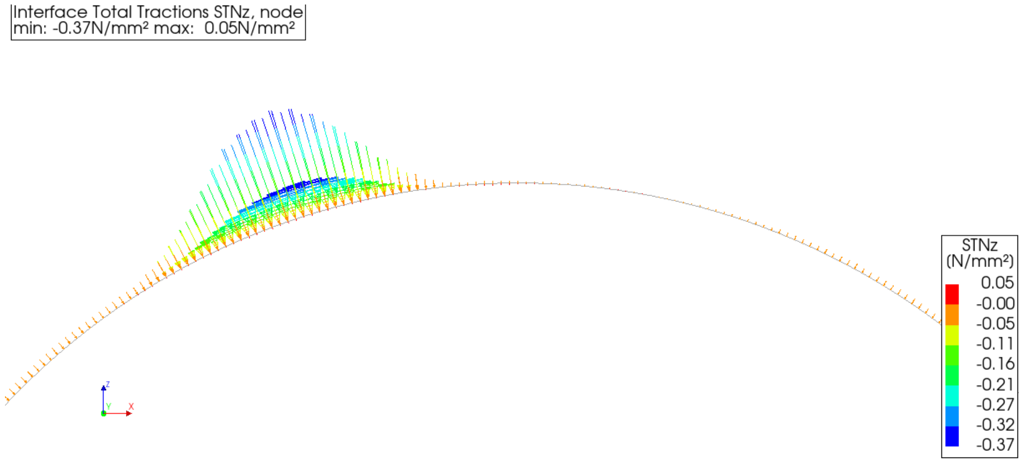

Figure 42. Interface tractions for the side load (longitudinal view)

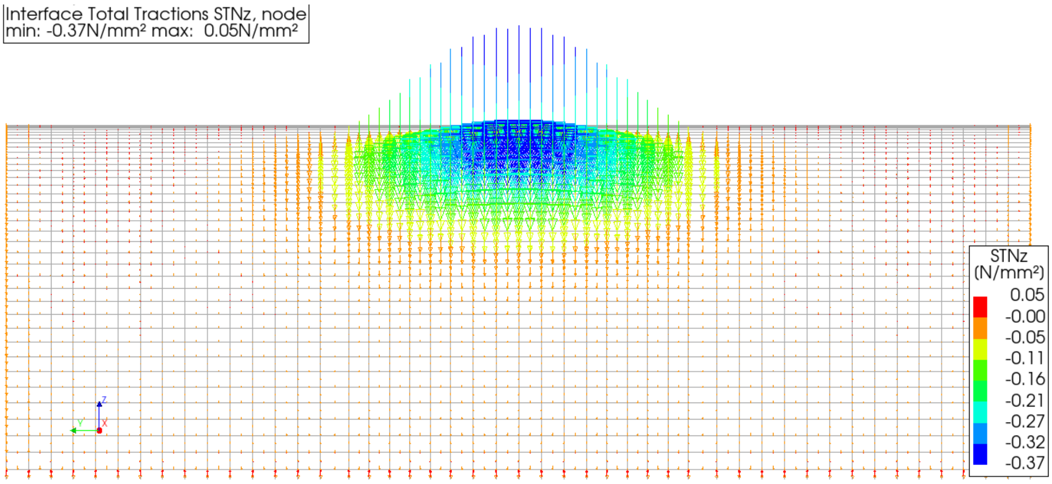

Figure 43. Interface tractions for the side load (transversal view)

For this analysis, the stresses were normalized using the maximum stress, and therefore the load spread can be visualized where the values are larger than zero. These results in Figure 44 and Figure 45 match the bell shape results obtained previously. The normalized tractions were calculated as follows where "i" refers to the position under the arch.

$$Normalized\ tractions = \frac{Tractions_{3D\ model,i}}{Tractions_{3D\ model,max}}$$

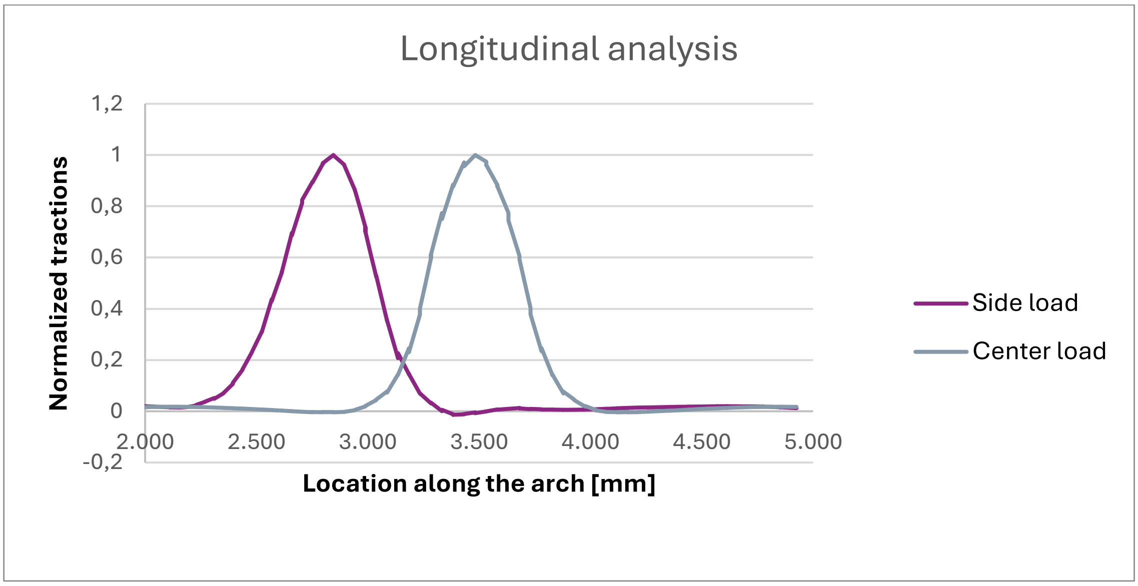

Figure 44. Longitudinal interface tractions for each location

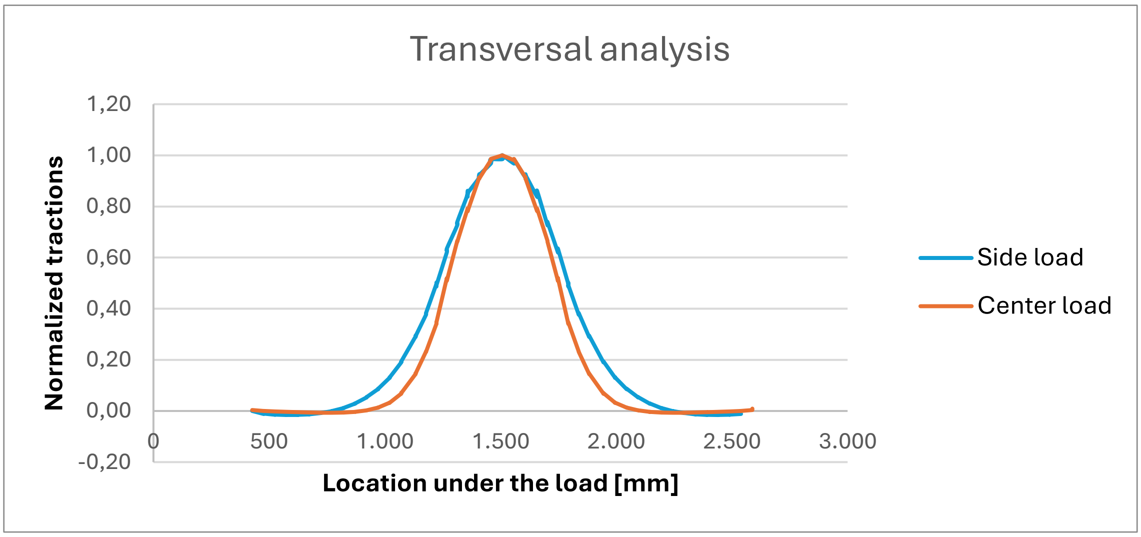

Figure 45. Transversal interface tractions for each location

The effective width calculated as in section 2.3.5 for the center and the side load using a 50° for β, using D as the thickness between the load plate and the top fiber of the masonry (300 mm and 450 mm respectively) and a B of 300 mm due to the plate distances, the effective width roughly matches what is observed in Figure 44 and Figure 45. In the center load the effective width determined with the equation is 1015 mm and for the side load 1373 mm.

For the longitudinal center load and for both of the transversal analysis location, the load spread is straight forward because the load is located in the center of the curve. But for the side load analysis in the longitudinal direction, it can be observed that at the left side of the curve it does reach zero, and therefore the load spread spreads further than the arch. In this case the analysis is made with one side only and the depth used to determine the angle is lower. The summary of the data can be seen in Table 13.

Table 13. Summary of findings from the load distribution graphs

Analysis	**Location of intersection 1 [mm]**	**Location of intersection 2 [mm]**	**Load spread width [mm]**	**Angle determined for interface [°][2]**	**Adding the arch width to the load spread [mm][3]**	**Angle determined from overall load spread [°]**
Longitudinal (center load)	4072	2941	1131	51,5	1561	50,8
Transversal (center load)	971	2045	1074	52,2	1504	49,5
Longitudinal (side load)[1]	3333	2708	625	56,9	1055	53,1
Transversal (side load)	771	2245	1474	52,5	1904	49,7

[1] The analysis is made using the side that the load converges with the arch.

[2] The depth used for the calculation of the longitudinal direction is determined by an average depth of the soil in the section of load spread

[3] The additional width spread is calculated assuming a load spread of 45° through the masonry and an additional depth of 215 mm.

From the values obtained it matches very closely the average obtained in the stiffness analysis. This means that using an angle of 50° would give a good approximation of the effective width, when using the depth of the soil + the masonry below the load. Although, due to the load spread angle, the other half of the load spread in the longitudinal (side load) will be overpassing the arch, leading to a full depth of the soil and therefore the effective width in this location is calculated to be the full width of the bridge.

It is evident that the load spread angle might vary when applying a nonlinear analysis, as load steps increase the displacement also increases caused by a load. The soil (limestone in this case) having lower mechanical properties than the masonry and the concrete, will redistribute the load leading to a change in the angle. Through the analysis, even cases of partial failure in the soil or structure can also influence and modify the load spread angle.

4.3 3D Non-linear Model with spandrel walls

To analyze the contribution of the constitutive model of the masonry and the interfaces to the model, the 3D model with walls was divided into 3 models. Using fewer elements, still maintaining the essence of the model, the description of each model are in Table 14.

Table 14. Model setups

Model	Backfill	Masonry arch and spandrels	Reinforced Concrete	Interfaces[1]	Connection between spandrel walls and concrete walls
Model A	Mohr-Coulomb plasticity	Linear elastic isotropic	Linear elastic isotropic	No interfaces	Disconnect to substitute the foam
Model B	Mohr-Coulomb plasticity	Total strain-based crack model	Linear elastic isotropic	No interfaces	Disconnect to substitute the foam
Model C	Mohr-Coulomb plasticity	Total strain-based crack model	Linear elastic isotropic	Coulomb friction	Disconnect to substitute the foam

[1] The interfaces include the interfaces between the soil and the masonry, the soil and the reinforced concrete wall, the masonry arch and spandrel walls, and the masonry and the reinforced concrete

These models were compared with the test results T22 (which is the load considered as the failure load). This can be observed in Figure 46.

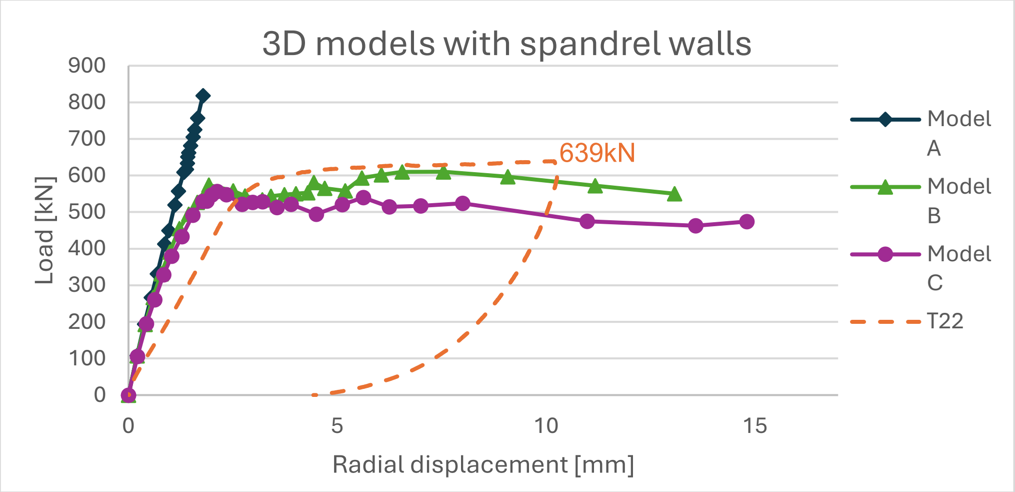

Figure 46. Load-radial displacement curve for the models with spandrel walls

When analyzing the results for the models with the load applied to plate B, the initial stiffness appears to be similar. However, as the load increases through the linear-elastic phase, the stiffness of the model is higher than that observed in the test results. This difference is reasonable, as the model is loaded only once, whereas the test has had multiple loading cycles, both statically and cyclically. The test involves a series of loadings prior to reaching the "high load" or even the "failure load" on plate B. Therefore, some cracking has already occurred due to previous loading, leading to a reduction in both stiffness and capacity. As indicated in the test description, the loads were applied at various locations, and even though the load is intended to remain within the elastic range, the bridge experiences a decrease in stiffness within this range as well. And so, the behavior observed in test T22 is consistent with expectations.

In Model A, having the soil is contained in a linear-elastic structure can’t determine a peak load because the bridge doesn’t reach failure. Because of this the overall behavior is linear elastic as seen in Figure 46. When comparing model B with the test, the behavior of the bridge is governed by the tensile behavior of the masonry explaining the peak and then some slight failure, still maintaining the overall behavior as a plateau. Although the behavior after 2mm radial displacement is not as pronounced as in model C, it can still be perceived in model B. The peak load for both models almost reaches the one determined in the test. However, a higher peak load was obtained when the model didn’t yet have the interface properties, which is explained by having lower properties in the interfaces providing less support to the structure in these locations and leading to redistribution of stresses. In Table 15, the errors from the peak loads are presented, where 13 % and 4,5 % of an error is significantly low.

Due to the shear retention value, the post-peak behavior is affected by having some shear when the diagonal cracking is happening in the spandrel walls, which allows the structure to have a better ductility. Therefore, the post peak behavior for models B and C are considered more reliable due to errors being low. An additional analysis was made by running models B, C, E and F with a shear retention of zero, to evaluate the significance of this parameter in the post peak response of the model and its effect in ductility. These results and discussion are presented in the Appendix 7.1 and provide evidence of the importance of this value.

Table 15. Peak load errors for models B and C

Model	Peak load	Error[1]
Model B	610,3	4,5%
Model C	556,2	13%

[1] Errors were calculated using the failure load as the real load.

For the cracking analysis, model A can’t be compared because of the masonry not being able to produce any cracking due to its linear-elastic model. Models B and C do contain cracking, and these are compared with the ones determined in the test. As reported in the paper by Sarhosis et al. (2024), no new cracks were observed when the load of 150 kN was on the B plate (Test T8). The way of identifying cracks means that most likely the cracks were around 0,1 mm when they were reported. This is the prompt that is used to consider the cracking representative. In Figure 49, even though cracks are detected by the model, they are still very small to be considered visible cracks. This means the results match the initial results from the tests in the arch. Also, it is observed in this figure that the cracking starts underneath the load and between the arch and the spandrel wall. In Figure 48 and Figure 49, the cracking identified in at the connection between the arch and the abutments, is a sign of hinges starting to form. The captured cracking figures are located in Figure 47.

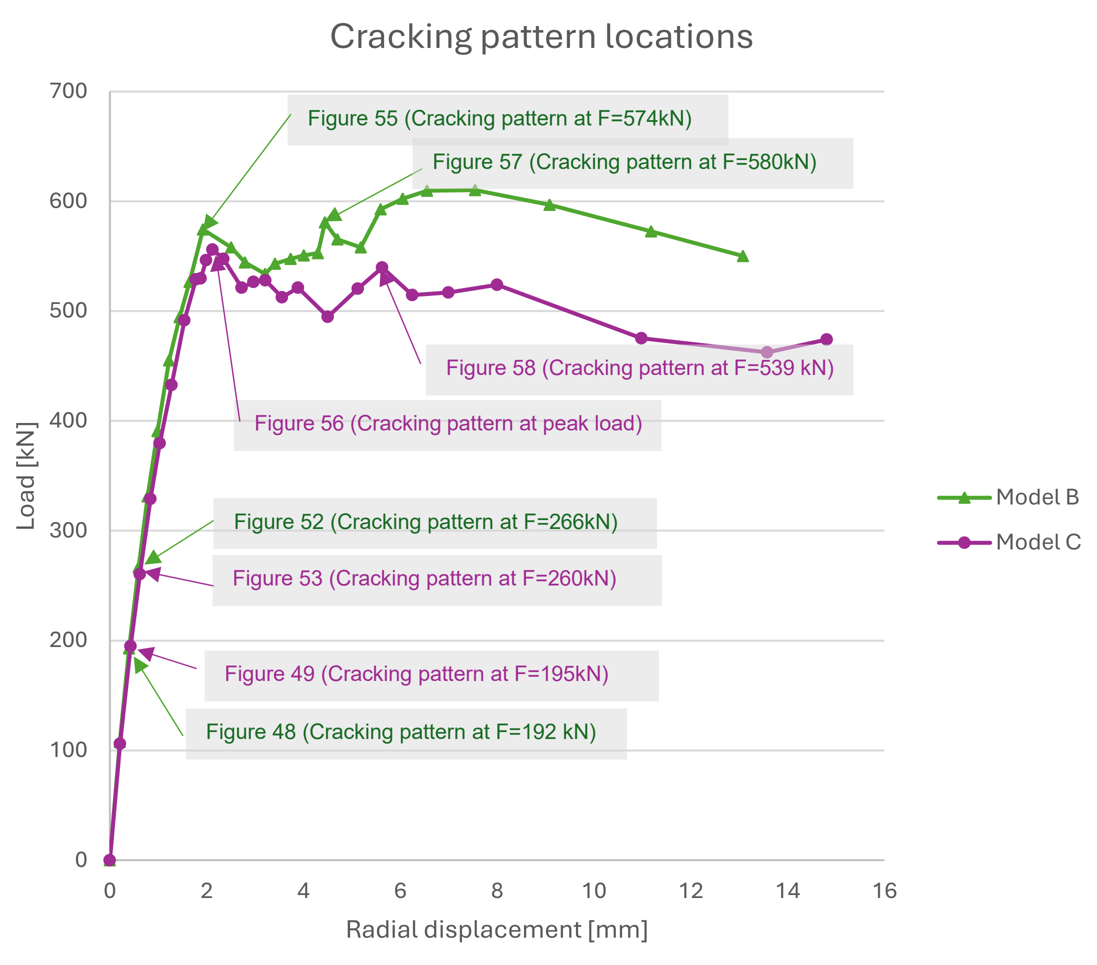

Figure 47. Cracking pattern locations

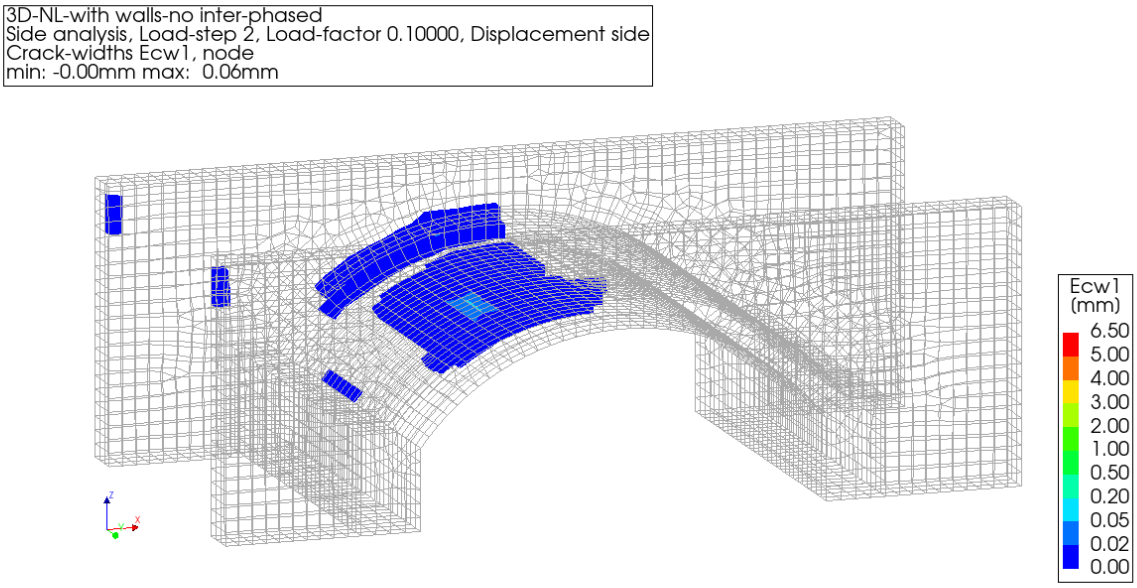

Figure 48. Cracking pattern for a 192 kN load for the model with spandrel walls for model B

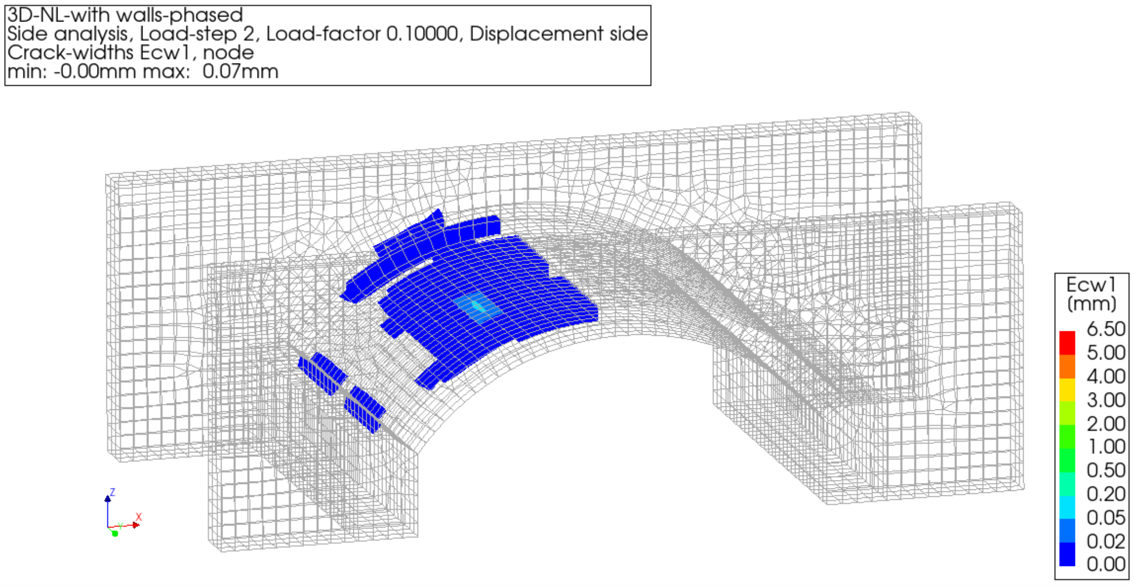

Figure 49. Cracking pattern for a 195 kN load for the model with spandrel walls for model C

The observed cracks were reported later when the load was applied in other plates. In Figure 50 the cracking for the 150kN is shown, which is a crack that happens between the spandrel walls and the arch. This is reported as the initial crack for the test. In models B and C also, an initial formation is also seen in the inner part of the spandrel walls, specifically in the connection with the arch, and it's expected to continue forming in this area similar to the behavior of the test.

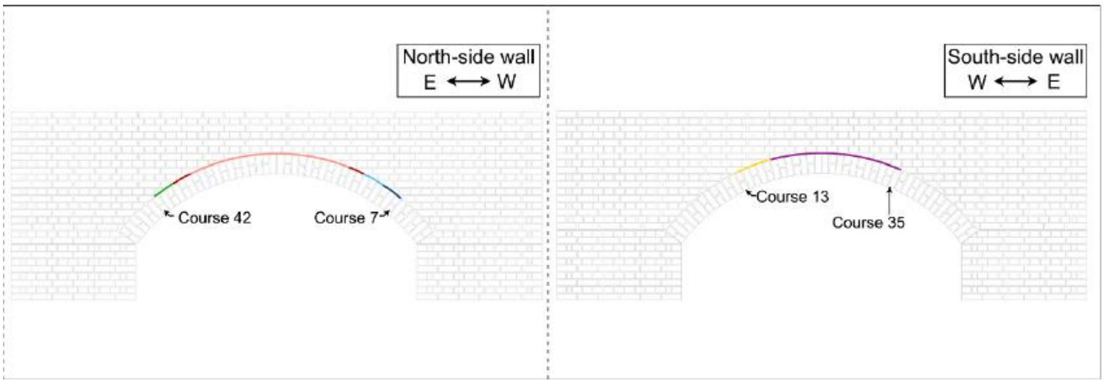

Figure 50. Cracking for the low load (150 kN) according to the test results (Sarhosis et al., 2024)

As expected, the cracking continues to develop as the changing in the loading. The cracking produced by the load applied at quarters of the bridge with the mid-load (250kN) is observed in Figure 51. The hinges start to form, some transversal cracks in the arch are already formed, and the cracks in the spandrel walls are starting to form.

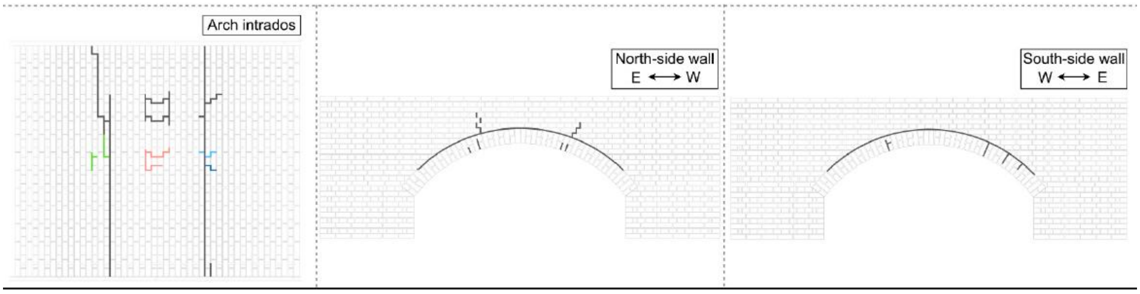

Figure 51. Cracking pattern due to 250kN located at quarters of the span (Sarhosis et al., 2024)

When comparing these cracks with the results obtained for the models B and C in Figure 52 and Figure 53, only visible cracking is the one just below the load, which is close to the results obtained in the cracking of the arch. On the other hand, the model hasn't yet presented any sign of cracking in the spandrel walls or as a start of a 3rd hinge for model C. Whereas model B, does have a sign of 3rd hinge and its presenting an opening due to the disconnected surface which was placed instead of the foam slabs, but this can be explained by the slightly higher load present in that step for model B than the one presented in model C.

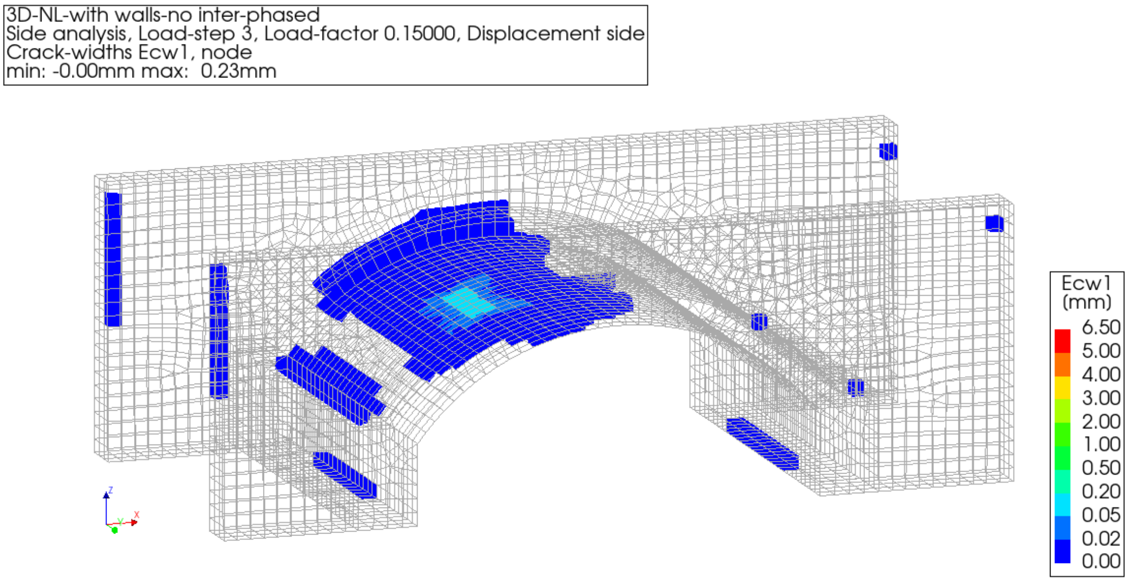

Figure 52. Cracking pattern for 266 kN for model B (view from the bottom of the arch)

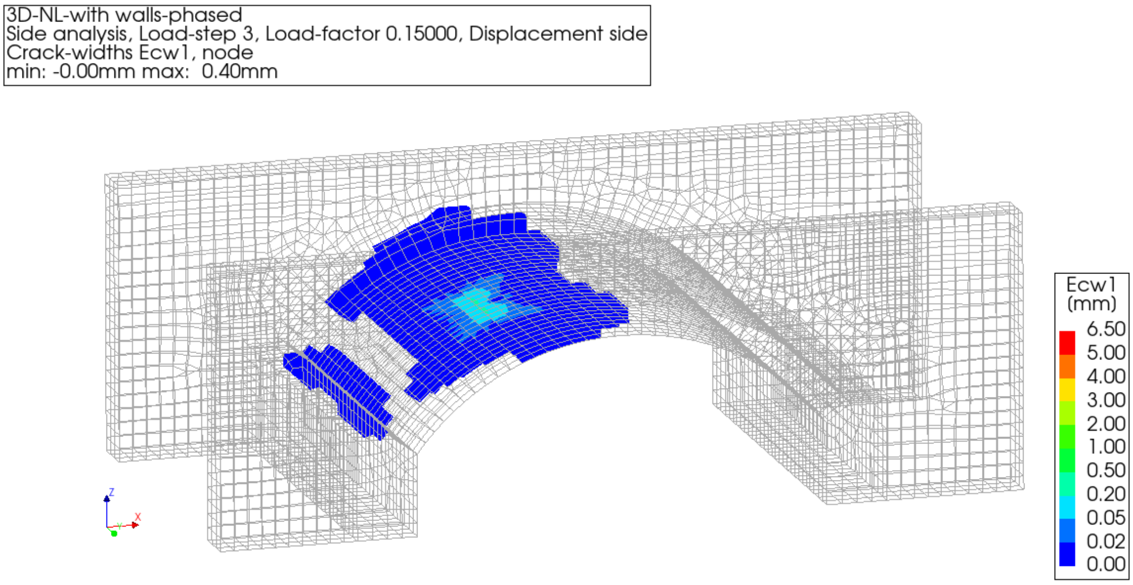

Figure 53. Cracking pattern for 260 kN for model C (view from the bottom of the arch)

As for the peak load, the models with walls match not only in the intrados of the arch but also the cracking in the spandrel walls. In the arch, the cracking crosses the full width of the bridge but also has extra cracks in diagonal directions. In the spandrel walls, two main diagonal cracks are formed, matching the behavior of the cracking in the benchmark. This can be seen when comparing Figure 54 against Figure 55 and Figure 56.

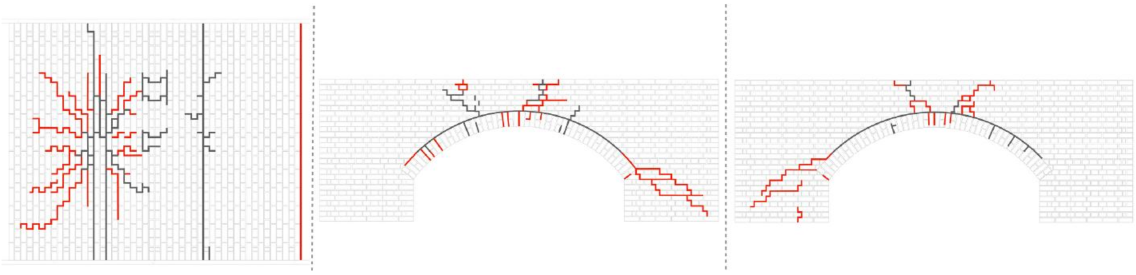

Figure 54. Cracking pattern for the failure load for the benchmark

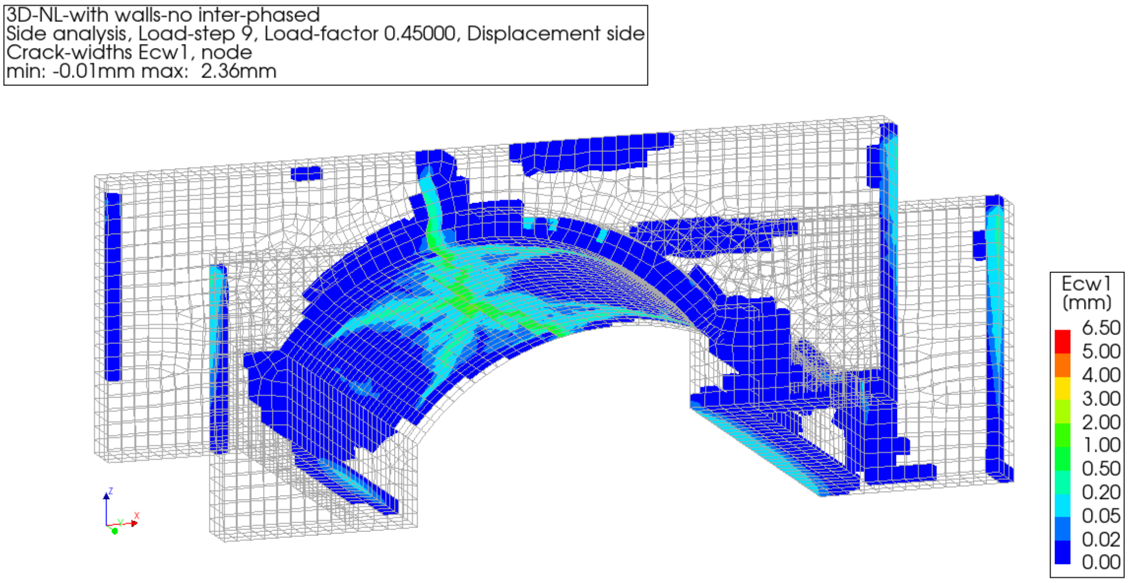

Figure 55. Cracking pattern for the first peak load for model B(view from the bottom of the arch)

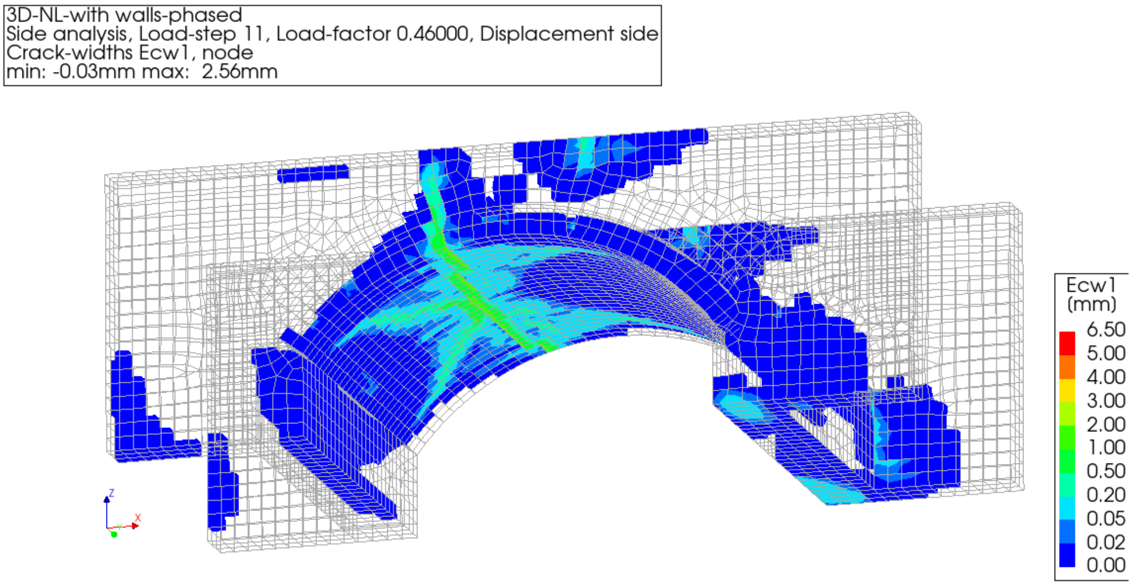

Figure 56. Cracking pattern for the peak load for model C (view from the bottom of the arch)

The cracking pattern is extended specially in the spandrel walls in the post peak behavior, but still following the same pattern, as the previous cracking patterns. This is observed in Figure 57 and Figure 58.

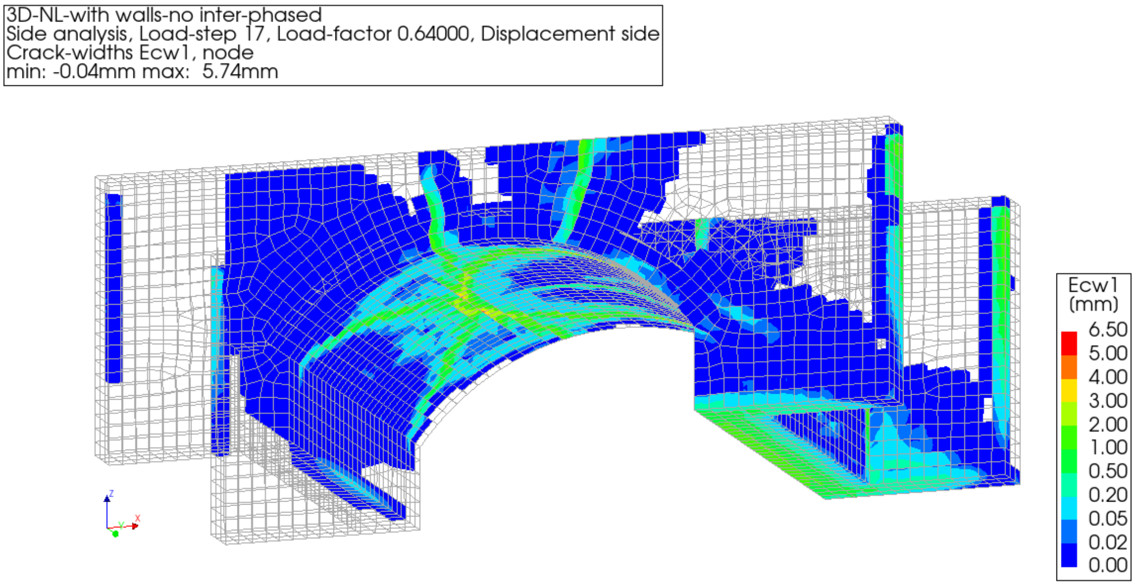

Figure 57. Cracking pattern for the post-peak for model B (view from the bottom of the arch)

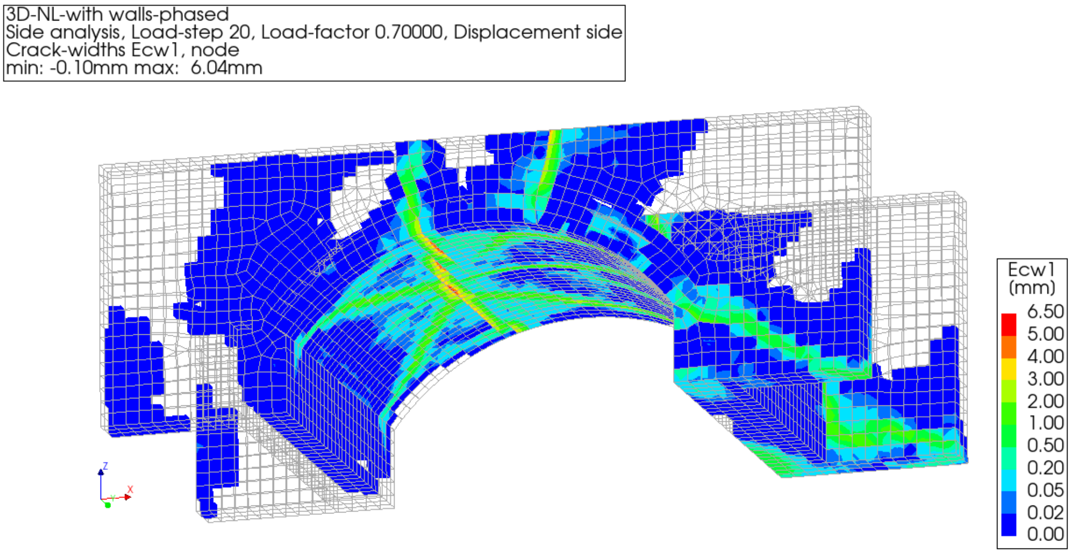

Figure 58. Cracking pattern for the post-peak for model C (view from the bottom of the arch)

For this comparison an analysis of the relative displacements along the arch is presented in Figure 59. It is observed that already for 106 kN, the model has some slipping between the arch and the spandrel wall, which is due to the interface properties which try to simulate the behavior of the test. This slipping behavior is not observed in the cracking due to it not opening but still producing a crack. This slipping behavior is mainly in the inner part of the connection, although in the figure, it can be observed that the slipping is produced through all the interfaces. An increase in relative displacements along this surface is observed as the load increases. On Figure 60 a separation between the arch and the spandrel walls is observed which matches the cracking explained previously.

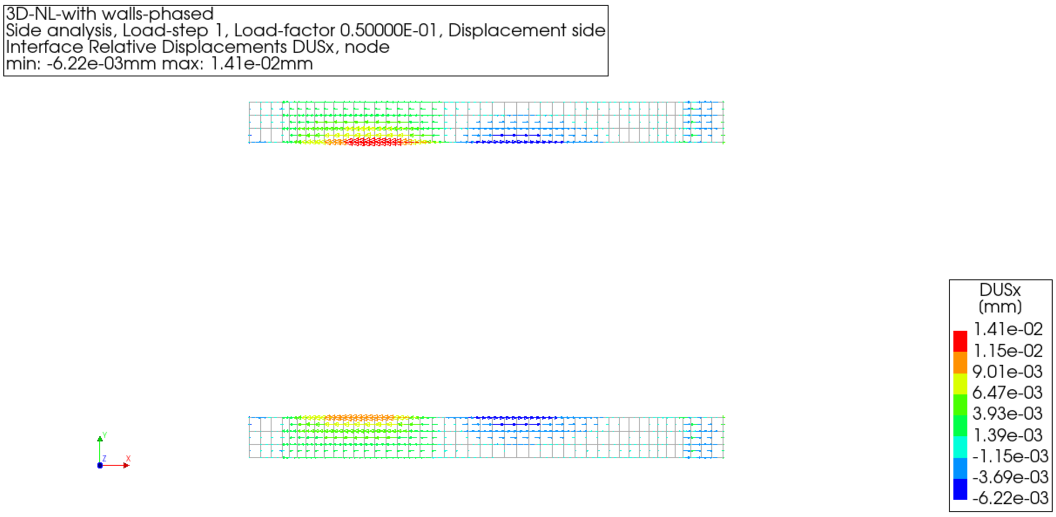

Figure 59. Interface relative displacements along the arch in model C for 106kN

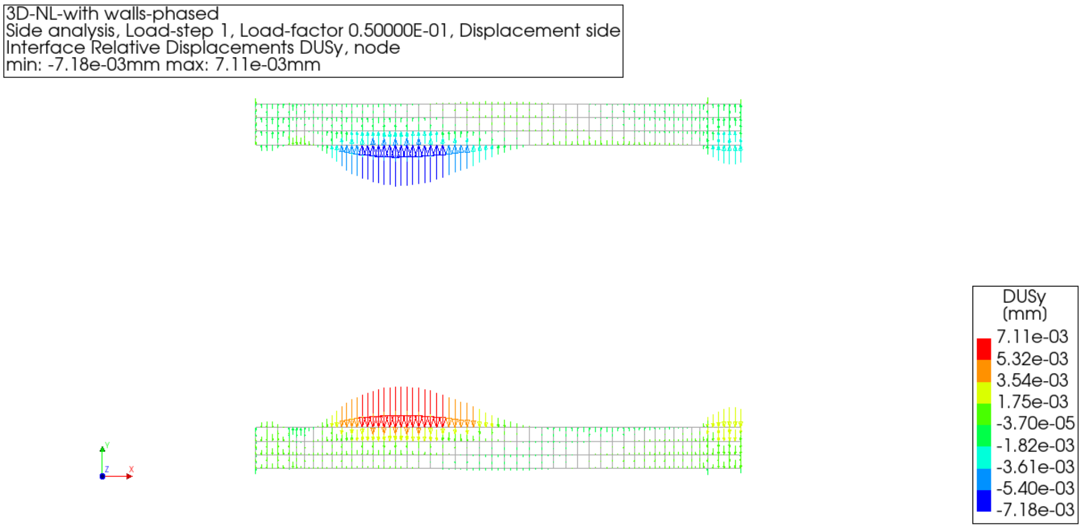

Figure 60. Interface relative displacements perpendicular to the arch in model C for 106kN

As for the ductility, this post peak behavior is affected by the shear retention behavior, and it's observed that the models have a sustained ductility. The model has ductility, not as flat of a curve as the one obtained in the test but still manages to hold some ductility following a similar behavior. The models show their capacity to resist some load after the peak having model B closely matching the experimental curve, and model C also, but not as good as model B. This can be observed in the radial displacement underneath the load application in Figure 46.

The behavior of the spandrel walls can also be observed from the results available for the test in Figure 61, where (a) is for the low-load, (b) is for the mid-load results and (c) is for a mid-load but for the opposite location. These results are compared with model C's out-of-plane displacements seen in Figure 62 and Figure 63. The behavior for a 195 kN load should be somewhere in between the values recorded for the test. The model contains displacements in the same order of magnitude as the test displacements. The behavior is consistent for the part of the wall that is far from the load application. But the displacements obtained for the wall close to the load application are in the opposite direction, even though they have similar order of magnitude. As for the behavior of the test when the load was in the H plate (also three-quarters of a span on the opposite side), the behavior of the walls is as expected and does match the behavior of the model, although the magnitude is slightly bigger in the test than in the model. For this case, the model starts matching the values seen in Figure 61(c) in the out-of-plane direction when load reaches 460 kN.

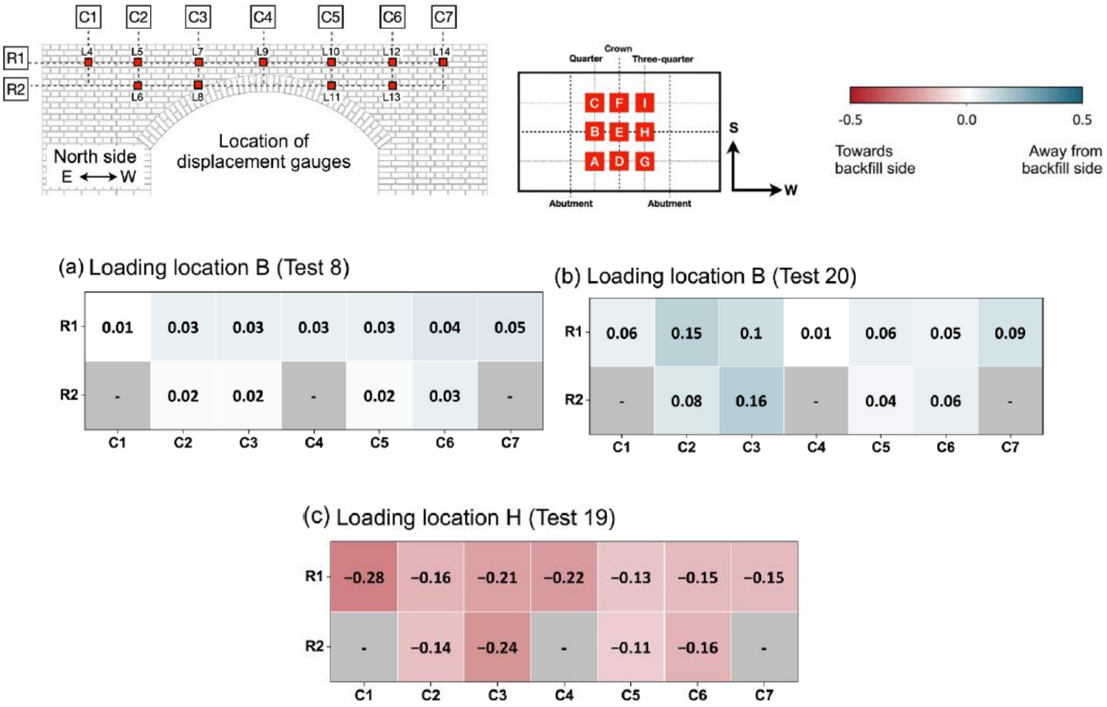

(a) Loading location B (Test 8)

	C1	C2	C3	C4	C5	C6	C7
R1	0.01	0.03	0.03	0.03	0.03	0.04	0.05
R2	-	0.02	0.02	-	0.02	0.03	-

(b) Loading location B (Test 20)

	C1	C2	C3	C4	C5	C6	C7
R1	0.06	0.15	0.1	0.01	0.06	0.05	0.09
R2	-	0.08	0.16	-	0.04	0.06	-

(c) Loading location H (Test 19)

	C1	C2	C3	C4	C5	C6	C7
R1	−0.28	−0.16	−0.21	−0.22	−0.13	−0.15	−0.15
R2	-	−0.14	−0.24	-	−0.11	−0.16	-

Figure 61. Test results for the out-of-plane (Sarhosis et al., 2024)

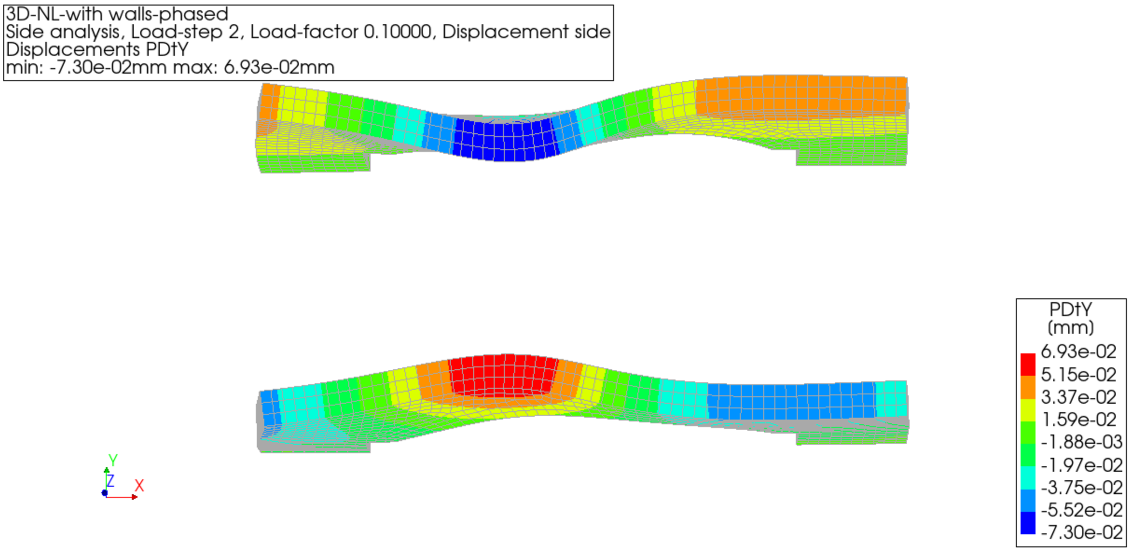

Figure 62. Out-of-plane deformation of the spandrel walls top view for model C at 195 kN

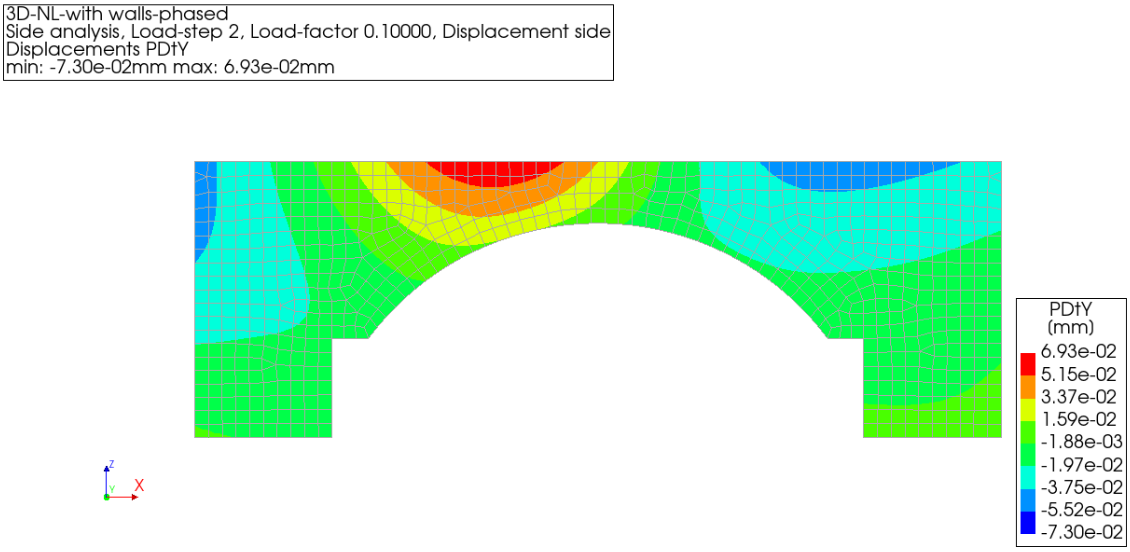

Figure 63. Out-of-plane deformation of the spandrel walls side view for model C at 195 kN

4.4 3D Non-linear model without spandrel walls

The same division was done as the one seen in section 4.3, the difference relies on the removal of the spandrel walls, where one of the models has only the backfill nonlinear, the second model has masonry and backfill nonlinear and the third model has masonry and backfill nonlinear and interfaces. The 3 models were made as described in Table 16.

Table 16. Model setups

Model	Backfill	Masonry arch	Reinforced Concrete	Interfaces[1]
Model D	Mohr-Coulomb plasticity	Linear elastic isotropic	Linear elastic isotropic	No interfaces
Model E	Mohr-Coulomb plasticity	Total strain-based crack model	Linear elastic isotropic	No interfaces
Model F	Mohr-Coulomb plasticity	Total strain-based crack model	Linear elastic isotropic	Coulomb friction

[1] The interfaces include the interfaces between the soil and the masonry, the soil and the reinforced concrete wall, and the masonry and the reinforced concrete.

In a similar way the models without the walls are compared to the ones with the spandrel walls to evaluate the effect of the walls and to make sure that the initial effect is still the same when considering nonlinearity. The models' results are shown in Figure 64 and the convergence plots of the models are shown in Appendix 7.2, and they show that all the points converged.

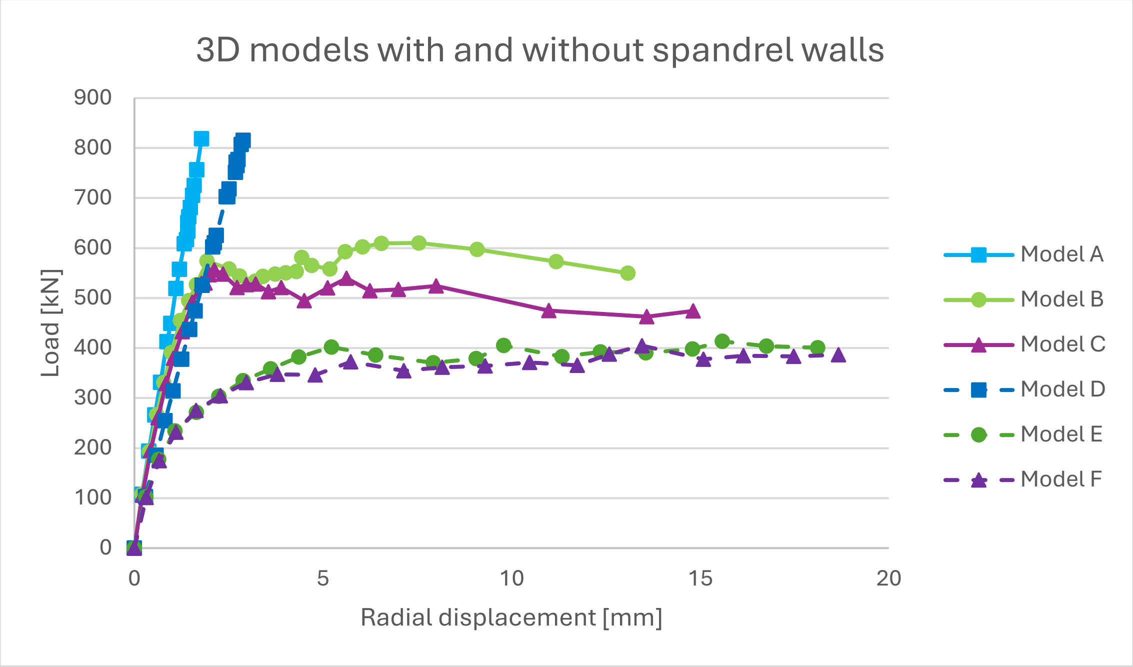

Figure 64. Load-radial displacement curve for the models with and without spandrel walls

When comparing model A to model D, a lower stiffness is detected for the model without spandrel walls, which matches the previous conclusion made when the models were linear elastic where the model without spandrel walls has a lower stiffness than the one with walls. Due to the changes in the soil constitutive model in the non-linear model, the initial stiffness is lower. The model with only soil as a non-linear material can't represent a peak load because the masonry is still a linear-elastic material, and therefore, they have no failure.

The same behavior is observed when looking at the initial stiffnesses of the models with walls against the models without walls. Not having the spandrel walls gives less support to the arch and consequently the peak load and the initial stiffness are lower as observed in the models B, C, E and F. In Table 17, the effect of the spandrel walls due to a peak load comparison is made, the results show that the peak load is underestimated by around 52% when there are no interfaces included. When the interfaces are included and contributing to the model as the comparison between model C and F, the load difference is significant, which means that the spandrel walls have a large contribution and not including them would mean 49% of the capacity is lost.

Table 17. Effect of spandrel walls on nonlinear models according to peak loads

Model	Condition	Peak load [kN]	Effect of spandrel walls
Model B	With walls (no interfaces)	610,3	52%
Model E	Without walls (no interfaces)	401,8	
Model C	With walls (with interfaces)	556,2	49%
Model F	Without walls (with interfaces)	372,3	

The effect of spandrel walls was calculated using the following equation.

$$Effect\ of\ spandrel\ walls = \frac{Peak\ load_{with\ walls} - Peak\ load_{without\ walls}}{Peak\ load_{without\ walls}}$$

An additional check was made comparing a secant at 70% of the peak load, this is only possible with the models that have a peak load (models B, C, E and F). A lower stiffness is determined by the models; this is expected since the materials are behaving nonlinearly. As for models B and C, with spandrel walls, the stiffness drops around 28% whereas the models E and F the drop is higher reaching 40% to 55%. The reason for a higher drop for the models is due to the lack of spandrel walls, which in models B and C, the walls are providing stiffness to the whole system. The initial stiffness is reduced from 30% to 36% when spandrel walls are removed. The stiffness differences can be seen in Table 18.

For the Test T22 where the benchmark reaches 70% of the peak load, the stiffness drops by almost 70%, but the behavior of the curve from 100kN up to this point seems to have quite a linear behavior. As the lower stiffness is expected due to the several loads applied on the benchmark before reaching the failure-load test.

Table 18. Summary of stiffnesses

Model	Initial stiffness [kN/mm]	Stiffness of secant at 70% of the peak load [kN/mm]
Benchmark (Test T22)	674	212
Linear elastic model with walls	613	-
Model A	536	-
Model B	531	385
Model C	499	353
Linear elastic model without walls	429	-
Model D	344	-
Model E	337	150
Model F	321	190

Regarding cracking patterns in the models, the cracks for the models without walls start at the bottom of the arch and propagating transversally without a significant increase in the load. This behavior is product of the missing spandrel walls that prevent the cracks from propagating further in the arch transversally. This is observed in Figure 65, where the cracking is represented for the similar loading as in Figure 53. In model F it is easier to identify the forming hinges. The cracking starts earlier than in the models with walls. Different from the model C, the cracking at a lower load is already considered visible.

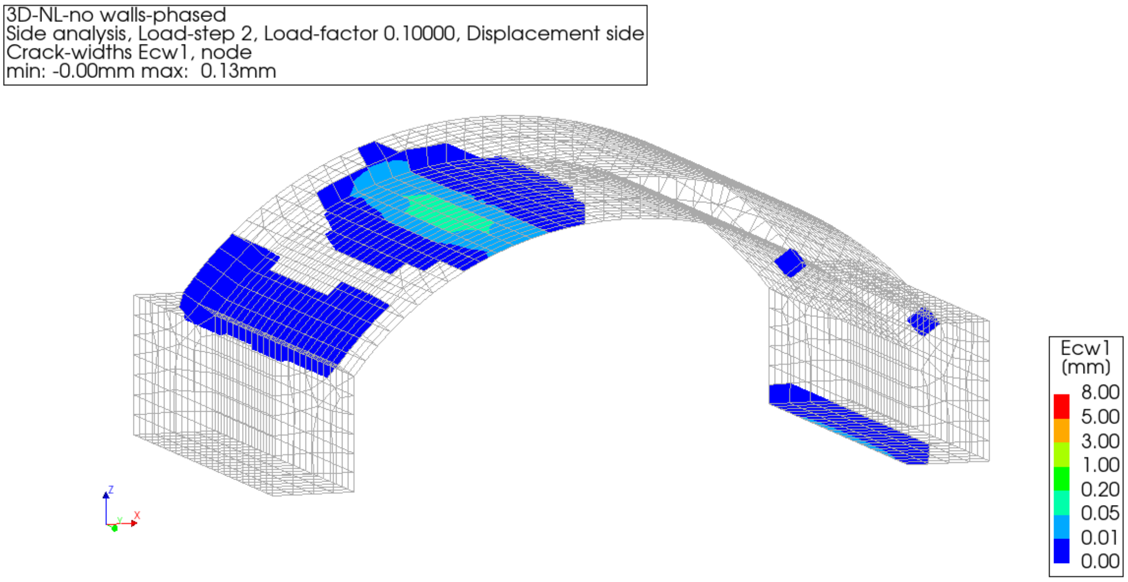

Figure 65. Cracking pattern for model F at 175 kN (view from the bottom of the arch)

When it comes to comparing ductility, the model with spandrels exhibits a more ductile response than the one without spandrels (see Figure 64). This is because the arch is working separately with less confinement which allows the formation of hinges in critical locations. Whereas in models B and C, the stiffness of the arch is higher, limiting the cracks from propagating transversally in the arch, preventing the formation of the hinges closer to the spandrel walls.

For model B, the model presents a slight increase in the load after a radial displacement of 2 mm creating a curve similar to a bilinear curve in which the model seems to have a sort of a plateau making the curve similar to the benchmark’s response. Model C does not provide a higher peak as model B, but it does maintain the curves figure, also having radial displacements while maintaining the load. All models, with and without spandrel walls have high ductility and are comparable to the test results. Although the results show that a more complex behavior of the curve is detected when spandrel walls are included. And a lower load step size around what seems to be the peak load is needed to better understand what is happening in the system.

4.5 2D Non-linear Model comparison

The non-linear model was performed using the non-linear properties that were described above in section 3.4.2. This 2D model was compared with the 3D model without spandrel walls, to determine how representative it can be.

When comparing the behavior of the initial stiffness, both models match. The ductile behavior is maintained. The peak load depends on the effective width used to calculate the loading, since the model is modelled using a one-meter width. Figure 66 shows the results according to different effective widths.

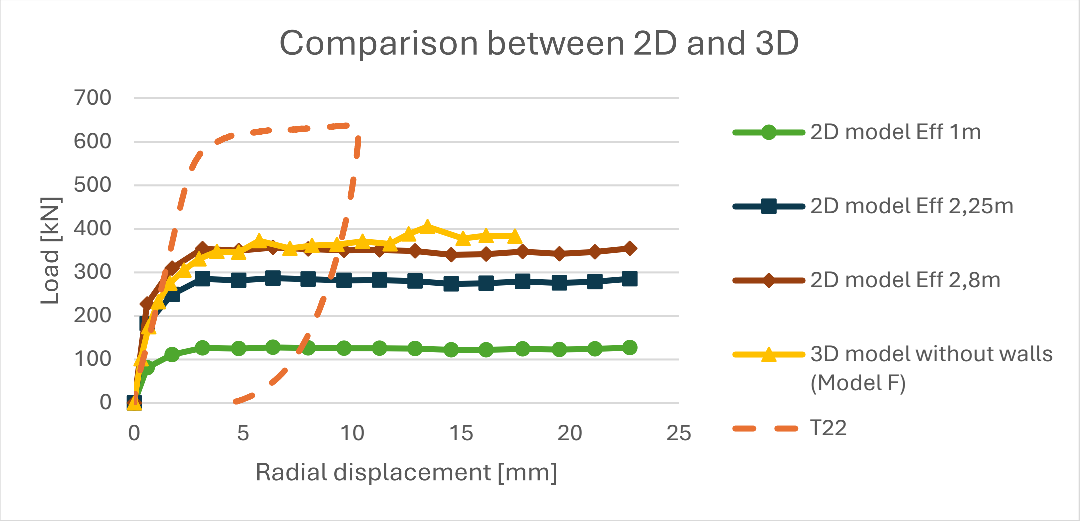

Figure 66. Results from 2D and 3D models with non-linear properties

If the 2D was needed to match the 3D model, then the effective width should be 2,8 m because 2,25 m (adjusted value for a plate of 750x300 mm from the 1,73 m previously calculated) is not enough. This 2,25 m is calculated using the equation in section 2.3.5 where D is 680 mm (distance to the lower fiber of the masonry), the load spread angle β is 50° and B is 750 mm (distance of the footing to determine the effective width). Although the behavior of the curve in Figure 66, does have similarities, the 2D model seems to have a sustained load compared to model F. If the effective width was 2,25 m, then the load is underestimated by 29% when compared to Model F, and it underestimated by 55% when comparing it to the benchmark considering that the test does have the spandrel wall contribution. Therefore, using a 2D approach with the load spread calculation according to the linear-elastic analysis is not as reliable as the 3D model for assessing this type of structure.

When comparing the behavior of the cracking is similar in a way that the hinges form in the same locations as in the 3D model it can be seen in Figure 67, Figure 68, Figure 69, Figure 70 and Figure 71. The sequence of the cracking is located in the same places when analyzing the center cross section of the 3D model without walls and the 2D. The sequence starts with a slight bigger crack just under the load application and another crack in the connection between the abutment and the arch as seen in Figure 67 and Figure 68. Later, as the load increases, another crack is formed in the arch as a hint of a third hinge, this sequence is consistent in both models but it easier to observe in the 2D model (see Figure 69 and Figure 70). As for the peak loading, for both models, the locations of the wider cracks are consistent, the only difference is the cracking in the 3D model has more smaller cracks along the arch, both models are observed in Figure 71 and Figure 72. In the 2D model the cracking is only represented in the transversal way and the energy is not being able to spread longitudinally, which would more pronounced cracking in the 2D model for the peak load.

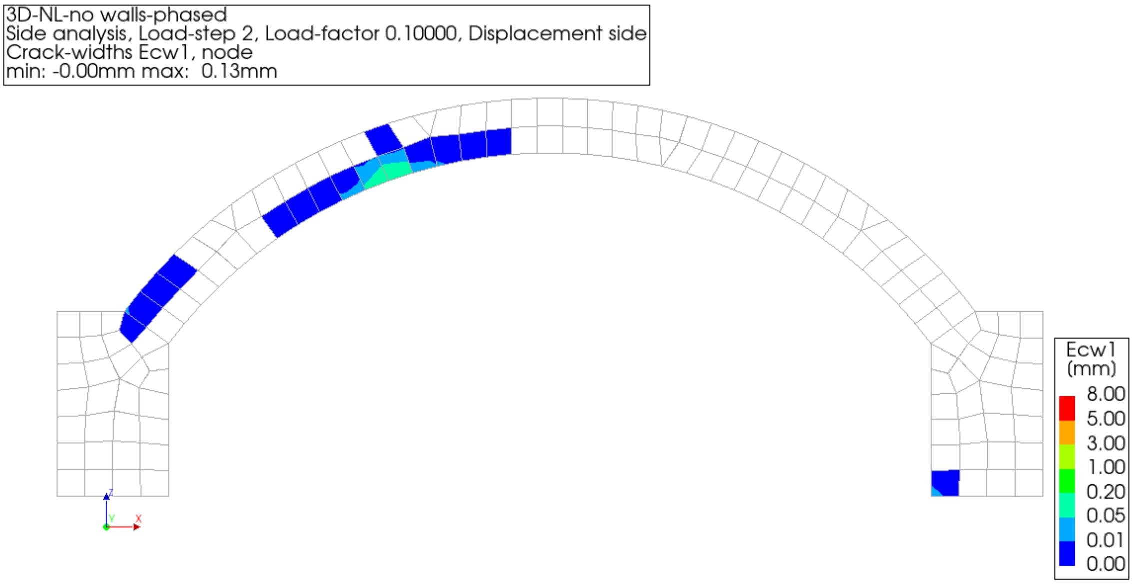

Figure 67. Cracking pattern for the 3D model initial cracks

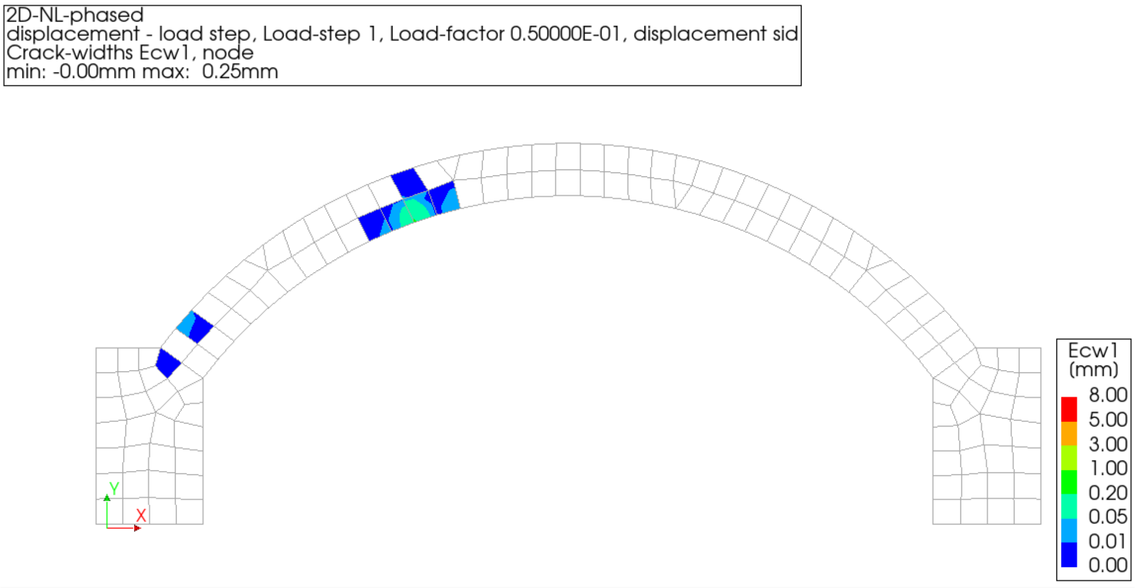

Figure 68. Cracking pattern for the 2D model initial cracks

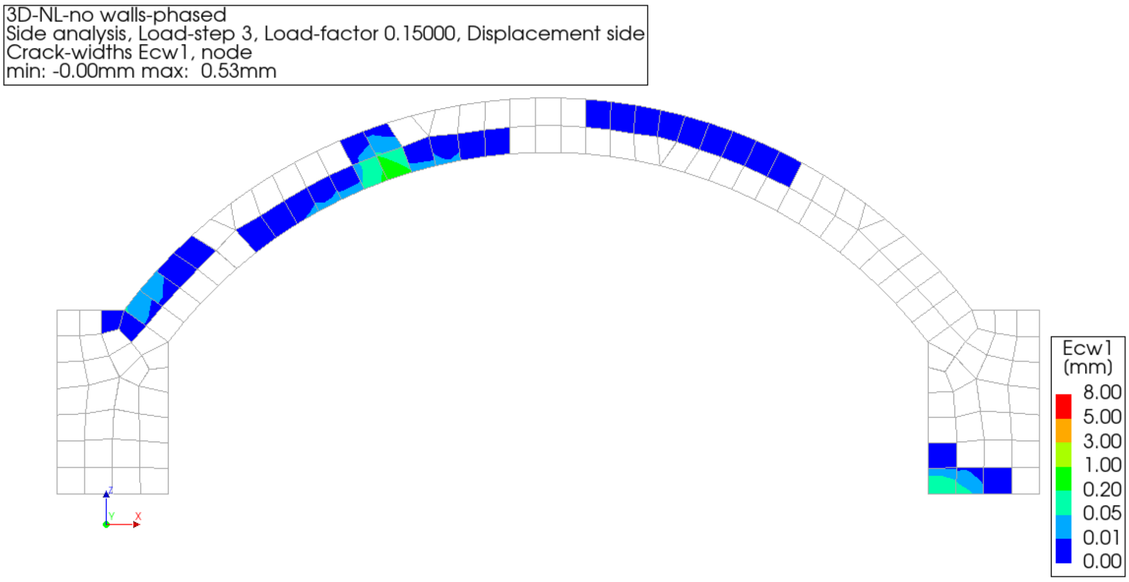

Figure 69. Following cracking pattern for the 3D model

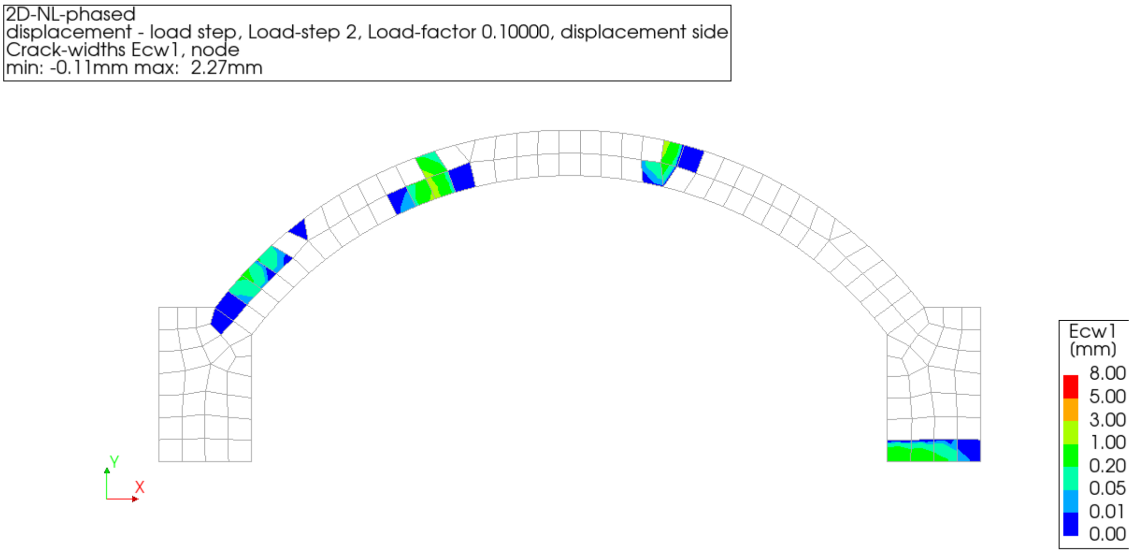

Figure 70. Following cracking pattern for the 2D model

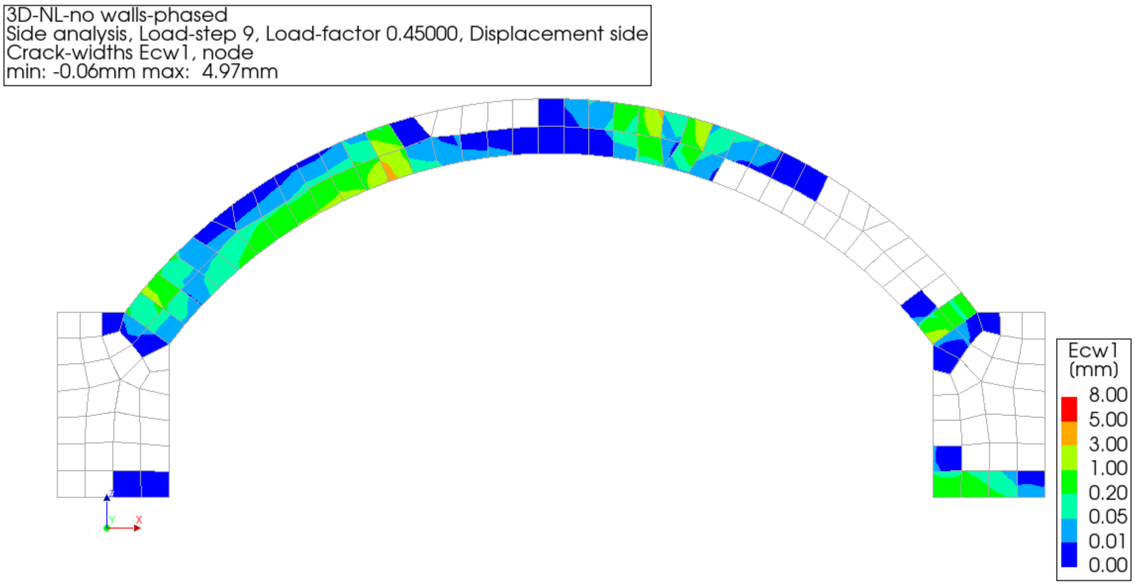

Figure 71. Cracking pattern for the 3D model first peak load

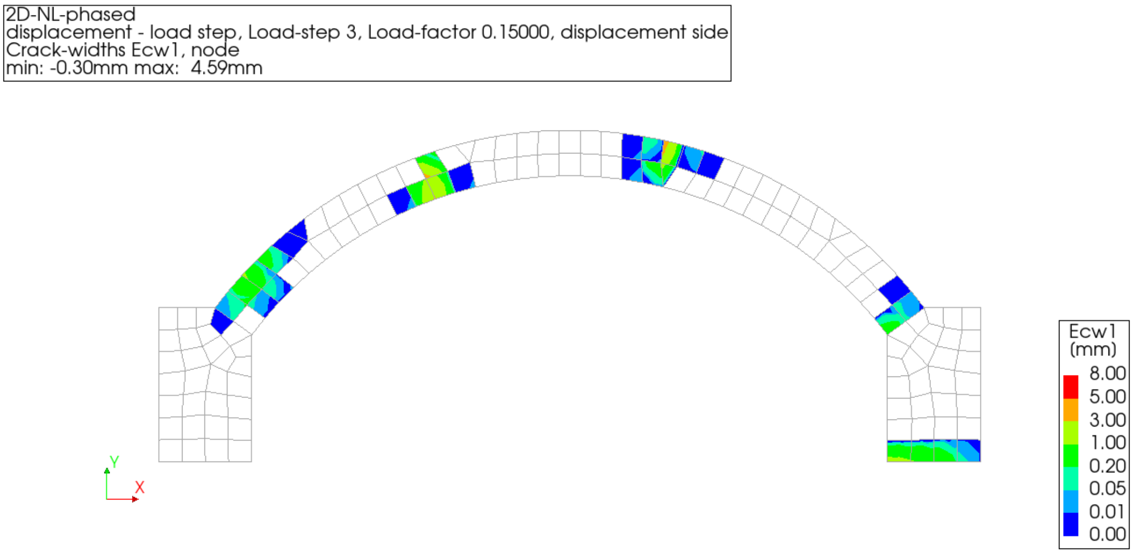

Figure 72. Cracking pattern for the 2D model at the peak load

The 3D representation of what is happening in the 2D model with the loading is illustrated in Figure 73. Where the bell shape observed as the load spread previously is not what a 2D model represents when working with an effective width. What is happening is that the 2D model is actually having a rectangular shape in the load spread. This is consistent with the cracking patterns seen in the 2D model.

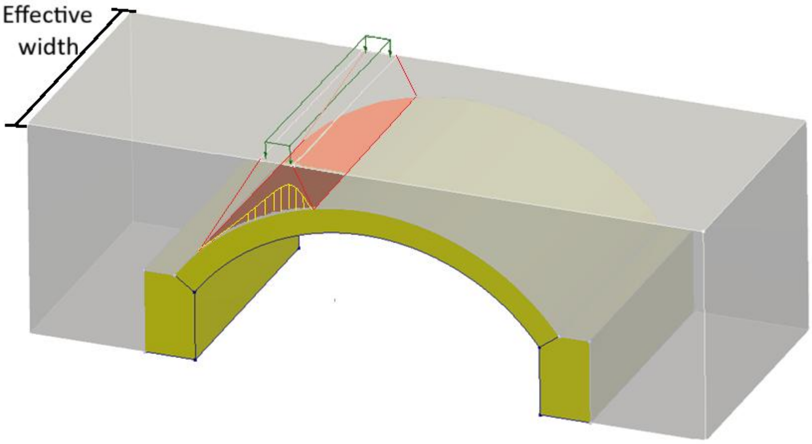

Figure 73. 2D model explained in a 3D vision

Chapter 5 Conclusions and recommendations

This chapter summarizes the main findings from the research and provides conclusions regarding the effectiveness of 3D continuum finite element modelling in assessing masonry arch bridges. The conclusions highlight the differences between 2D and 3D approaches, the role of spandrel walls, and the relevance of realistic soil structure interaction in achieving accurate assessments. Additionally, recommendations are proposed for future work, including potential model refinements, applications to other bridge geometries, and guidelines for implementing advanced numerical analyses in practical engineering assessments and conservation projects.

5.1 Conclusions

The main objective of this research is to evaluate whether the use of a 3D model (including spandrel walls) can provide greater accuracy than a 2D model while understanding load spread, and the effect of spandrel walls. This was divided into sub questions that contribute to answering the main research question, as follows.

How to select material properties that should be used to make the model comparable to the benchmark?

Initially, the material properties are ideally determined through laboratory tests. These should be done with sufficient number of tests to determine the values; and with low variation between the tests for the properties to be representative. Results show that even with data obtained from tests, some calibration is necessary to match the structural response of a real case scenario when modelling a masonry arch bridge. Properties determined from laboratory test at a material level are not 100% accurate when used in structural FEM. Specially the Young's modulus of masonry since this value is typically overestimated with the laboratory tests, in this case the reduction was of 27%. The properties that can't be determined by tests should be taken from typical values or correlations for the same type of material. It is recommended that the most influential properties are calibrated using a similar real case scenario test, but this can only be done if there is a benchmark to compare with. As for the properties that cannot be calibrated and are taken from typical values, they can still be representative enough to be able to model a structure, as shown in this research.

How does the choice of effective width in a 2D plane strain model influence its performance relative to a 3D model without spandrel walls?

In the linear elastic model, the load distribution through the backfill is used to calculate the effective width of the arch. Within this framework, an angle of approximately 50° provides a good approximation of the effective width when considering the combined depth of the soil and the masonry beneath the applied load. In 3D models, the load spreads following a bell shaped distribution, producing a circular footprint on the masonry surface. In contrast, 2D plane strain models generate a rectangular load projection due to their geometric simplifications. In nonlinear analyses, however, the load distribution evolves throughout the simulation as progressive damage and inelastic deformations develop in both masonry and soil. Consequently, the 50° load-spread angle defined for the linear elastic phase no longer represents the real behavior at failure.

Because of this previous point, although the 2D model has a response curve similar in shape to that of the 3D model without walls, its peak load is governed by the effective width derived from the linear elastic approximation and therefore underestimates the actual capacity. The effective width calculated in the linear analysis is insufficient once nonlinear effects are considered. While the 2D and 3D responses are qualitatively comparable, using the linear effective width results in an underestimation of the peak load capacity by approximately 29%. Regarding the failure mechanism, the cracking sequence and hinge locations are very similar in both models, indicating that these aspects are not significantly affected by the effective width assumption. However, additional adjustments are required to match the nonlinear response, which effectively involves accounting for the full transverse participation of the bridge, as the entire width becomes engaged in resisting loads at failure.

What are the differences in stiffness, peak load capacity, cracking patterns and ductility between the 3D model and the benchmark experiment?

The 3D model with spandrel walls is very close in the linear-elastic analysis to the benchmark since the materials were calibrated to match the stiffness. As for the nonlinear analysis, the stiffness decreases slightly due to the additional properties introduced with the constitutive models that were applied. The peak load capacity of model C is close to the benchmark, reaching 87% of the benchmark's capacity when including the interfaces properties, and model B is reaching 95,5% of the peak capacity. Which indicates that the addition of interfaces in the model play a minor role. The cracking patterns match the locations, and the 4-hinge failure is also reached by the continuum model. The ductility resulted in a lower one for the model compared to the benchmark but still presented a radial displacement due to a sustained load.

What are effects on stiffness, peak load capacity, cracking patterns and ductility due to the spandrel walls?

The spandrel walls contribute positively to the capacity of the bridge. When considering spandrel walls, the stiffness is 30-36% higher and the peak load is about 50% higher. The cracking patterns differ in a way that the model including the spandrel walls redistributes the cracking, differently from the model without the walls. Although to analyze the failure type and hinge formation the model excluding the walls is easier to understand. Ductility can't be fully assessed, as none of the models show a significant drop of capacity before the end of the analysis, same as for the test.

With the sub questions answered, the main question of this research can be addressed:

How much can performing a continuum 3D finite element analysis improve the accuracy in the assessment of masonry arch bridges compared to 2D models?

As determined in the research, the 2D model, as modeled in this research, is not as representative as the 3D model to be used for an assessment. The 2D model requires further calibration but can be used to determine the failure mechanism. The 3D continuum model demonstrated that, with the correct properties, it can closely predict stiffnesses, peak load capacity, and the cracking pattern and sequence and ductility. Although the curve behavior is slightly complex, the overall behavior is the same. A 13% error in the 3D model with walls, compared to a 55% error in the 2D model indicates that the 3D continuum model is more reliable. Whereas the 2D continuum model can still be representative for the pre-peak considering that the effects of the spandrel walls are not considered in this model, even then underestimating slightly the real response of the benchmark. As the spandrel walls have a positive effect in the overall response of the bridge, when modeling them in a 3D model, it will improve the accuracy of the model by 42%. It can therefore be concluded that the 3D continuum model is more accurate for an assessment of masonry arch bridges than 2D models.

5.2 Recommendations

The analysis with the cracking patterns and displacements in the spandrel walls can be investigated further. This can be done by using different constitutive models that can better simulate the nonlinear behavior of the spandrel walls because there are models that were made specifically for walls (which is a topic that has been widely explored). Since the spandrel walls play an important role in providing lateral confinement and redistributing loads, understanding their cracking mechanisms would help clarify how they influence the overall stiffness and the capacity of the bridge.

A sensitivity analysis on the mesh size could also be studied to identify the influence on the accuracy of the model results. This would determine whether or not the structural response is dependent on the mesh size, increasing or decreasing the reliability of the model. By doing so, the most efficient mesh configuration can be determined.

The results of future experimental tests can be improved by measuring the displacement at the load application point in the at the top of the backfill. This would allow for a more comprehensive comparison between experimental and numerical results, enhancing the accuracy of model calibration and the understanding of load transfer mechanisms within the structure.

The research can be extended by including cyclical loading, which can lead to material degradation. Since the benchmark test already considered cyclic loading and demonstrated changes in stiffness within the linear elastic range, it is possible that the peak load capacity is influenced by this behavior. Including cyclic or dynamic loading would provide valuable information on how repeated traffic loads affect the long-term performance and degradation of masonry bridges, making the model closer to real-life conditions.

Further studies to better characterize the materials would help confirm whether the input parameters used in the model are correctly defined and calibrated. Laboratory or field testing with low variability in the measured properties would increase the reliability and reproducibility of the results. This would support the development of more accurate constitutive models for masonry and soil, reducing uncertainty in future analyses.

Understanding the load spread effect in the nonlinear framework can be achieved by analyzing the changes in the load spread per load step. From this, a new load spread angle for nonlinear analysis could be determined so that the effective width becomes comparable. Alternatively, an improved method for determining the effective width could be developed, allowing the 2D model to effectively represent the 3D model without the spandrel walls.

The ductility of the model can be further explored through sensitivity studies. It is recommended to vary the fracture energy values, as well as to modify mode-II and mode-I parameters, to make the model more ductile or brittle depending on the scenario. This variation might affect the model’s outcomes. Since sliding cannot be fully represented when using a rotating crack model, performing simulations that compare fixed and rotating crack can provide a better understanding of ductility and post-peak behavior. Therefore, such analysis would improve the understanding of the model’s performance.

Finally, combining monitoring and modeling with masonry arch bridges which are still in use can improve the confidence of the predictions. This can be done using strain gauges, displacement sensors, digital image correlation, or even drones with LiDAR technology. Conducting simulations in a 3D continuum model with a moving load would allow comparison between the model’s behavior to the measurements, helping to verify and extend the conclusions made in this research while providing feedback on modeling practices.

Chapter 6 Bibliography

American Concrete Institute. (2019). *Building code requirements for structural concrete (ACI 318-19) and commentary (ACI 318R-19)*. American Concrete Institute.

Angelillo, M., Lourenco, P. & Milani, G. (2014). Masonry behaviour and modelling. Mechanics of masonry structures (pp. 1–26). Springer. https://doi.org/10.1007/978-3-7091-1774-3_1

Boussinesq, J. (1885). *Application des potentiels à l'étude de l'équilibre et du mouvement des solides élastiques.* Paris, France: Gauthier-Villars.

DIANA FEA. (2025). *DIANA Theory manual* (Version 10.10). DIANA FEA BV. Retrieved from https://manuals.dianafea.com/d1010/en/1306105-1306105-theory-1010.html

Duncan, J. M., & Wright, S. G. (2005). *Soil strength and slope stability*. John Wiley & Sons.

Domenico, P. A., & Schwartz, F. W. (1990). *Physical and chemical hydrogeology* (2nd ed.). John Wiley & Sons. Retrieved from https://health.hawaii.gov/heer/files/2021/07/Domenico1990.pdf

European Committee for Standardization. (2005). *EN 1996-1-1: Eurocode 6: Design of masonry structures. Part 1-1: General rules for buildings. Rules for reinforced and unreinforced masonry*. CEN.

Heyman, J. (1969). *The safety of masonry arches*. International Journal of Mechanical Sciences, 11(4), 363–385. https://doi.org/10.1016/0020-7403(69)90070-8

Heyman, J. (1982). *The masonry arch*. Ellis Horwood.

Ferreira, G. A. (2007). Modelação e Avaliação Estrutural de Pontes em Arco de Alvenaria. [Master thesis]. Universidade de Coimbra

Ghiassi, B., Vermelfoort, A. T., & Lourenço, P. B. (2019). Masonry mechanical properties. In B. Ghiassi & G. Milani (Eds.), *Numerical modeling of masonry and historical structures* (pp. 239–261). Woodhead Publishing. https://doi.org/10.1016/B978-0-08-102439-3.00007-5

Karlinasari, R., & Rachmadan, R. (2020). *Analysis of lateral deformation of mini pile around the vacuum consolidation area*. *IOP Conference Series: Earth and Environmental Science*, *584*(1), 012065.

Lantsoght, E. O. L., Yang, Y., & van der Veen, C. (2022). Multi-level decision-making strategy for preparation of proof load and failure tests. *Engineering Structures, 252,* 113672.

Lei, Q., Latham, J.-P., Xiang, J., & Lang, P. (2014). *Representation of large scale network geometry with realistic apertures determined by mesoscale geomechanical modelling of a natural fracture system*. In J. F. Labuz (Ed.), Proceedings of the 48th U.S. Rock Mechanics/Geomechanics Symposium (Vol. 2, pp. 1146–1155). American Rock Mechanics Association.

Liu, B.; Sarhosis, V.; Booth A.D.; & Gilbert, M. (2024). The 3D response of a large-scale masonry arch bridge – Part II: Performance at failure. *Engineering Structures, 313*(2024), 1-16. https://doi.org/10.1016/j.engstruct.2024.118308

Lourenco, P.B. & Rots, J.G. (1998). Possibilities of Modeling Masonry as a Composite Softening Material: Interface Modeling and Anisotropic Continuum Modeling. Proceedings of the 12th Engineering Mechanics Conference, ASCE, San Diego, U.S., p. 56-61

Lourenco, P.B. (1994). Analysis of masonry structure with interface elements (Report no. 03-21-22-0-01 / report no. 94-NM-R0762). TU Delft and TNO.

Milani, G. & Lourenço, P.B. (2012). 3D non-linear behavior of masonry arch bridges. *Computers and structures, 110-111(*2012),133-150. https://doi.org/10.1016/j.compstruc.2012.07.008

NEN. (2020). *NPR 9998:2020 Assessment of structural safety of buildings in case of erection, reconstruction and disapproval: Induced earthquakes — Basis of design, actions and resistances*. Netherlands Standardization Institute.

Paeglītis, A., Paeglītis, A., Vītiņa,I. & Igaune S. (2013). Study and Renovation of Historical Masonry Arch Bridge. *The Baltic Journal of Road and Bridge Engineering (Mar 2013), 8*(1), 32-39. https://doi.org/10.3846/bjrbe.2013.05

Papa, T.; Grillanda, N. & Milani, G. (2021). Three-dimensional adaptive limit analysis of masonry arch bridges interacting with the backfill. *Engineering Structures, 248*(2021), 1-19. https://doi.org/10.1016/j.engstruct.2021.113189

Pipinato, A.(2016). *Chapter 12 – Masonry bridges. Innovative Bridge Design Handbook*. Pages 299-33, Butterworth-Heinemann. https://doi.org/10.1016/B978-0-12-800058-8.00012-8

PLAXIS. (2018). *PLAXIS 2D 2018 reference manual*. Delft, The Netherlands: PLAXIS bv.

Rots, J., Hendriks, M. & Esposito R. (2024). Notes from CIEM5230-U3 Concrete structures [Power Point lecture notes]. Retrieved from Brightspace: https://brightspace.tudelft.nl/d2l/le/content/680488/Home

Sarhosis, V, De Santis, S., and de Felice, G. (2016). *A review of experimental investigations and assessment methods for masonry arch bridges*. Structure and Infrastructure engineering, 12, (*11*), 1439–1464. http://dx.doi.org/10.1080/15732479.2015.1136655

Sarhosis, V. ; Liu, B. & Gilbert, M. (2024). The 3D response of a large-scale masonry arch bridge - part I: Performance under low and medium loading levels. *Engineering Structures, 316*(2024), 1-18. https://doi.org/10.1016/j.engstruct.2024.118496

Stacho, J., Sulovska, M., & Slávik, I. (2023). *Analysis of the shear strength of a soil-geosynthetic interface*. *Civil and Environmental Engineering, 19*(1), 452-463.

StoneArchBridges. (2021). Understanding Mortar in Old bridges. Stone Arch Bridges. Retrieved from https://stonearchbridges.com/2021/12/17/understanding-mortar-in-old-bridges/

Tang, N., Lei, D., Huang, D., & Xiao, R. (2019). Mechanical performance of polystyrene foam (EPS): Experimental and numerical analysis. *Polymer Testing, 73*, 359–365. https://doi.org/10.1016/j.polymertesting.2018.12.001

Van Breda, S.M.S. (2023). *The role of constitutive models on simulating the structural behaviour of masonry arch bridges.* [Master of Science Thesis not published]. TUDelft.

Van Dalen, K. & Vardon, P. (2023). Notes from CIEM 0000-U2 Interdicipinary Mechanics and design for CE [Power Point lecture notes]. Retrieved from Brightspace: https://brightspace.tudelft.nl/d2l/le/content/680398/Home

Chapter 7 Appendix

Table A 1. Description of the tests of the benchmark

Test No.	Plate locations	Type of load	Level	Loading area [mm]
T1	A	Static	Low-load (150kN)	300x300
T2	B	Static	Low-load (150kN)	300x300
T3	C	Static and cyclic	Low-load (150kN)	300x300
T4	D	Static and cyclic	Low-load (150kN)	300x300
T5	E	Static and cyclic	Low-load (150kN)	300x300
T6	F	Static and cyclic	Low-load (150kN)	300x300
T7	A	Static and cyclic	Low-load (150kN)	300x300
T8	B	Static and cyclic	Low-load (150kN)	300x300
T9	G	Static and cyclic	Low-load (150kN)	300x300
T10	H	Static and cyclic	Low-load (150kN)	300x300
T11	I	Static and cyclic	Low-load (150kN)	300x300
T12	G	Static and cyclic	Mid-load (250 kN)	300x300
T13	A	Static and cyclic	Mid-load (250 kN)	300x300
T14	D	Static and cyclic	Mid-load (250 kN)	300x300
T15	F	Static and cyclic	Mid-load (250 kN)	300x300
T16	J	Static and cyclic	Mid-load (250 kN)	300x300
T17	C	Static and cyclic	Mid-load (250 kN)	300x300
T18	E	Static and cyclic	Mid-load (250 kN)	300x300
T19	H	Static and cyclic	Mid-load (250 kN)	300x300
T20	B	Static and cyclic	Mid-load (250 kN)	300x300
T21	B	Static	High-level (560 kN)	750x300
T22	B	Static	Failure-load	750x300
T25	H	Static	Failure-load	750x300

Table A 2. Stiffnesses of the bridge due to differences in the material Young's modulus while keeping the other material properties in the linear elastic range

Material	Young's modulus change for material [MPa]	Bridge stiffness due to side load [kN/mm]	Bridge stiffness due to center load [kN/mm]
Masonry	9000	734,5	416,3
	8000	663,5	374,1
	7500	627,9	352,9
	7000	592,3	331,7
	6800	578,0	323,2
	6500	556,6	310,5
Backfill	50	788,6	454,4
	30	762,1	444,9
Reinforced concrete wall	35000	816,8	465,5
	15000	809,1	460,2

7.1 Shear retention comparison

Additional models were made for a shear retention comparison where the new models maintain the same geometry, and configuration per model except for the shear retention value of zero for the masonry (for models B’, C’, E’ and F’). As for the rest of the material properties, all are maintained. In the case of fixed cracking model, which is the constitutive model used for this research, the crack can reorient after the first cracks and cause misalignments that produce shear. Models A and D are not affected by the change due to the masonry having a linear-elastic constitutive model, therefore these are not shown in the comparison. The additional results are shown in Figure A 1.

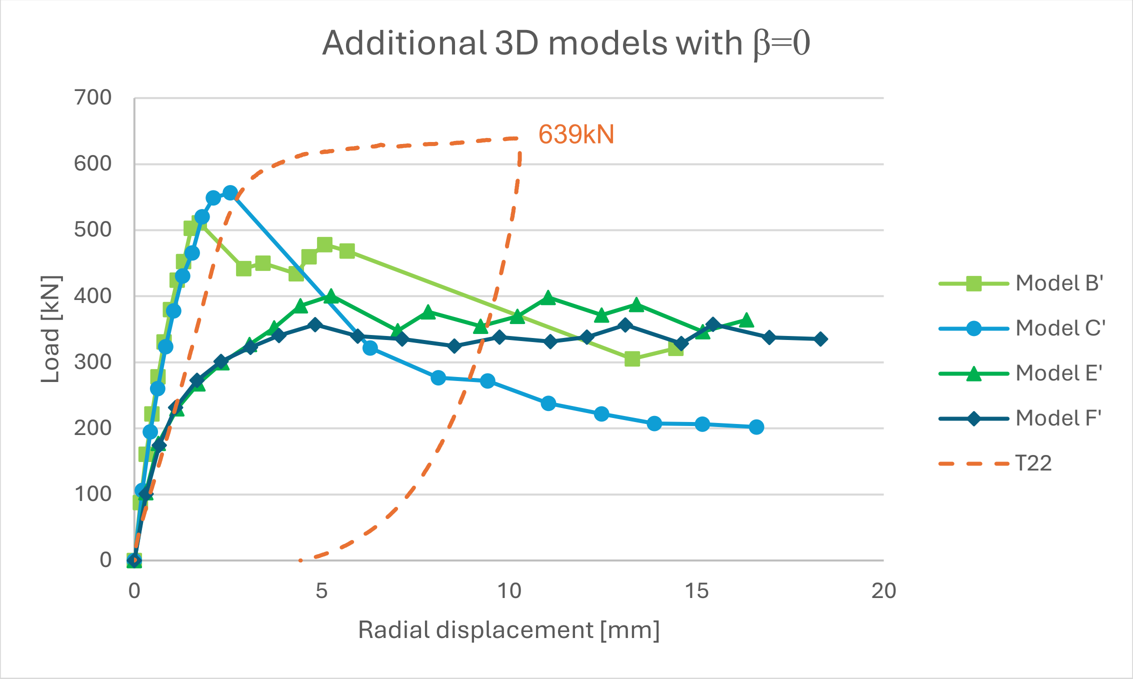

Figure A 1. Load-displacement curve for the zero-shear retention value

These load-displacement curves show a similar behavior to the shear retention value of 0,01 for the models E’ and F’ which means that this parameter value doesn’t have a significant effect. Whereas the models B’ and C’, the models with spandrel walls, seem to have more significant effect. This is reasonable since the cracking in the walls is most likely to have misalignments due to diagonal cracking.

The main difference is the post-peak behavior and the ductility. The displacement at which the capacity drops around 20% of the peak load for models C’ and B’, the radial displacements are 4,5 mm and 8,5 mm respectively. Therefore, the model C’ evidently has less ductility than model B’, since the displacements are larger when having the same percentage drop.

With these results, model F’ has a small reduction in the capacity, still not too significant. Although, reducing the shear retention increases the overall capacity of model F’ doesn’t have significant difference. Whereas model C’ does maintain the same peak load as the model C, resulting in a same error between the benchmark, and the post peak behaviour has a sudden fall in capacity, which is the same behavior as for model B’. This means that the shear retention parameter has a significant effect on the post-peak behavior, and that not introducing this correctly may lead to unreliable post-peak results.

A smaller load step does provide a better resolution in the load-radial displacement curve and gives a better understanding of the behavior of the model with the shear resistance value, which is not made with these models. As the results show, model F’ tends to have slightly lower load capacities due to the introduction of the interfaces while models B’ and E’ and they all are not consistent. But having a smaller load step or higher resolution around the peak load would most likely have a higher peak load for model B’ and would explain the lower peak-load without interfaces, in the present case.

While analyzing the post peak models B’ and C’ have a worse ductility compared to the models with 0,01 shear retention. Both models show a significant lower ductility having more of a brittle behavior different from the same value as the benchmark and models b and C. Which means that the shear retention plays a significant role in the post peak behavior of the models with spandrel walls and provides more reliable results, especially in the post-peak behavior.

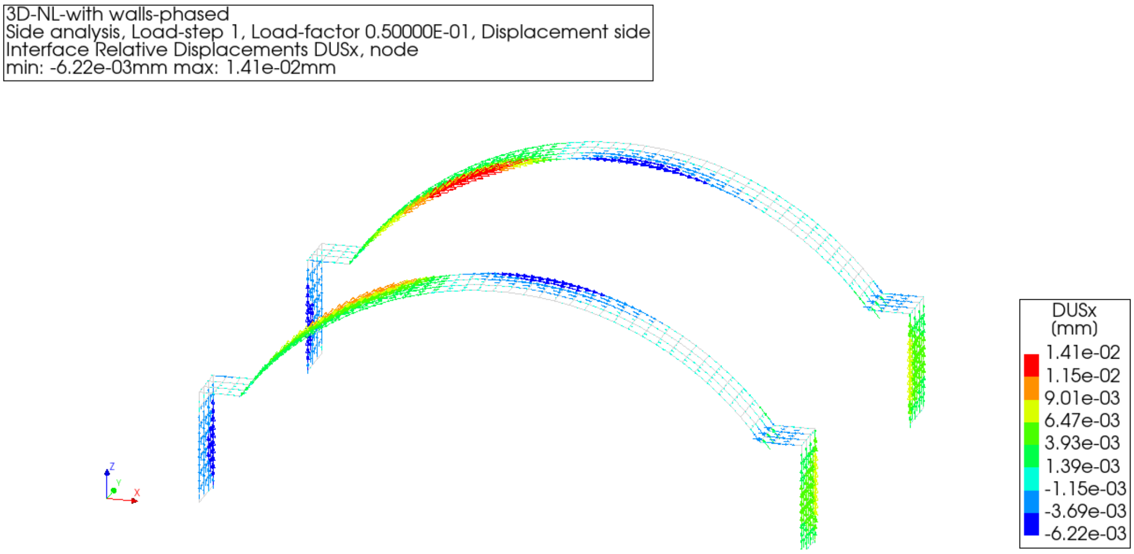

Figure A 2. Interface relative displacements along the arch in model C’ for 106kN

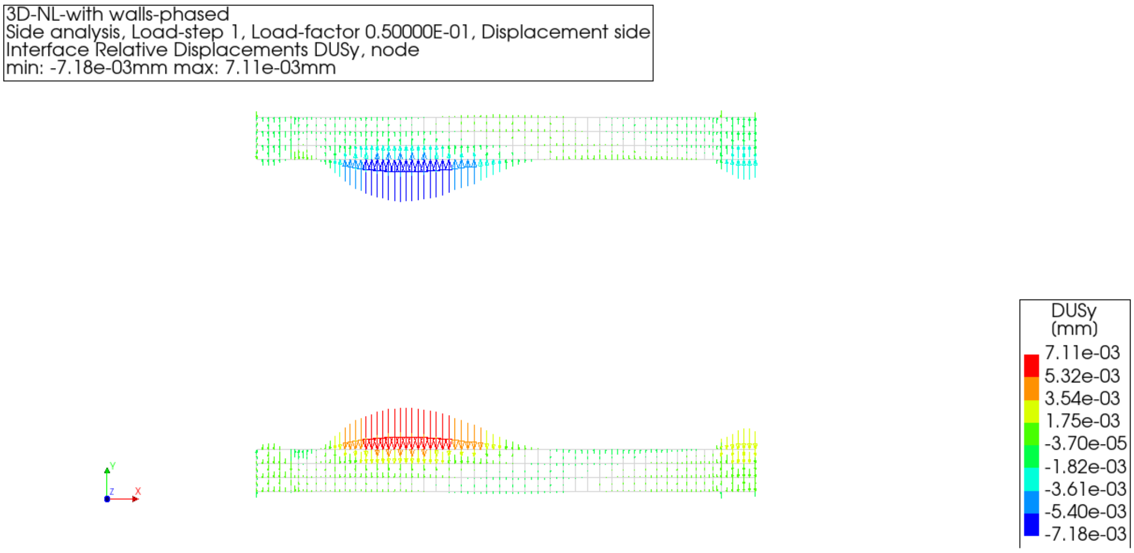

Figure A 3. Interface relative displacements perpendicular to the arch in model C’ for 106kN

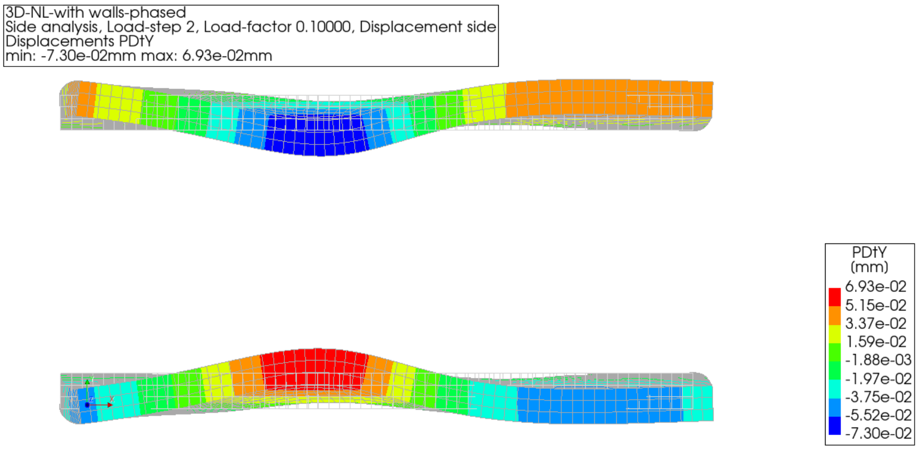

Figure A 4. Out-of-plane deformation of the spandrel walls top view for model C’ at 195 kN

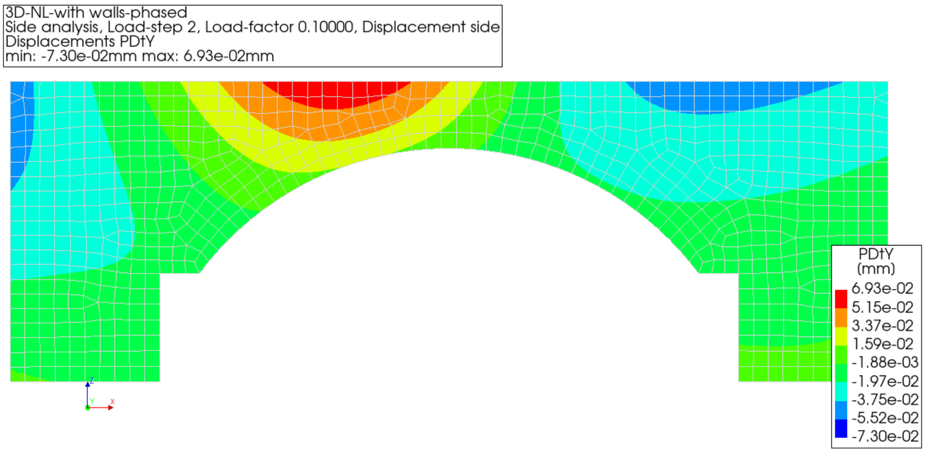

Figure A 5. Out-of-plane deformation of the spandrel walls side view for model C' at 195 kN

As seen in Figure A 2, Figure A 3, Figure A 4 and Figure A 5, the interface relative displacements are maintained as the results in section 4.3 and the displacements in the spandrel walls remain the same for the same load, therefore the higher shear resistance does not affect the outcome of the response of the interfaces and the spandrel walls. But a smaller load step does provide a better resolution in the load-radial displacement whereas not having this better resolution limits the identification of the peak load, which can be why the model B' has a lower peak load than model C'.

7.2 Convergence plots

The convergence plots for both the models with shear resistance zero and shear resistance 0,01.

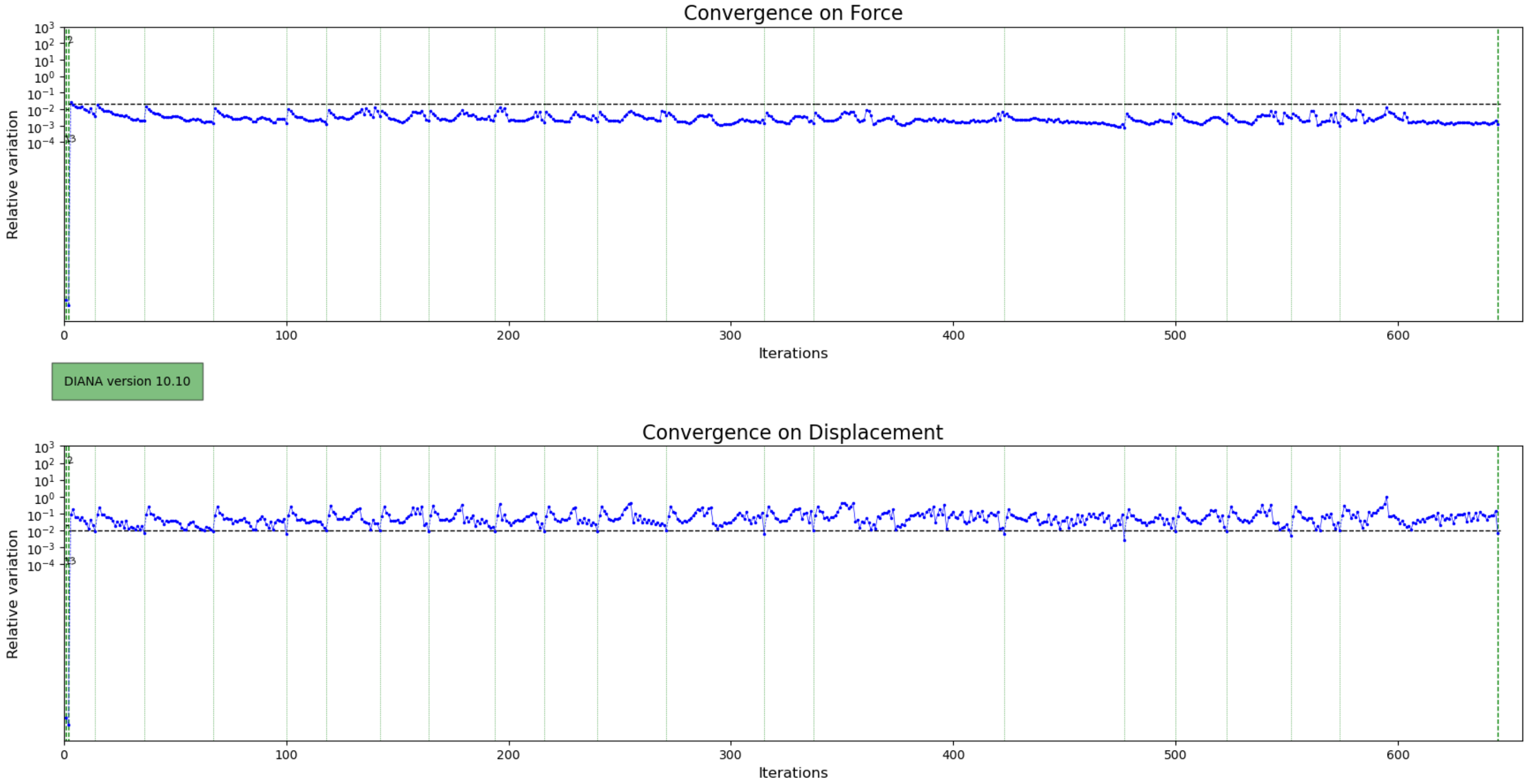

Figure A 6. Convergence plots for model A

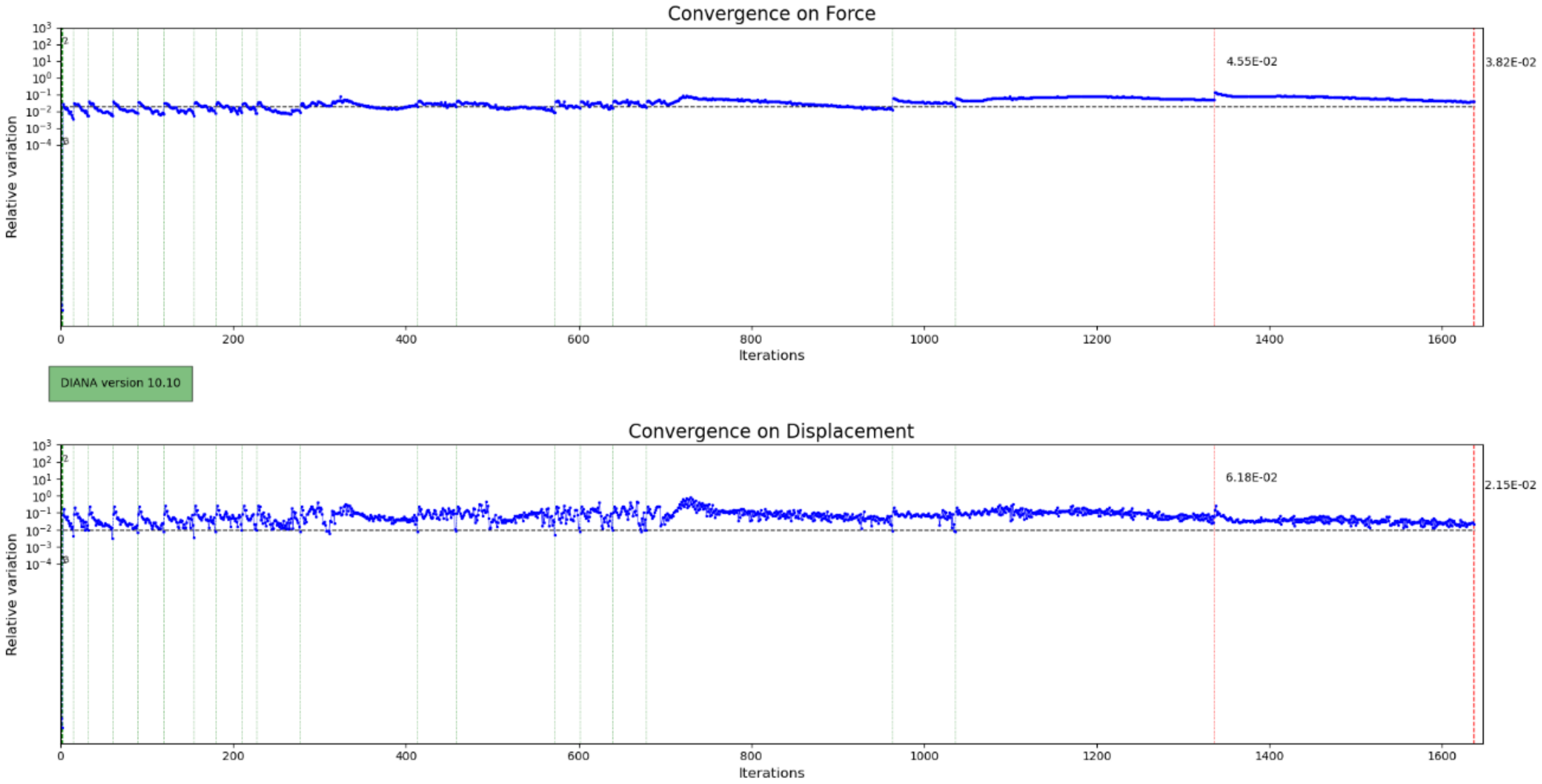

Figure A 7. Convergence plots for model B’ (β=0)

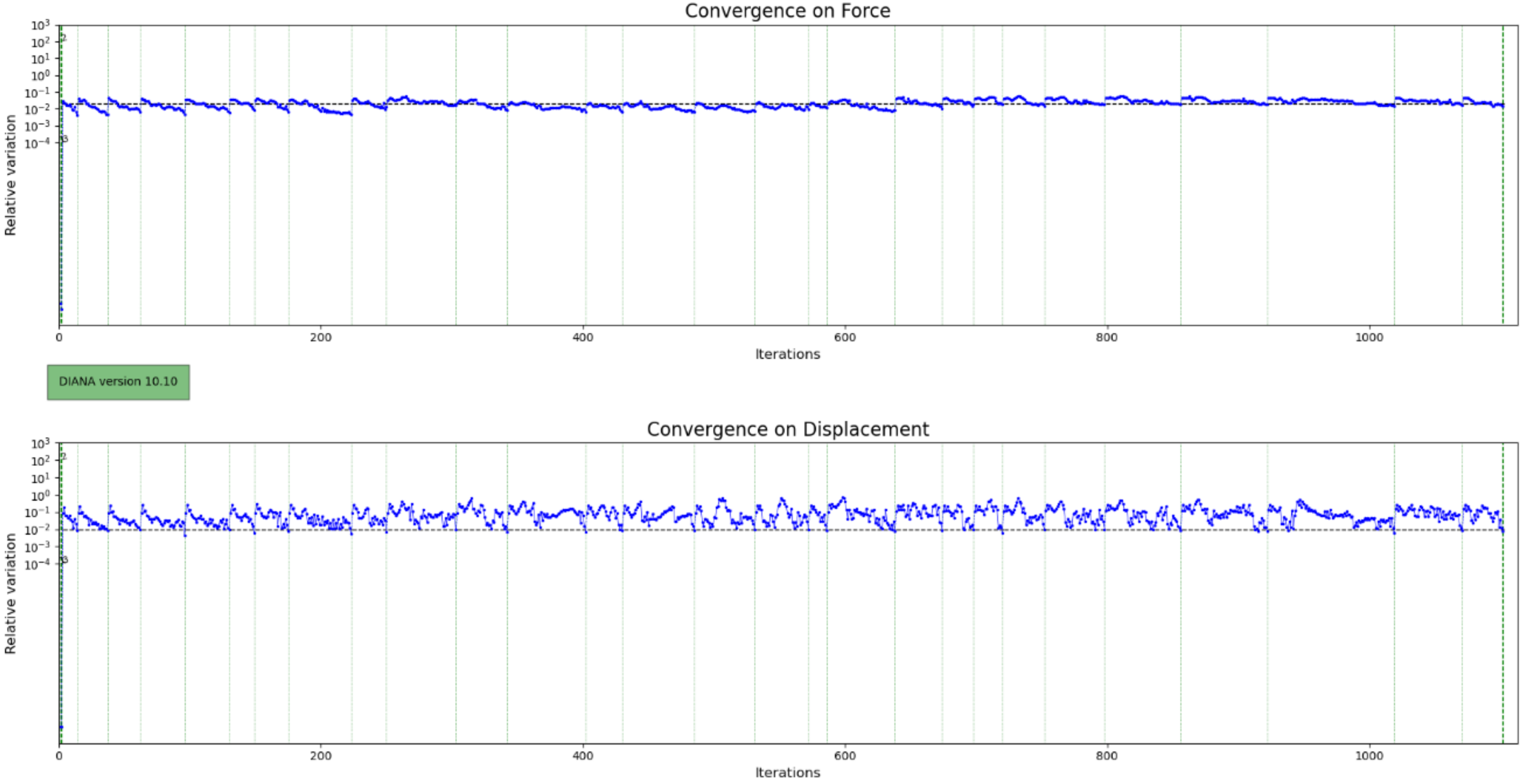

Figure A 8. Convergence plots for model B (β=0,01)

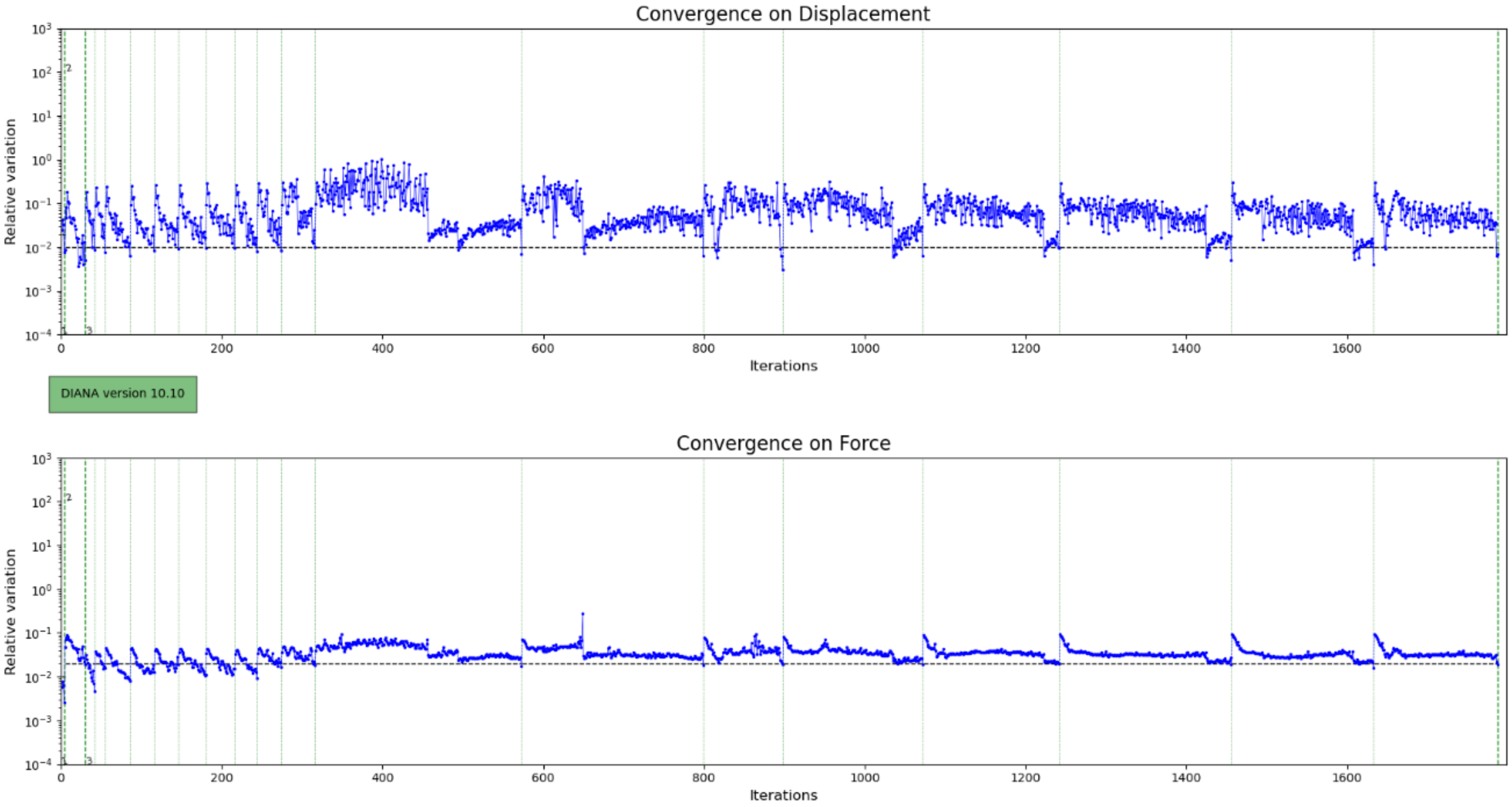

Figure A 9. Convergence plots for model C’ (β=0)

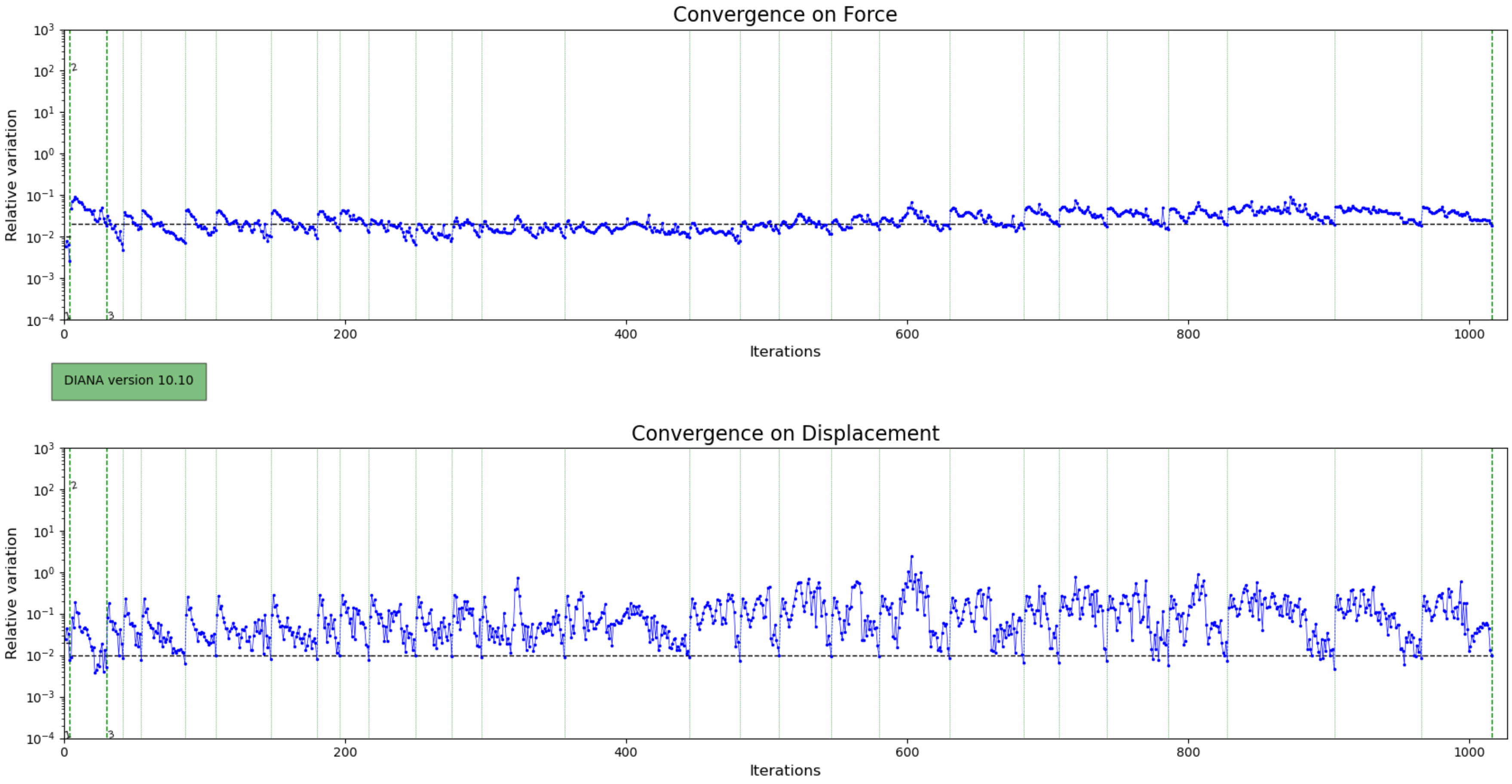

Figure A 10. Convergence plots for model C (β=0,01)

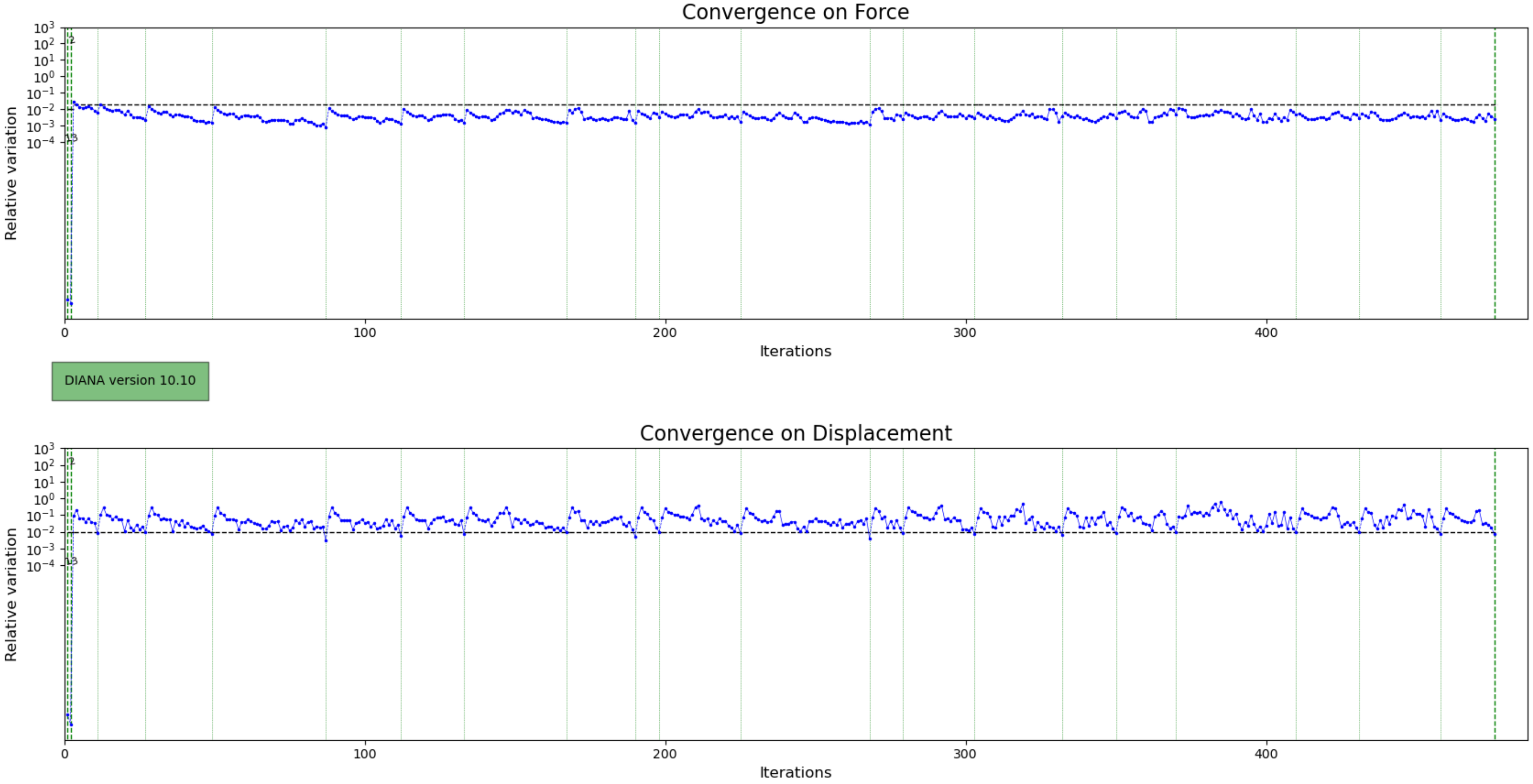

Figure A 11. Convergence plots for model D

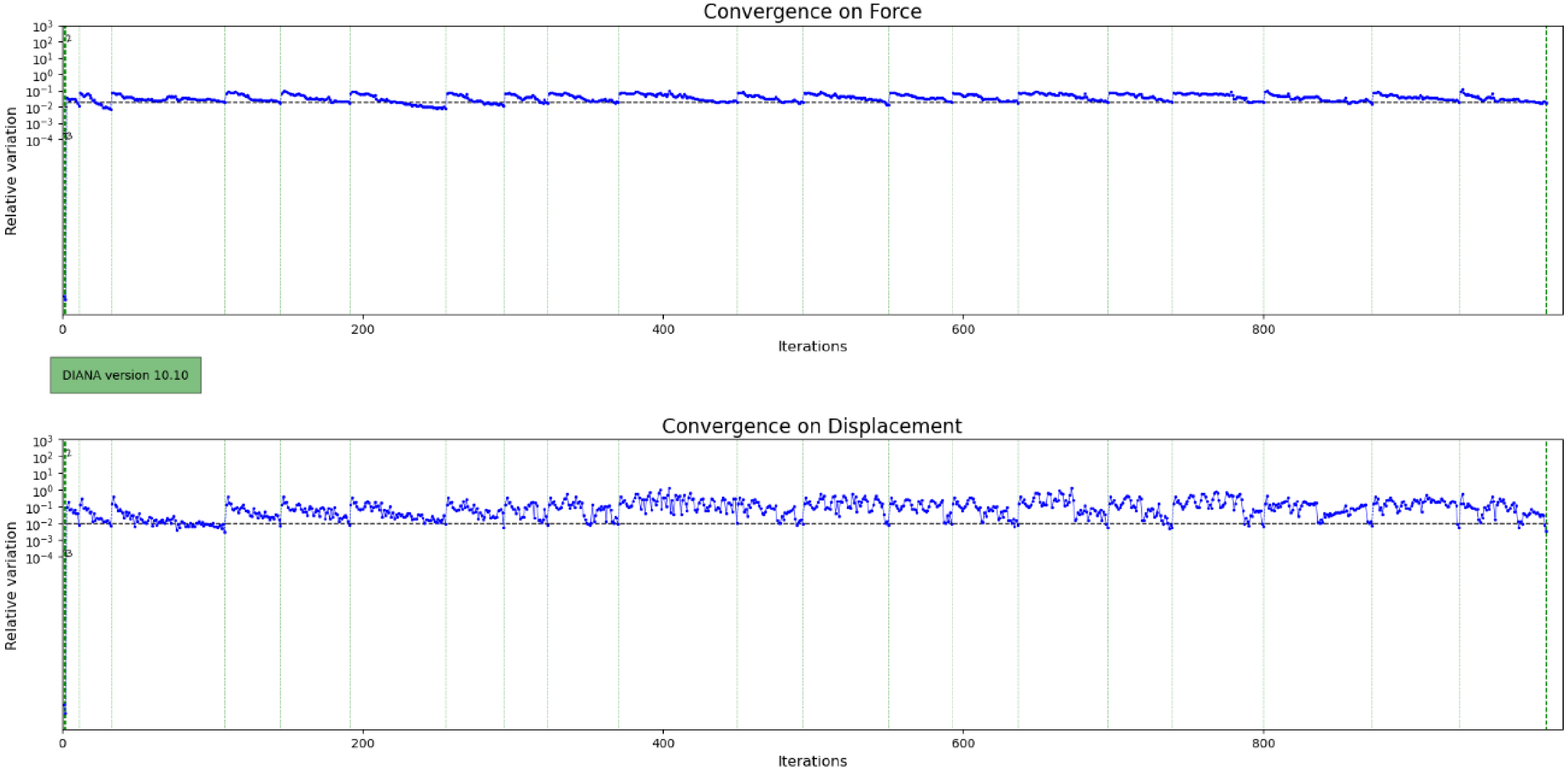

Figure A 12. Convergence plots for model E’ (β=0)

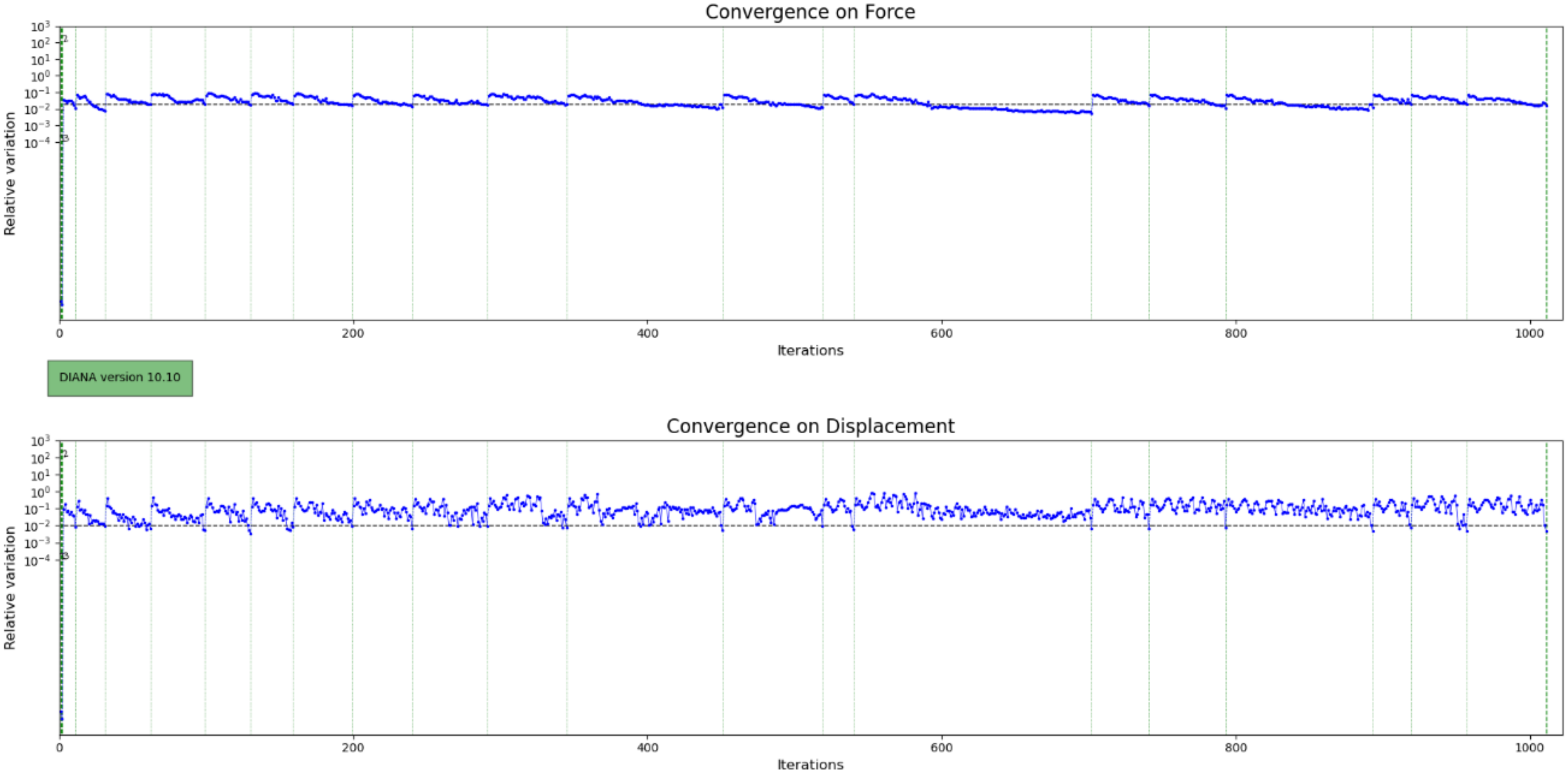

Figure A 13. Convergence plots for model E (β=0,01)

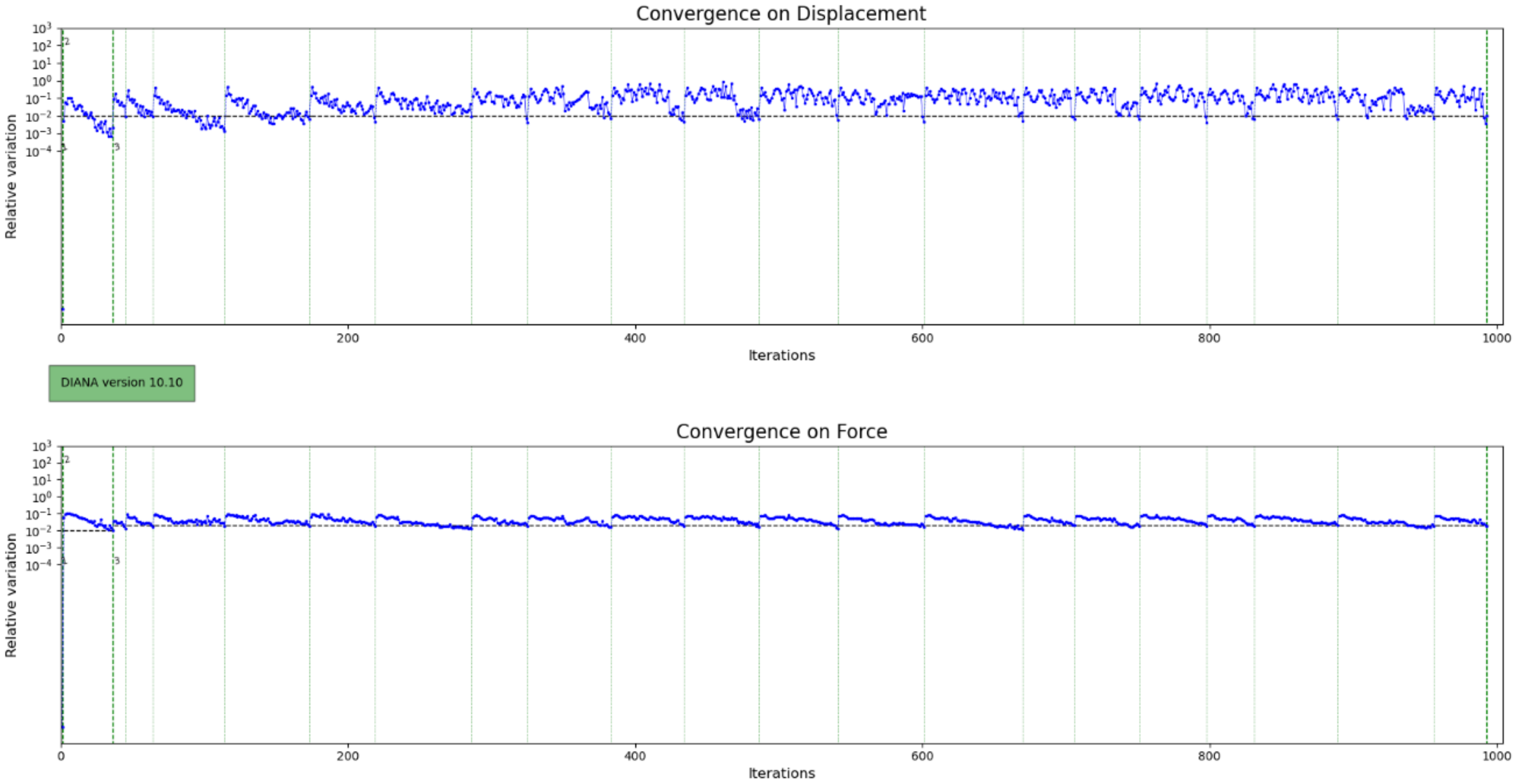

Figure A 14. Convergence plots for model F’ (β=0)

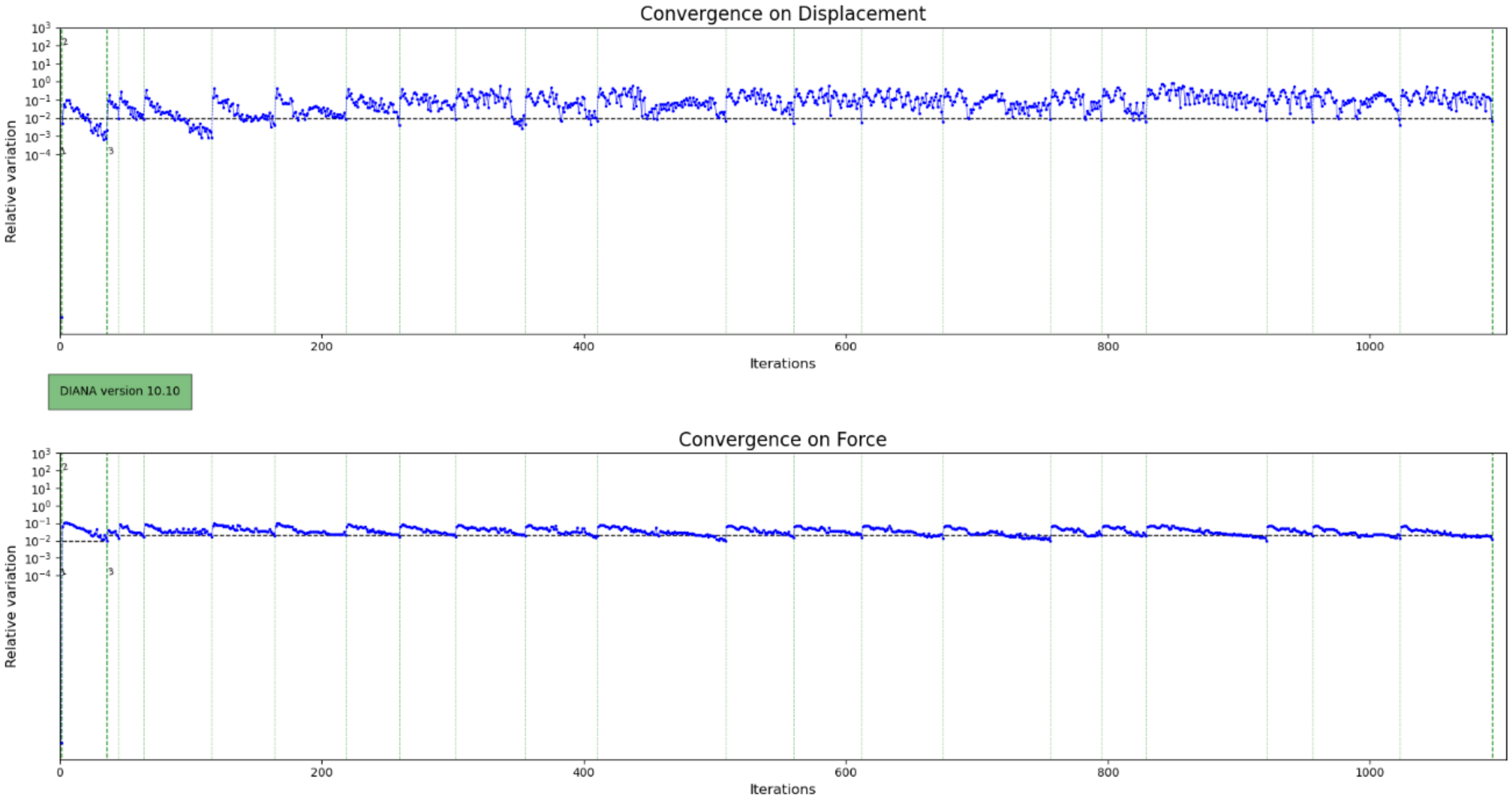

Figure A 15. Convergence plots for model F (β=0,01)